ESA TPM CASSIOPE E-POP MISSION FINAL OPERATIONS REPORT

SWE-PO-FINAL OPERATIONS REPORT-0001-A

Prepared by	Andrew Howarth - UCalgary

Date of Issue	2024-06-13
Revision	A
Status	Release
Document Type	Final Report
Distribution	ESA

APPROVAL

Title: ESA TPM Cassiope e-POP Mission Final Operations Report	
Status: Release	Revision A
Prepared by Andrew Howarth	Date 2024-06-13
Approved by J. Antonio de la Fuente	Date 2024-06-14

CHANGE LOG

Reason for change	Revision	Date

CHANGE RECORD

	Revision B		
Reason for change	Date	Pages	Paragraph(s)

Table of Contents

1 INTRODUCTION

This is the Final Operations Report for the CASSIOPE e-POP Mission under the European Space Agency's (ESA) Third Party Mission (TPM) program. CASSIOPE was launched in 2013 by MacDonald, Dettwiler and Associates (MDA) in partnership with the Canadian Space Agency and the Canadian Industrial Technologies Office, joining the ESA Third Party Mission Program as Swarm Echo in February of 2018. Routine science operations for the mission ended on December 31, 2021. As of January 2024, the spacecraft is still operational, in a reduced capacity due to the loss of full attitude control and is no longer being operating under the ESA TPM program.

2 MISSION SUMMARY

CASSIOPE is a multi-purpose mission that brings together small satellite bus development, space science, and commercial technology demonstration into a single platform. CASSIOPE was launched by SpaceX on a Falcon 9 rocket from Vandenberg Space Force Base on September 29, 2013, into an elliptical polar orbit at an inclination of 81°, spanning altitudes from 320 km to 1500 km. CASCADE, the technology demonstration payload from MDA, is a high-speed data transmission payload that connects over a Ka-band link at 300 Mbps on two channels. e-POP, the science payload, is a space weather instrumentation suite consisting of eight scientific instruments for the investigation of phenomena related to the near-earth space environment. These two payloads are carried by a 500 kg, 3-axis stabilized small satellite platform that is part of the Canadian Small Satellite Bus program.

2.1 CASSIOPE BUS

Designed and built by Magellan Aerospace Winnipeg and pictured in Figure 1, CASSIOPE has a hexagonal structure that measures 180 cm across by 125 cm tall. The spacecraft was designed with a 2-year

lifetime at 95% reliability and has full redundancy in mission critical systems, including graceful degradation in mass memory, battery, and solar array.

Figure 1: CASSIOPE bus prior to launch

2.1.1 Power Subsystem

The CASSIOPE power subsystem is comprised of an array of five solar panels, a 24 A·h lithium-ion battery, and redundant power control units that serve as the interface between power source, storage, and load. During e-POP science orbits, power consumption averages near 180 W, with a peak draw of close to 400 W. The bus power system has the ability to operate between 22 and 34 output DC volts.

2.1.2 Attitude Control Subsystem

Attitude control on CASSIOPE consists of control algorithms working with uploaded parameter tables, reference tables, and data sampled from two bus magnetometers, six coarse sun sensors, four reaction wheels, three magnetic torque rods, and two star sensors.

CASSIOPE's star cameras are the micro Advanced Stellar Compass, provided by the Technical University of Denmark. When both star sensors are providing quaternion solutions, the merged solution has a precision near 30" (0.008°). With only one star sensor providing a solution, the precision drops to 200". Failing over to the coarse sun sensors for attitude knowledge drops the precision to 8° on average and can be incorrect by up to 30° at times. It is therefore of critical importance to consider the attitude solution source when working with science data that is dependent on the accuracy of the attitude solution. Details of how the star sensor attitude data were combined and how the resulting precision was calculated can be found in ESA document ESA-EOPSM-SWRM-TN-3487, based on the work of Dr. Christian Siemes.

2.1.3 Communications

Data uplink and downlink between CASSIOPE and a given earth station is accomplished via a radio frequency (RF) link in the S-band frequency range. Table 1 provides the parameters associated with the RF link.

Item	Value
Uplink Frequency	2054.84 kHz
Uplink Bandwidth	50 kHz
Uplink Polarization	Right-hand circular polarized
Uplink Bitrate	4 kbps
Downlink Frequency	2231.5 MHz
Downlink Bandwidth	5 MHz
Downlink Polarization	Right-hand circular polarized
Downlink Bitrate	Selectable: 4, 2, 1, 0.5 Mbps, 40 kbps

Table 1: CASSIOPE/Swarm-E S-band communication parameters

S-band patch antennas for transmitting and receiving are located on both the top (-Z) and bottom (+Z) panels of the spacecraft, with only a small 5° null near the center plane of spacecraft body, allowing for transmission and reception of signals in most attitude configurations.

2.1.4 e-POP

The e-POP payload consists of a complement of eight in-situ, imaging, and radio instruments designed to facilitate high-resolution measurements of the polar ionosphere. Figure 2 shows the layout of the e-POP instruments on the spacecraft along with the body axis definitions.

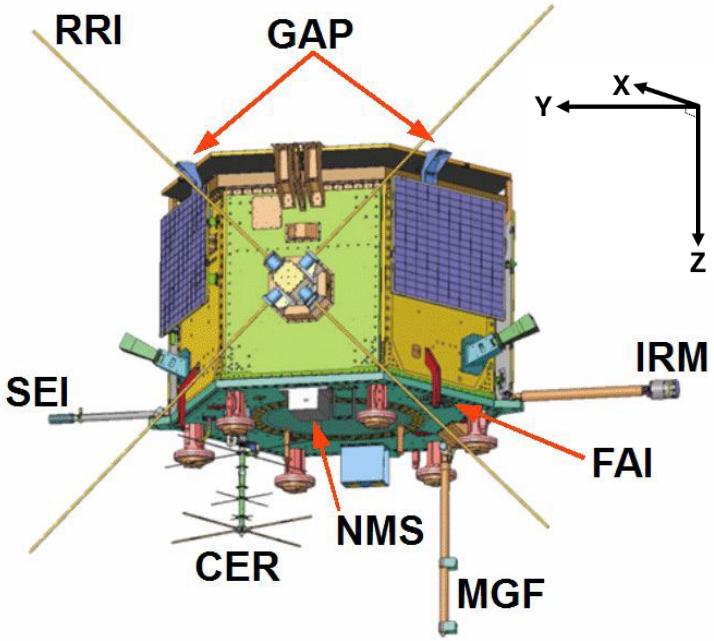

Figure 2: e-POP instruments on CASSIOPE/Swarm-Echo

2.1.4.1 CER

The e-POP Coherent Electromagnetic Radiation tomography experiment (CER) is a radio beacon transmitter designed to facilitate radio propagation and ionospheric scintillation measurements.

CER consists of a tri-frequency beacon and a three-frequency, circular polarized antenna on a 68.6 cm boom. CER generates beacon signals at 150, 400, and 1067 MHz for reception by receiver network chains around the world. Data is collected from these receiving stations and analyzed using ionospheric tomography techniques, producing 2-D ionospheric electron density maps.

The development of CER was spearheaded by the Naval Research Lab in Washington, D.C. under the direction of Dr. Paul Bernhardt.

2.1.4.2 FAI

The e-POP Fast Auroral Imager (FAI) is a dual CCD, single controller instrument for imaging the aurora. The two CCD cameras are differentiated by the permitted wavelength passbands, which are 630 nm for the visible camera, and 650-1000 nm for the near-infrared camera. Each camera head is equipped with f/4 optics, reduced to f/0.8 via a fibre-optic taper for high optical sensitivity, and a focal length of 68.9 mm.

The FAI imagers have a field of view of 26° and point in the +Z direction on the spacecraft, which is nominally pointed towards nadir (downward). Altitude profiles of the aurora can also be obtained by taking images of the night-side horizon, which makes use of the 3-axis stabilized platform of CASSIOPE/Swarm-E. Each CCD has 256 x 256 imaging pixels, giving the cameras a fundamental resolution of 0.1°, or 2.6 km at apogee for aurora at 110 km altitude. For greater sensitivity, the CCDs can perform on-chip binning resulting in 128 x 128 or 64 x 64 pixel images. The image quality of the backside-illuminated, low noise CCDs is further enhanced by the presence of thermal-electric coolers that reduce the temperature of the CCDs by up to 28°C below the ambient baseplate temperature, which is usually around -5°C.

FAI was developed at the University of Calgary in partnership with Routes AstroEngineering (now COM DEV), Burley Scientific, Keo Consultants Inc, and JENOPTIK Optical Systems, Inc. The lead scientist for FAI is Andrew Howarth.

2.1.4.3 GAP

The e-POP Global Position System (GPS) receiver-based Attitude, Position, and profiling experiment (GAP) is used for spacecraft position and attitude determination and for ionospheric radio occultation profiling measurements.

GAP employs five differential Global Positioning System receivers and associated antenna complement to provide the e-POP payload with high-resolution spatial positioning information, flight-path velocity determination, and real-time, high-stability timing. Spacecraft attitude may also be determined by combining the data from receivers connected to three of the top-mounted antennas. In addition, one of the GAP antennas is mounted on the anti-ram side of the spacecraft and dedicated to ionospheric radio occultation measurements in which the relative phase delay of the measured L1 and L2 signals (at frequencies of 1.57542 GHz and 1.2276 GHz, respectively) from different satellites of the GPS constellation are used to determine the electron density profile of the ionosphere using tomographic techniques. The other four antennas are mounted on the anti-nadir face of the spacecraft, with bore-

sights normal to the spacecraft surface, and are used primarily for the timing, position, and velocity measurements.

GAP was developed under the leadership of Dr. Richard Langley of the University of New Brunswick, in partnership with Magellan Aerospace Winnipeg and the University of Calgary.

2.1.4.4 IRM

The e-POP Imaging and Rapid-scanning ion Mass spectrometer (IRM) measures the composition and velocity distributions of ions in the 0.1-100 eV/q and 1-40 amu/q range. From these measurements the bulk plasma parameters in the ionosphere such as relative ion density, drift velocity, and temperature can be determined, with the goal of exploring topics including ion outflow from the topside ionosphere, perpendicular ion heating and acceleration, storm-time molecular ion upflow, and others.

The IRM sensor is cylindrical and deployed on an 88-cm boom. Its entrance aperture has a 360° field of view (FOV) perpendicular to the deployment axis and close to 120° FOV along the deployment axis.

For ion detection the IRM sensor employs a hemispherical electrostatic analyzer, a time-of-flight gate, a micro-channel plate detector, and a position-sensitive anode.

IRM was developed, built, and tested at the University of Calgary under the direction of Drs. Peter Amerl and Andrew W. Yau.

2.1.4.5 MGF

The e-POP MaGnetic Field instrument (MGF) consists of dual, tri-axial fluxgate magnetometers mounted on a 92.9-cm carbon fibre boom for measurements of magnetic field perturbations to a precision of 0.0625 nanotesla, from which to infer the DC magnetic field as well as small-scale field-aligned currents. The MGF sensors are separated by 32 cm center-to-center along the boom.

The Earth's magnetic field is measured at a rate of 160 measurements per axis per second. This temporal resolution allows detection of current structures down to the 100-meter scale, and the sensitivity allows for measurement of current densities down to 10-7 A/m^2.

The development of MGF was undertaken by Dr. Donald Wallis, in partnership with Bennest Enterprises and Narod Geophysics. The lead scientist for MGF is Dr. David Miles.

2.1.4.6 NMS

The e-POP Neutral Mass and velocity Spectrometer (NMS) measures mass composition and velocity of neutral atmospheric species in the 1-40 amu mass and 0.1-2 km/s velocity range.

NMS measures neutral particle constituents using an open-source electron impact ionization chamber and a microchannel plate (MCP) imaging detection subassembly. It employs a planar entrance aperture with a plasma filter to repel low energy charged particles. The rammed neutrals enter the aperture and traverse through an electron source. The ionized population is then accelerated into the instrument by a potential difference between the entrance aperture and the detection subassembly. Ions arriving at the annular microchannel plate detector are sorted according to their arrival angle (azimuthal location) and energy (radial location). Thus, the instrument can resolve both the neutral particle composition and the flow velocity.

NMS development was spearheaded by the Japan Aerospace Exploration Agency with Dr. Hajime Hayakawa as principal investigator.

2.1.4.7 RRI

The e-POP Radio Receiver Instrument (RRI) measures wave electric fields in the 10 Hz – 18 MHz range, at magnitudes from 1 µV/m to 1 V/m.

RRI is a four-channel VLF/HF receiver. It consists of four 3-meter STEM dipole antennas, a digital radio receiver module, and an electronics unit. At VLF, the receiver measures the electric fields of spontaneous waves in the frequency range 10Hz-10kHz. The receiver measures the electric fields of LF-HF radio emissions and of man-made waves transmitted from ground radars (CADI, SuperDARN and HAARP). The input dynamic range of the receivers is about 100 dB, covering an input signal level from -100 to 0 dBV. The receiver bandwidth can be selected at either 5 or 30 kHz.

The analog output of each antenna is fed through a high-impedance pre-amplifier, then matched to a 16-bit analog-to-digital converter. The amplitude and relative phase of the incoming signals is measured using the orthogonal dipole antennas, allowing for both the magnitude and direction of arrival of the waves to be determined.

RRI was built by COM DEV International in Ottawa, Ontario, with contributions from the University of Calgary under the direction of Dr. Gordon James.

2.1.4.8 SEI

The e-POP Suprathermal Electron Imager (SEI) measures the electron energy and pitch angle distribution over the energy range of 1 to 200 eV, with particular emphasis on photoelectrons in the 1 to 50 eV range.

SEI is a 2-D electrostatic analyzer/imager consisting of a 2.5-cm diameter cylindrical sensor head. The sensor is mounted on an 80-cm boom to place it outside the spacecraft sheath. Its skin bias is adjustable in its thermal mode to counteract the spacecraft potential and to control the input particle flux.

Incident electrons traverse the electrostatic hemispherical analyzer and are dispersed according to their energy and azimuth across the MCP detector. The energy range detected is dependent upon the sensor skin bias and the internal analyzer bias voltage. SEI has field of view of ±15° in elevation and 360° in azimuth. Its entrance aperture plane is within 15° of the local magnetic field at high latitude.

SEI employs a 256 x 256-element CCD detector that is optically coupled to the electronics unit and de-coupled from the sensor bias voltages. It uses an MCP to amplify the incident electron azimuth/energy distribution and image it onto a phosphor screen that is fibre-optically coupled to the CCD sensor. It can operate at an imaging rate of up to 100 Hz.

SEI was developed, built, and tested at the University of Calgary under the direction of Dr. David Knudsen.

3 OPERATIONS

3.1 DATA ACQUISITION

All Telemetry, Tracking, and Command (TT&C) services for CASSIOPE/Swarm-E have been provided by the Swedish Space Corporation (SSC) at their stations in Kiruna, Sweden (latitude 67.9°, longitude 21.1°), Inuvik, Canada (latitude 68.4°, longitude -133.5°), and, contracted through the German Aerospace Center (DLR), at O'Higgins, Antarctica (latitude -63.3°, longitude -57.9°). Having ground stations at high latitude in both the northern and southern hemispheres allows for long ground-contact periods at all points in the orbit precession period, regardless of if the apogee is in the northern or southern hemisphere.

The Launch and Early Operations Phase (LEOP) of the mission took place on September 29th and 30th, 2013, consisting of seven passes at the O'Higgins station. Commissioning began on October 1, 2013, and concluded after three months, on December 31, 2013. The Routine Operations Phase ran from January 1, 2014, to December 31, 2021.

The CASSIOPE/Swarm-E bus has four virtual channels that are available for downlink during a pass. Table 2 gives a description of each virtual channel along with the total amount of data for each channel for the entirety of the mission.

Virtual Channel	Description	Mission Data Volume (GB)
VC0	Science data captured from the e-POP instruments	3117.8
VC4	Back-orbit bus housekeeping information	261.1
VC5	Real-time bus housekeeping information	8.84
VC6	Low-level Unit Manager telemetry	491.78

Table 2: CASSIOPE/Swarm-E Virtual Channel Descriptions and Data Volumes

The number of data acquisition passes per month for the duration of the mission are displayed in Figure 3. The peak at the beginning of the mission corresponds to the start of the Commissioning Phase. For the balance of Commissioning and into Routine Operations there was typically one data acquisition pass per day. In July of 2017, regular operations were increased to two passes per day in anticipation of CASSIOPE being brought into the ESA Third Party Mission (TPM) program as Swarm-Echo. The four-pass-per-day paradigm began in February of 2018 when CASSIOPE officially became Swarm-Echo and entered the TPM program. At the end of Routine Operations, in January 2022, operations fell back to one pass per day. A complete listing of all successful data acquisition passes to October 22, 2023, is listed in

Appendix B.

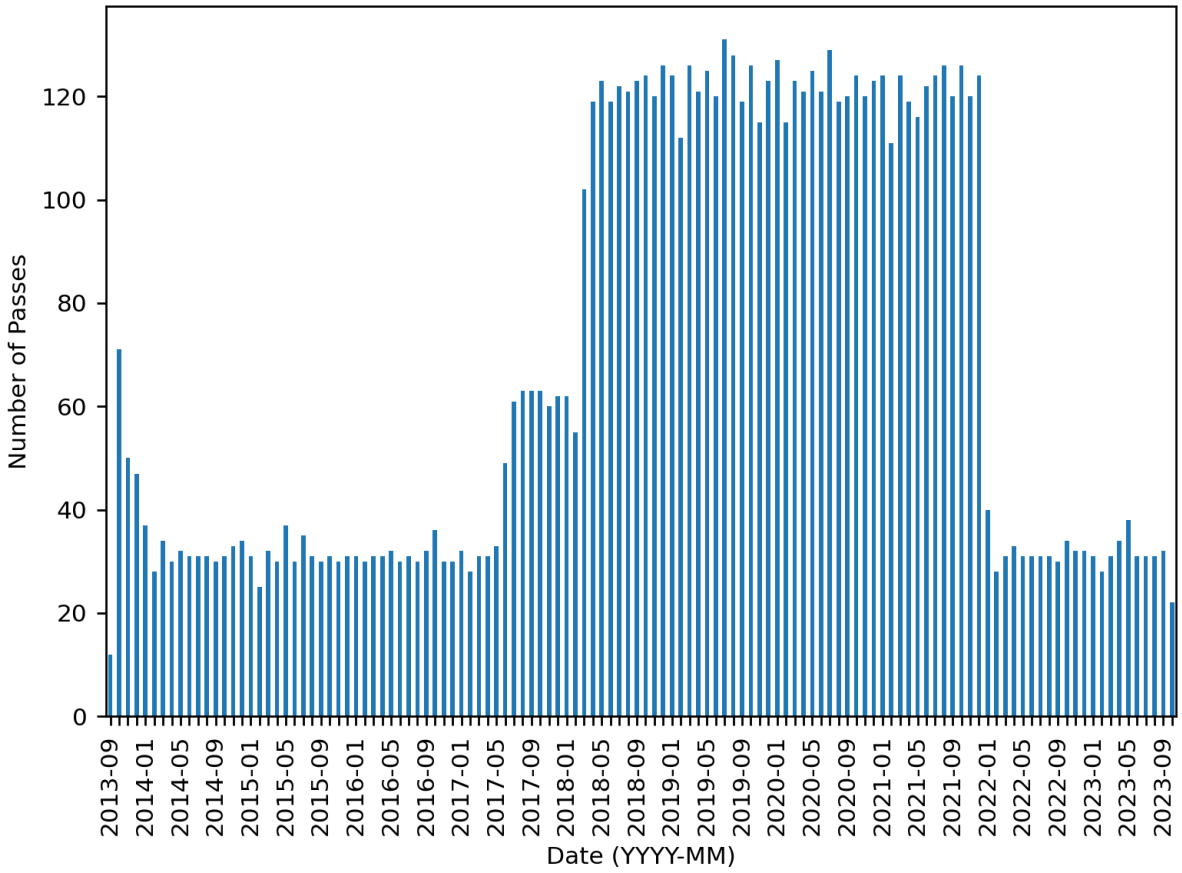

Figure 3: Number of data acquisition passes per month for the duration of the CASSIOPE/Swarm-E mission

3.2 Coordinated Science Campaigns

Throughout the CASSIOPE/Swarm-E mission, coordinated science campaigns were conducted on a regular basis. These campaigns included operation of specific instruments in particular modes, often at prescribed times or locations, in conjunction with another space- or ground-based resource. Table 3 lists the coordinated science campaigns executed during the Routine Operations phase of the mission.

Campaign	Description	Dates
ARRL Field Day	RRI tuned to Ham Radio frequencies over the USA during the American Radio Relay League (ARRL) Field Day	2015-06-28 2017-06-24 to 2017-06-25 2018-06-23 to 2018-06-28 2021-06-26 to 2021-06-27
Ham Radio Frequency Bands	RRI tuned to Ham Radio frequencies over the USA during non-ARRL field days	2015-09-02, 2015-09-05, 2015-10-16 to 2015-10-18
Churchill RRI	Tune RRI to VLF frequencies over instrumentation at Churchill, MB, Canada	2018-10-06, 2018-10-07, 2018-10-12, 2018-10-14 to 2018-11-16
Lucky Lake RRI	Tune RRI to VLF frequencies over Lucky Lake, SK, Canada	347 dates between 2018-09-18 and 2021-01-08. See

		edex.phys.ucalgary.ca for a complete listing.
FAI imaging of resident space objects	Image resident space objects using FAI by pointing the camera towards the stars	146 dates between 2022-11-27 and 2023-10-03. See edex.phys.ucalgary.ca for a complete listing.
Frequency Limited Acoustic Shock (FLASH) measurements	Use RRI to detect plasma waves from closely passing resident space objects	75 dates between 2022-03-27 and 2023-10-25. See edex.phys.ucalgary.ca for a complete listing.
DSX satellite	Conjunctions with the DSX satellite where the DSX transmitter was operating	177 dates between 2019-09-06 and 2021-02-28. See edex.phys.ucalgary.ca for a complete listing.
DMSP satellites	Conjunctions with a DMSP satellite	657 dates between 2014-10-11 and 2022-01-03. See edex.phys.ucalgary.ca for a complete listing
Cygnus spacecraft	Conjunctions with the Cygnus International Space Station resupply spacecraft	2018-07-22, 2020-05-25, 2020-05-26
Cluster satellites	Conjunctions with a Cluster satellite	2014-10-12, 2014-10-15
ICI-4 rocket launch	Attempted conjunctions with the launch of the ICI-4 rocket from Andøya, Norway	2015-02-02, 2015-02-08 to 2015-02-20
RENU2 rocket launch	Attempted conjunctions with the launch of the RENU2 rocket from Andøya, Norway	2015-11-29 to 2015-12-14
TechDemoSat satellite	Conjunctions with the TechDemoSat satellite	2014-10-22, 2014-10-24, 2014-10-30, 2014-11-01
ZACUBE-1 satellite	Conjunctions with the ZACUBE-1 satellite	2014-10-16, 2014-10-18, 2014-10-19, 2014-10-21, 2014-10-25, 2014-10-26, 2014-10-28, 2014-11-15 to 2014-11-17, 2016-09-01, 2016-09-06, 2016-09-12, 2016-09-14, 2016-09-16
ICEBEAR radar	Conjunctions with the ICEBEAR radar near Saskatoon, SK, Canada	81 dates between 2018-03-07 and 2021-03-02. See edex.phys.ucalgary.ca for a complete listing.
Swarm satellites	Conjunctions between Swarm-A/C or Swarm-B satellites	1507 dates between 2014-10-06 and 2021-11-30. See edex.phys.ucalgary.ca for a complete listing.
AUTUMNX	Intentional overflights of the AUTUMNX receiver chain in Québec, Canada	44 dates between 2016-04-02 and 2016-05-31. See edex.phys.ucalgary.ca for a complete listing.
CARISMA array	Intentional overflights of the CARISMA array in western Canada	42 dates between 2014-10-17 and 2016-02-22. See

		edex.phys.ucalgary.ca for a complete listing.
Saskatoon SuperDARN	Coordinated operation of the Saskatoon SuperDARN radar and CASSIOPE/Swarm-E instruments	284 dates between 2014-01-02 and 2023-02-21
WWV transmitter	Conjunctions with the high-power WWV HF transmitter near Fort Collins, CO, USA	2017-07-20 to 2017-07-22, 2017-08-15 to 2017-08-18, 2017-10-17, 2017-10-17, 2017-10-22 to 2017-10-24, 2019-05-15 to 2019-05-19, 2019-05-26 to 2019-06-02
BPM time signal transmitter	Conjunctions with the HF BPM time signal transmitter in Pucheng, China	2020-06-14, 2020-06-21
Kharkiv ISR	Conjunctions over the incoherent scatter radar at Kharkiv, Ukraine	2020-06-21, 2020-06-23, 2020-06-24
DHO38 transmitter	Passes over the DHO38 VLF transmitter near Rhauderfehn, Germany	2016-01-16, 2016-01-17, 2016-03-05
CODAR	Conjunctions with the Coastal Ocean Dynamics Applications Radar (CODAR) systems	43 dates between 2016-02-01 and 2018-09-15. See edex.phys.ucalgary.ca for a complete listing
Toolik Lake	Passes over instrumentation at Toolik Lake, AK, USA	62 dates between 2014-11-14 and 2018-11-17. See edex.phys.ucalgary.ca for a complete listing.
Clyde River SuperDARN	Coordinated operation of the Clyde River, NU, Canada SuperDARN radar and CASSIOPE/Swarm-E	45 dates between 2017-04-22 and 2020-10-13. See edex.phys.ucalgary.ca for a complete listing.
CHU station	Passes over the CHU radio station near Ottawa, ON, Canada	2017-07-21 and 2017-07-22
Cambridge Bay CADI	Passes over the Cambridge Bay, ON, Canada Canadian Advanced Digital Ionosonde (CADI)	2017-07-01 to 2017-07-04, 2017-08-13 to 2017-08-15, 2017-10-01 to 2017-10-02
Arecibo transmitter	Passes over the Arecibo, Puerto Rico HF transmitter	67 dates between 2015-11-13 and 2020-04-03. See edex.phys.ucalgary.ca for a complete listing.
TIGER SuperDARN	Passes over the TIGER SuperDARN radar in southern Australia and New Zealand	2015-11-02, 2015-11-02
Sura heater	Coordinated operation of the Sura Ionospheric heater, located near Vasilsursk, Russa, and CASSIOPE/Swarm-E	59 dates between 2014-10-03 and 2018-11-29. See edex.phys.ucalgary.ca for a complete listing.
Sondrestrom ISR	Conjunctions with the incoherent scatter radar facility at Sondrestrom, Greenland	94 dates between 2015-08-19 and 2017-12-21. See edex.phys.ucalgary.ca for a complete listing.

Resolute Bay radar	Coordinated operation of the HF transmitter at Resolute Bay, NU, Canada, and CASSIOPE/Swarm-E	663 dates between 2016-10-29 and 2020-02-28. See edex.phys.ucalgary.ca for a complete listing.
NLK transmitter	Conjunctions with the NLK VLF transmitter near Oso, WA, USA	17 dates between 2016-01-16 and 2019-01-18. See edex.phys.ucalgary.ca for a complete listing.
NWC transmitter	Conjunctions with the NWC VLF transmitter near Exmouth, Western Australia	22 dates between 2016-01-22 and 2019-01-24. See edex.phys.ucalgary.ca for a complete listing.
Ottawa NRCan transmitter	Conjunctions with the Natural Resources Canada HF transmitter near Ottawa, ON, Canada	82 dates between 2015-05-08 and 2018-02-16. See edex.phys.ucalgary.ca for a complete listing.
NAA transmitter	Conjunctions with the NAA VLF transmitter near Cutler, ME, USA	2016-01-18, 2016-01-09, 2016-03-05
Millstone Hill	Coordinated operation of the Millstone Hill incoherent scatter radar	2017-04-21, 2017-04-28
Prince George SuperDARN	Conjunctions with the SuperDARN radar at Prince George, BC, Canada	2018-04-11, 2018-04-13
Rankin Inlet SuperDARN	Conjunctions with the SuperDARN radar at Rankin Inlet, NU, Canada	2016-08-02 to 2016-08-05, 2018-02-15 to 2018-02-17
Kodiak SuperDARN	Conjunctions with the SuperDARN radar at Kodiak, AK, USA	2018-04-12, 2018-04-13
Hankasalmi SuperDARN	Conjunctions with the SuperDARN radar at Hankasalmi, Finland	9 dates between 2016-07-16 and 2017-04-23. See edex.phys.ucalgary.ca for a complete listing.
HAARP	Coordinate operations with the HAARP ionospheric heater	64 dates between 2017-02-19 and 2023-08-15. See edex.phys.ucalgary.ca for a complete listing.
EISCAT Tromso	Coordinated operations with the ionospheric heater at Tromso, Norway	29 dates between 2015-03-09 and 2020-06-24. See edex.phys.ucalgary.ca for a complete listing.
EISCAT Svalbard	Coordinated operations with the EISCAT facilities at Svalbard, Norway	37 dates between 2014-11-09 and 2016-12-15. See edex.phys.ucalgary.ca for a complete listing.
RISR	Coordinated operations with the Resolute Bay incoherent scatter radars (RISR-N or RISR-C)	110 dates between 2015-02-11 and 2019-08-30. See edex.phys.ucalgary.ca for a complete listing.

Table 3: Coordinated Science Campaigns during the CASSIOPE/Swarm-E mission

3.3 CONFIGURATION CHANGES

Table 4 below lists the configuration changes for the CASSIOPE/Swarm-E bus and the e-POP instruments.

Affected system	Description	Date
MGF	MGF flight software update from version 1.2 to 1.3 to fix ring transients caused by an unintended timing variation between when the magnetic feedback to the sensor is updated and when the next sample is taken.	2014-04-10 (inboard sensor) 2014-04-22 (outboard sensor)
ADCS	ADCS reaction wheels' default spin rate reduced from 100 rad/s to 0 rad/s. This was in response to reaction wheel #4 seizing and being shut off, leaving only three running reaction wheels.	2016-08-12
GAP-A receivers	Removal of the NovAtel SATXYZ and PSRPOS messages from the default set of messages sent by the GAP-A receivers. The default messages remaining are the RANGE and PSRXYZ messages. This was done to reduce the number of lost packets from the GAP-A receivers due to bottlenecking.	2017-11-22
GAP GPS-1 and GPS-3 receivers	The GAP GPS-1 receiver failed and was replaced by the cold spare GPS-3 unit.	2018-09-16
GAP GPS-4 receiver	The GAP GPS-4 receiver was re-programmed to have a default message rate at startup of 20 Hz, rather than 50 Hz	2019-01-10
GAP GPS-3 receiver	The GAP GPS-3 receiver was re-programmed to output the RANGE and PSRXYZ NovAtel GPS messages at startup. Previously it output only the RANGECMP message by default.	2019-01-22
GAP	The GAP primary flight software image EEPROM failed. Transition was made to boot from the secondary EEPROM that contains a copy of the same flight software.	2021-02-23
ADCS	The spacecraft was put into a sun-pointing attitude in response to the failure of Reaction Wheel #1	2021-02-27
ADCS	Achieved a modified nadir-pointing attitude using an ADCS solution that requires only two wheels	2021-09-16
ADCS	The spacecraft was put into a permanent sun-pointing attitude using only the magnetic torque rods, in response to the failure of Reaction Wheel #3	2021-12-17

Table 4: Configuration changes to the CASSIOPE/Swarm-E bus and e-POP payload

3.4 LONG-TERM TRENDING

Records of spacecraft and e-POP instrument housekeeping values over the course of the mission are displayed in Figures Figure 4 - Figure 16 below. Other than the e-POP instrument current draw graphs, all plots show the maximum, minimum, and average values for comparison. Distinct changes in long-term trends in 2021, particularly in temperatures and solar panel voltages, are associated with the transition to a permanent sun-pointing attitude. Table 5 is provided below for proper interpretation of the plots in Figure 13.

Power Control Unit Values	Physical Solar Panel Array Connections
Panel Voltage 1	½ Top Solar Panel
Panel Voltage 2	Anti-Ram +Y Panel, Ram -Y Panel
Panel Voltage 3	Anti-Ram -Y Panel, Ram +Y Panel
Panel Voltage 4	½ Top Solar Panel

Table 5: Solar Panel to Power Control Unit Connections

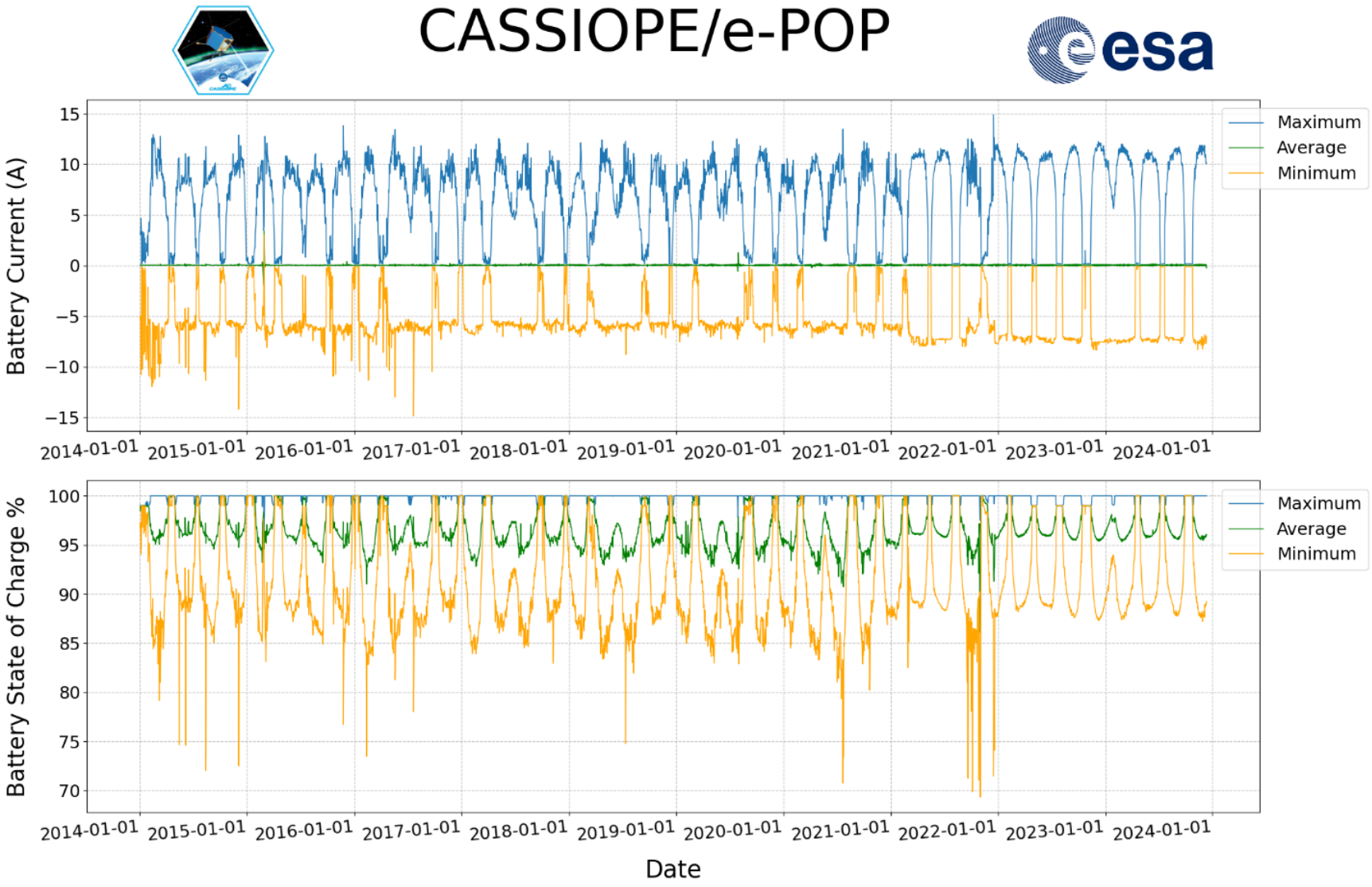

Figure 4: CASSIOPE/Swarm-E battery current (top) and battery state of charge (bottom)

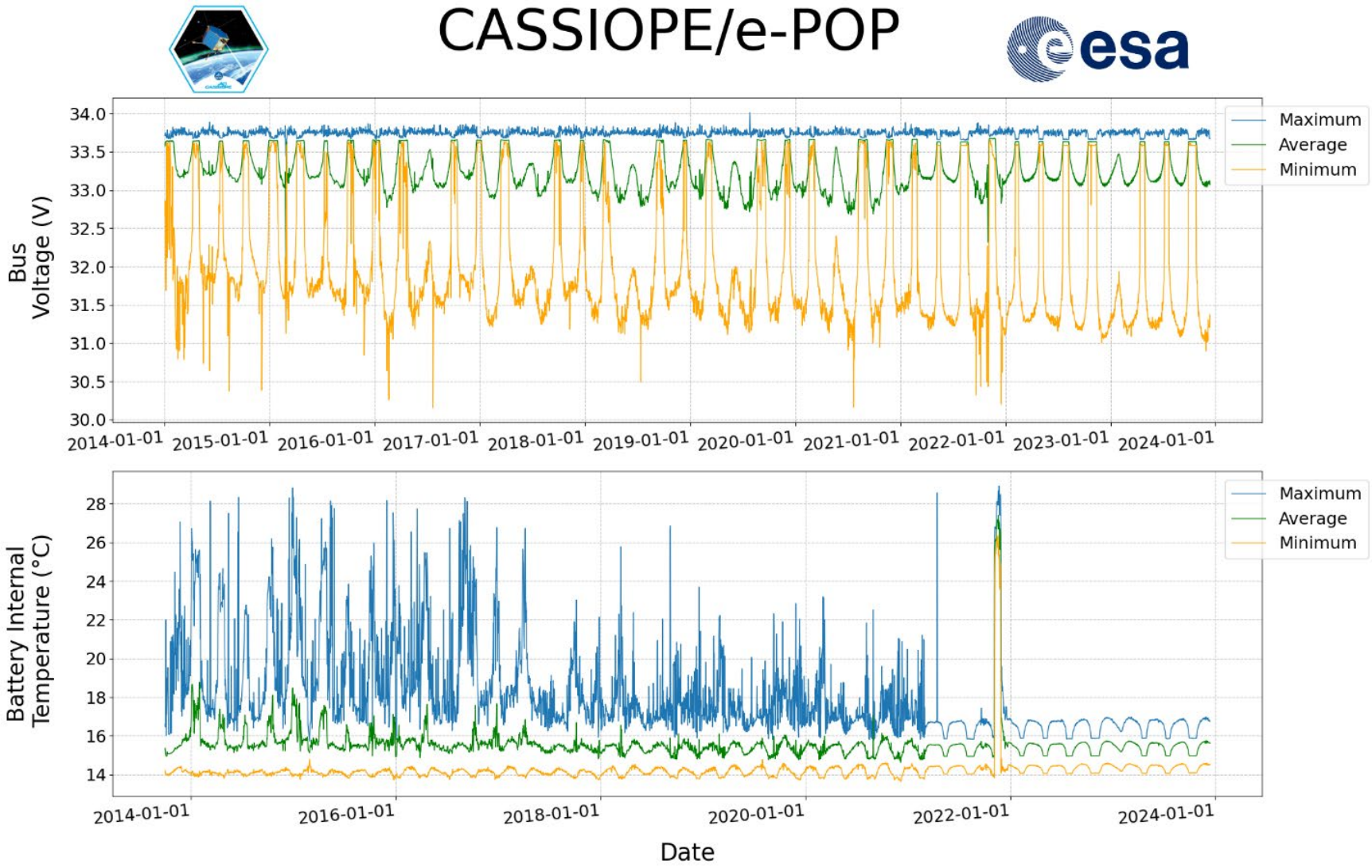

Figure 5: CASSIOPE/Swarm-E bus voltage (top) and internal battery temperature (bottom)

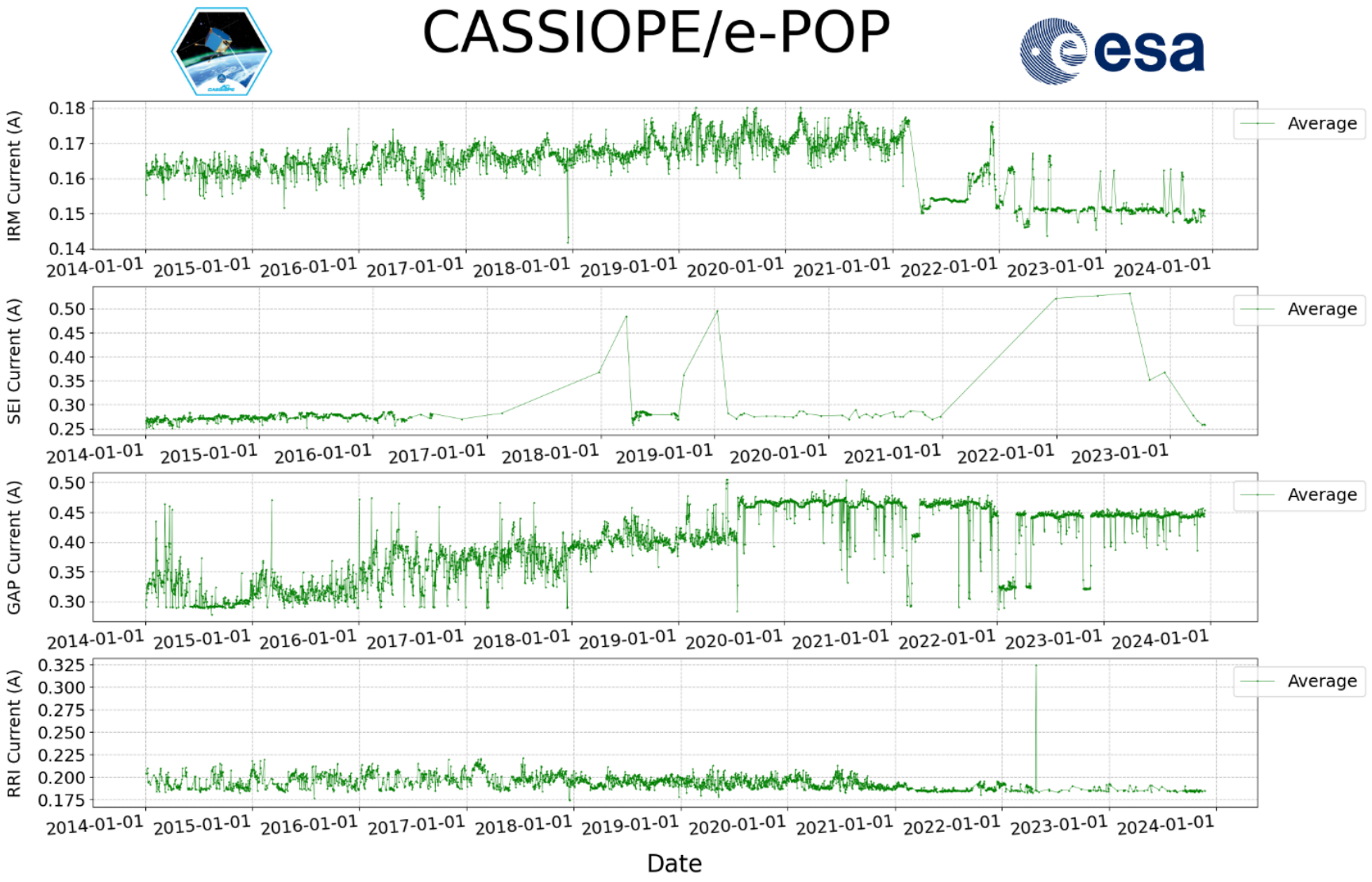

Figure 6: e-POP instrument current draw for (top-to-bottom) IRM, SEI, GAP, and RRI

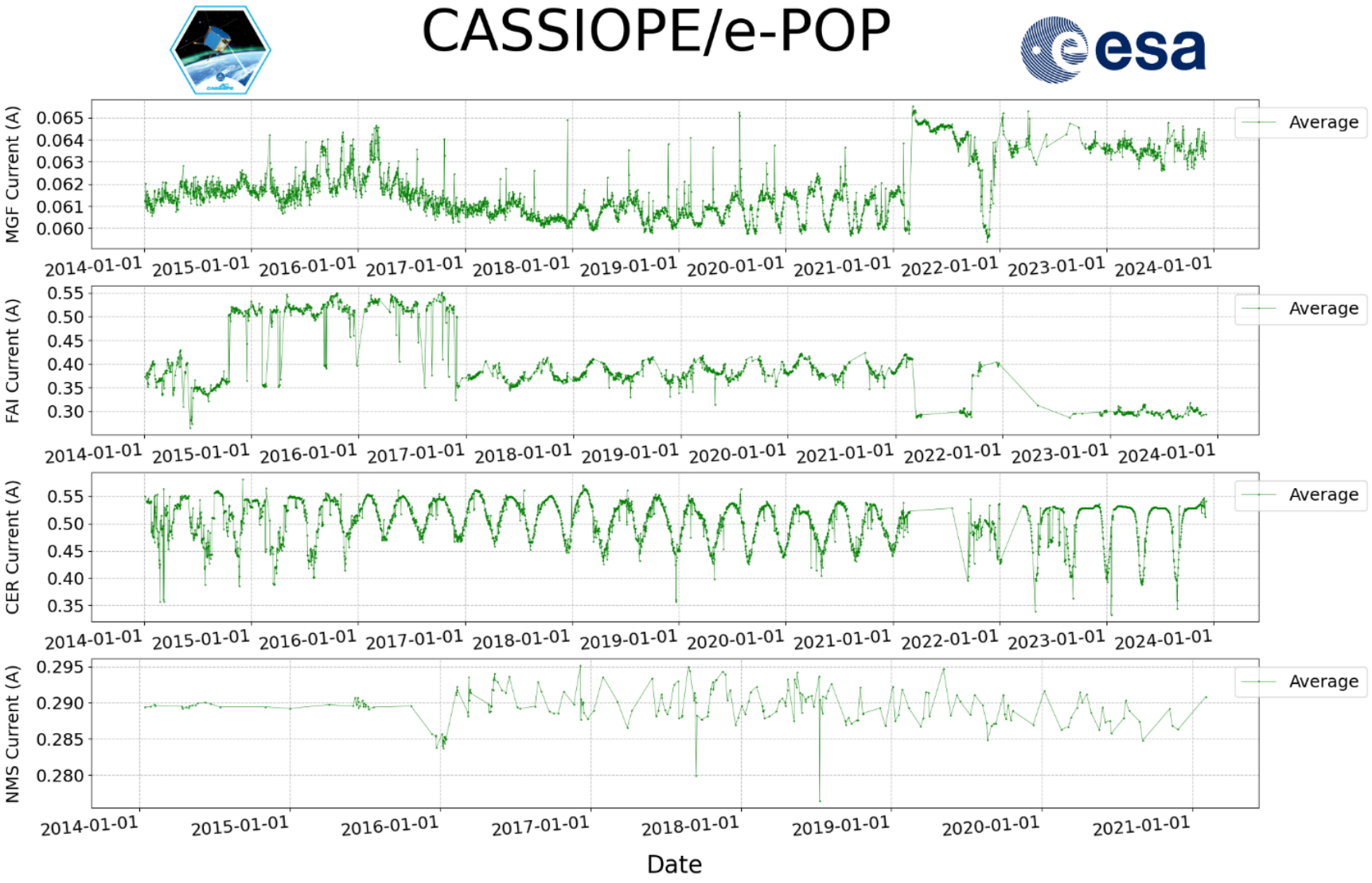

Figure 7: e-POP instrument current draw for (top-to-bottom) MGF, FAI, CER, and NMS

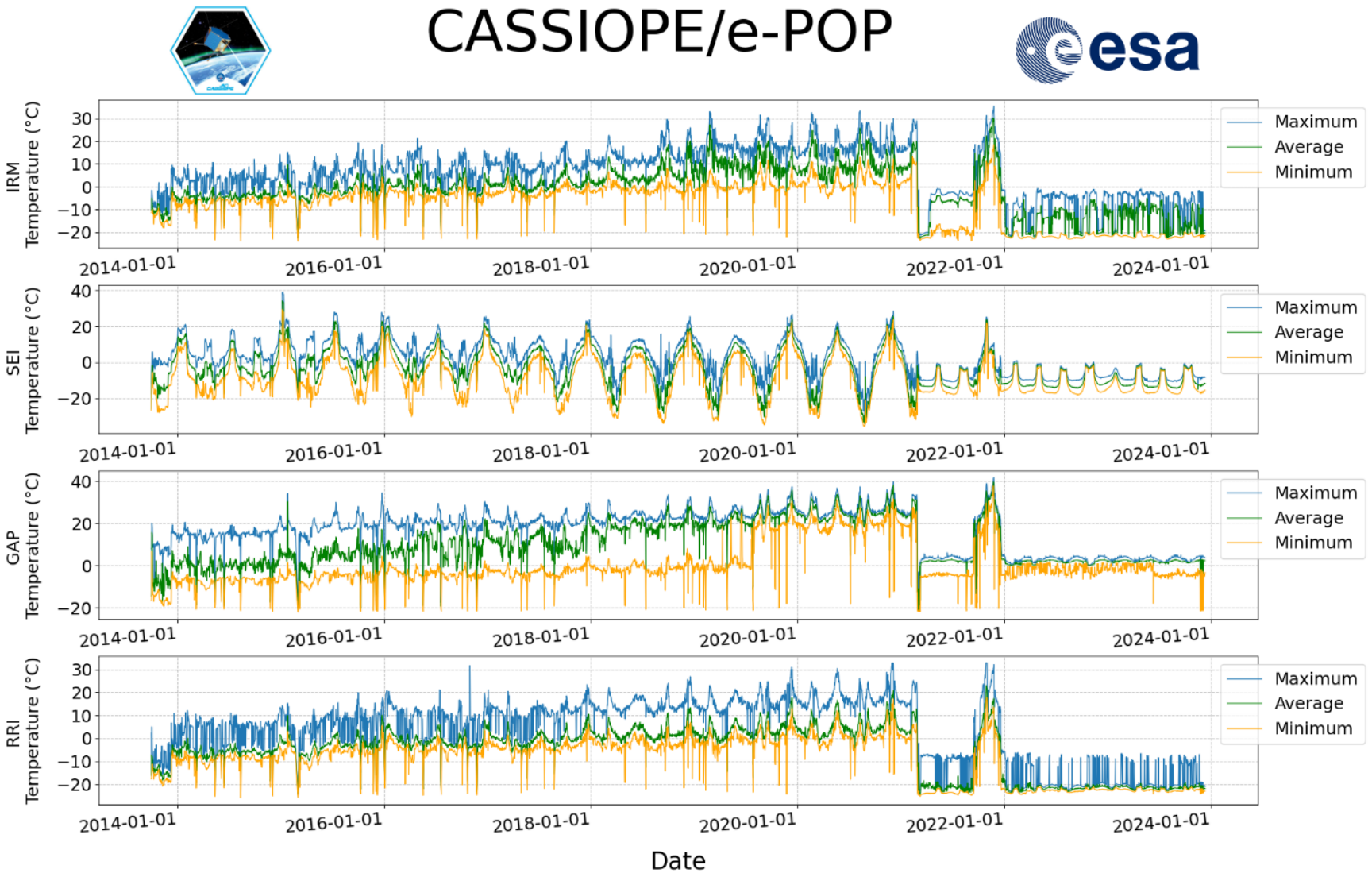

Figure 8: Temperatures for (top-to-bottom) IRM, SEI, GAP, and RRI. The thermistor for each instrument is located on a board inside the respective electronics box, except for SEI where the thermistor is in the sensor head at the end of the SEI boom.

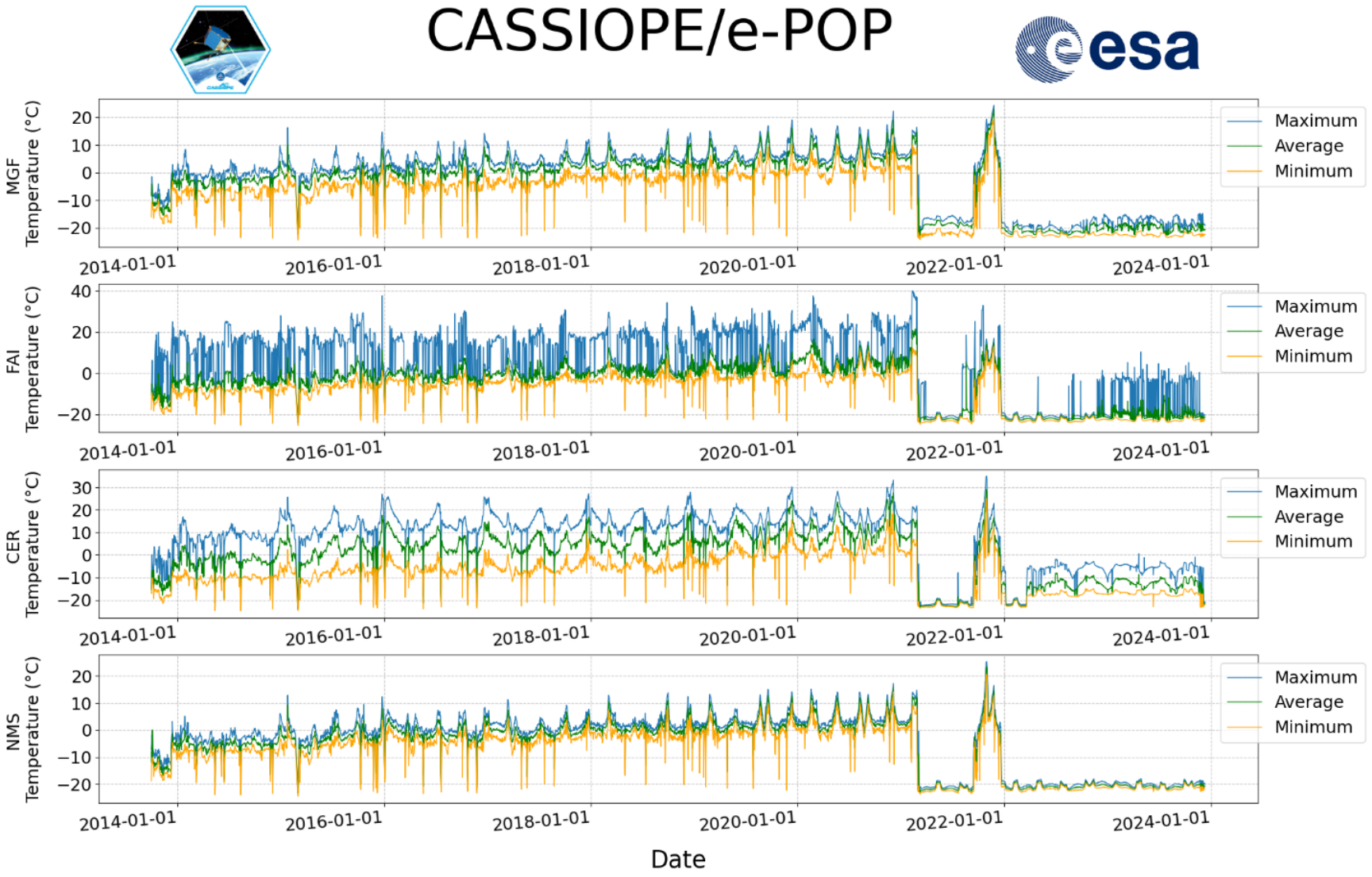

Figure 9: Temperatures for (top-to-bottom) MGF, FAI, CER, and NMS. The thermistor for each instrument is located on a board inside the respective electronics box.

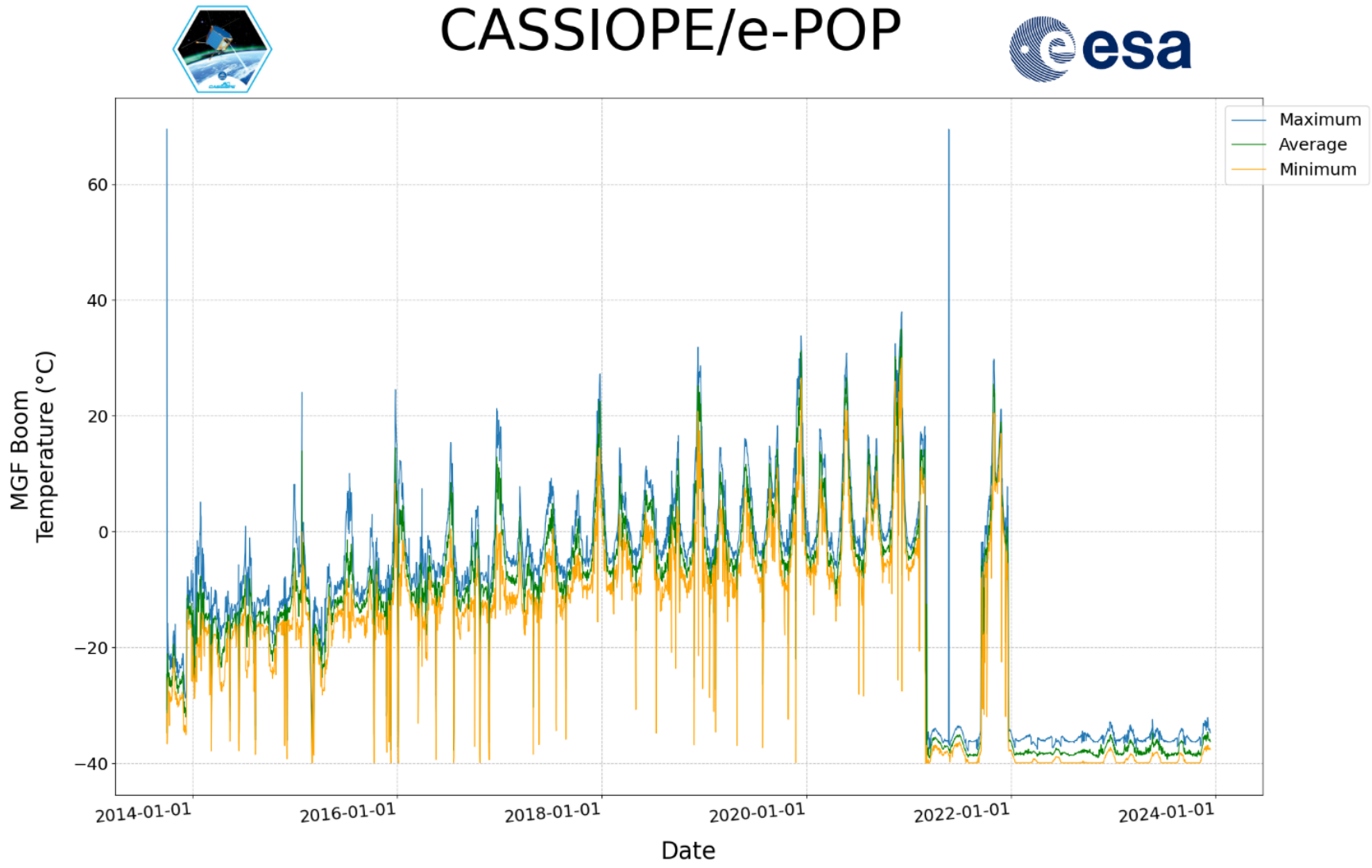

Figure 10: Temperature of the MGF boom between the two MGF sensor heads

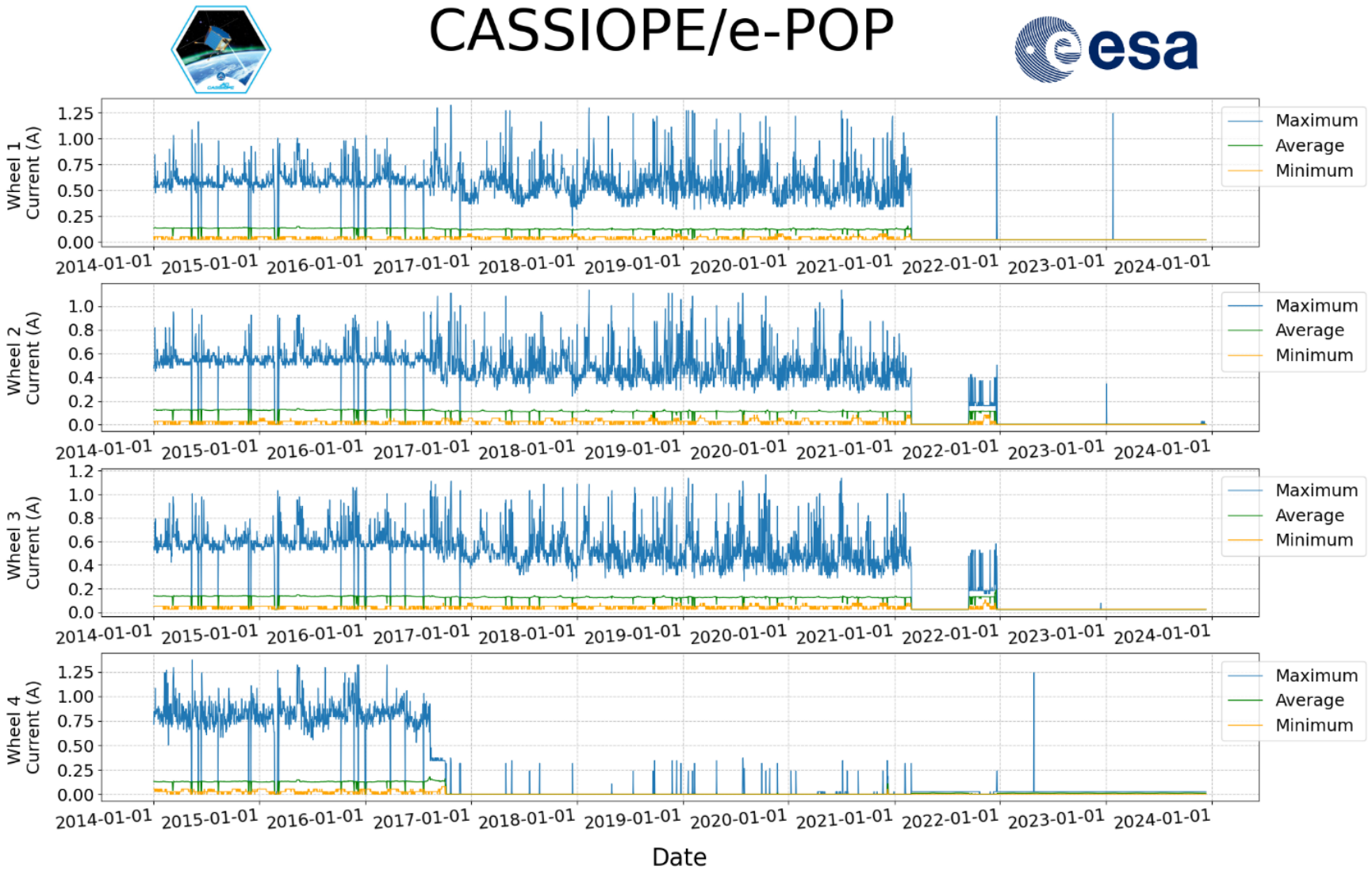

Figure 11: Current draw from the CASSIOPE/Swarm-E reaction wheels

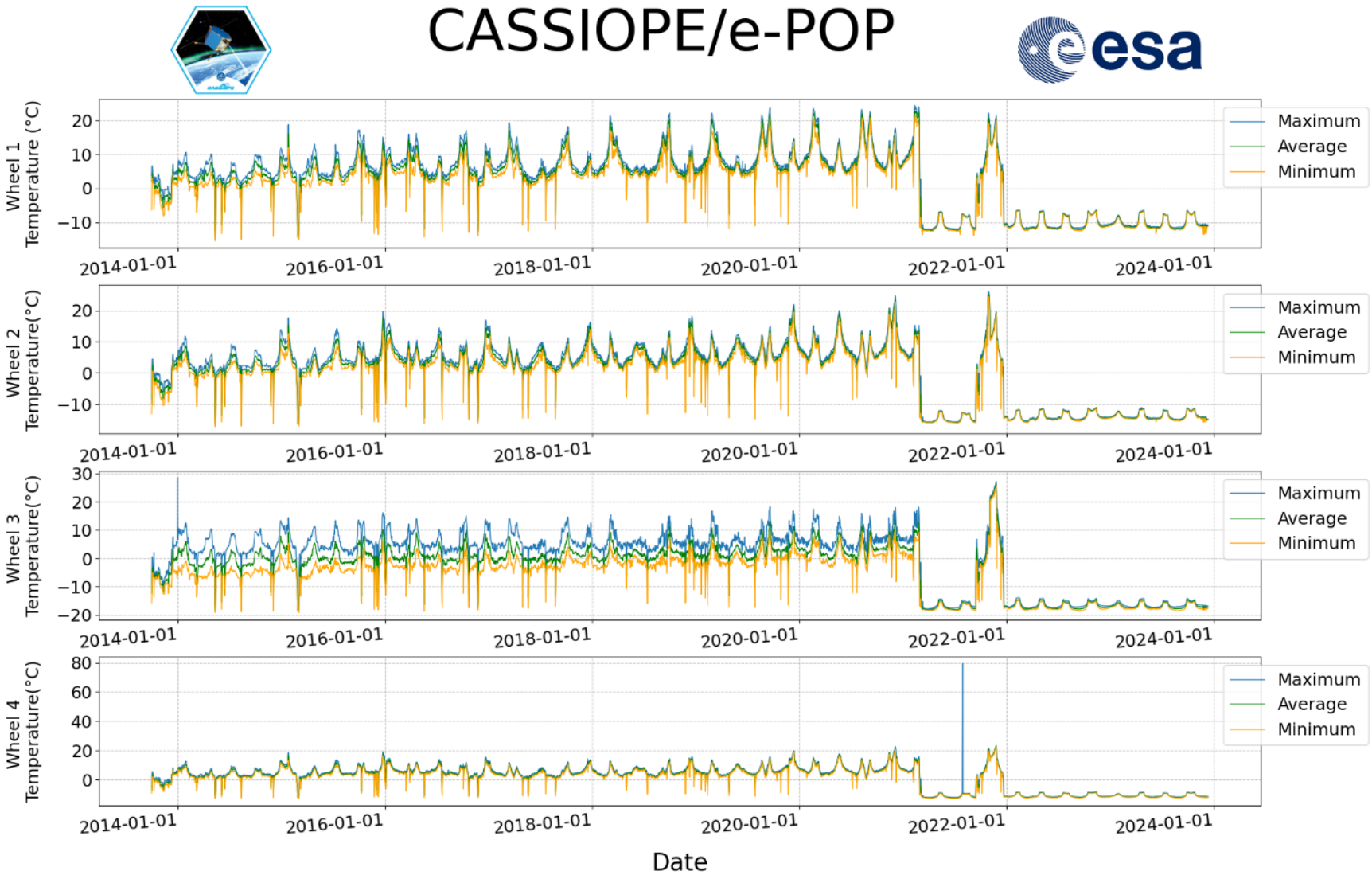

Figure 12: Temperatures of the CASSIOPE/Swarm-E reaction wheels

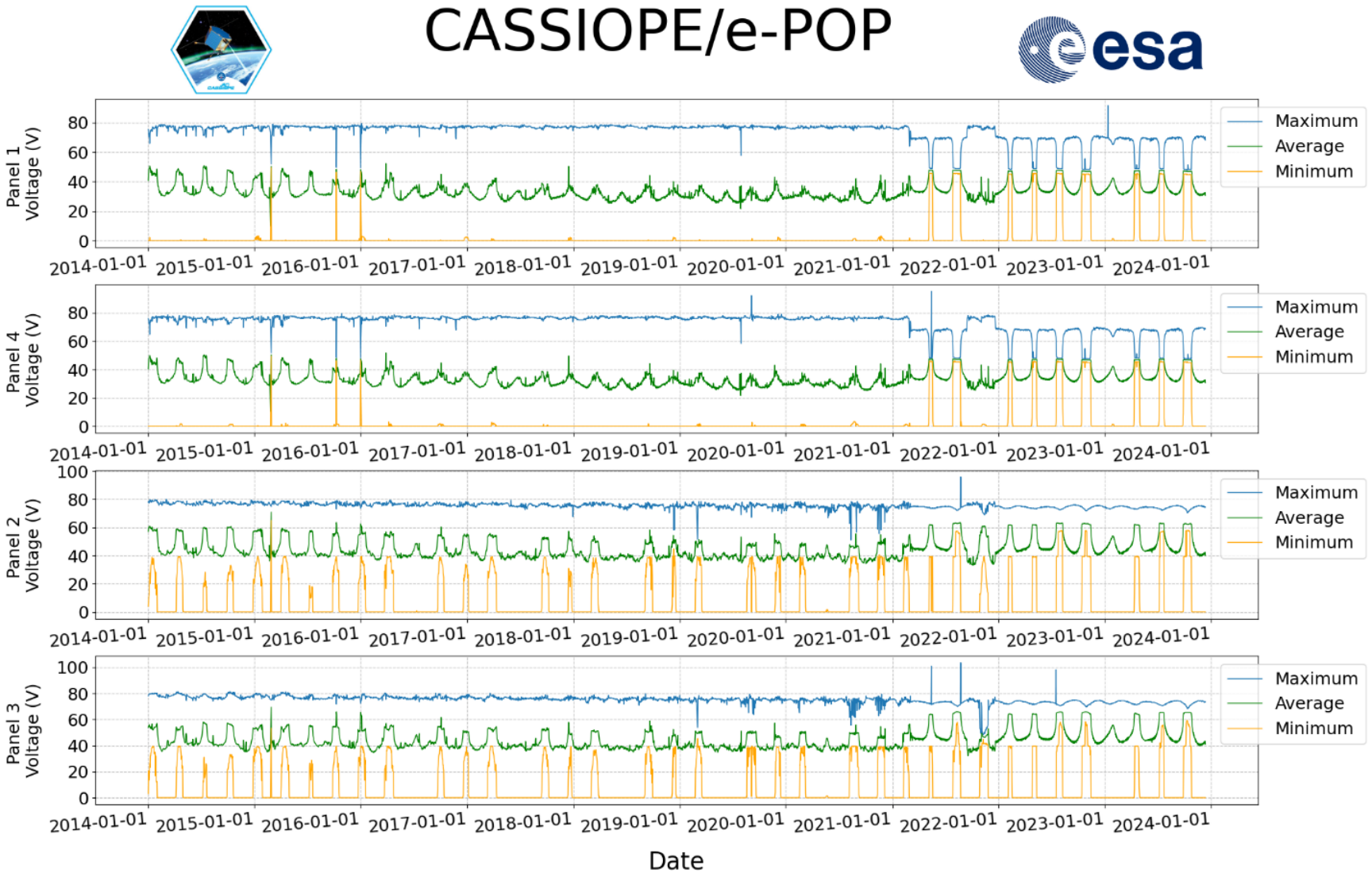

Figure 13: Voltages of the solar charging system. Note that the five physical solar panels map to the four voltages in the plots above according to Table X.

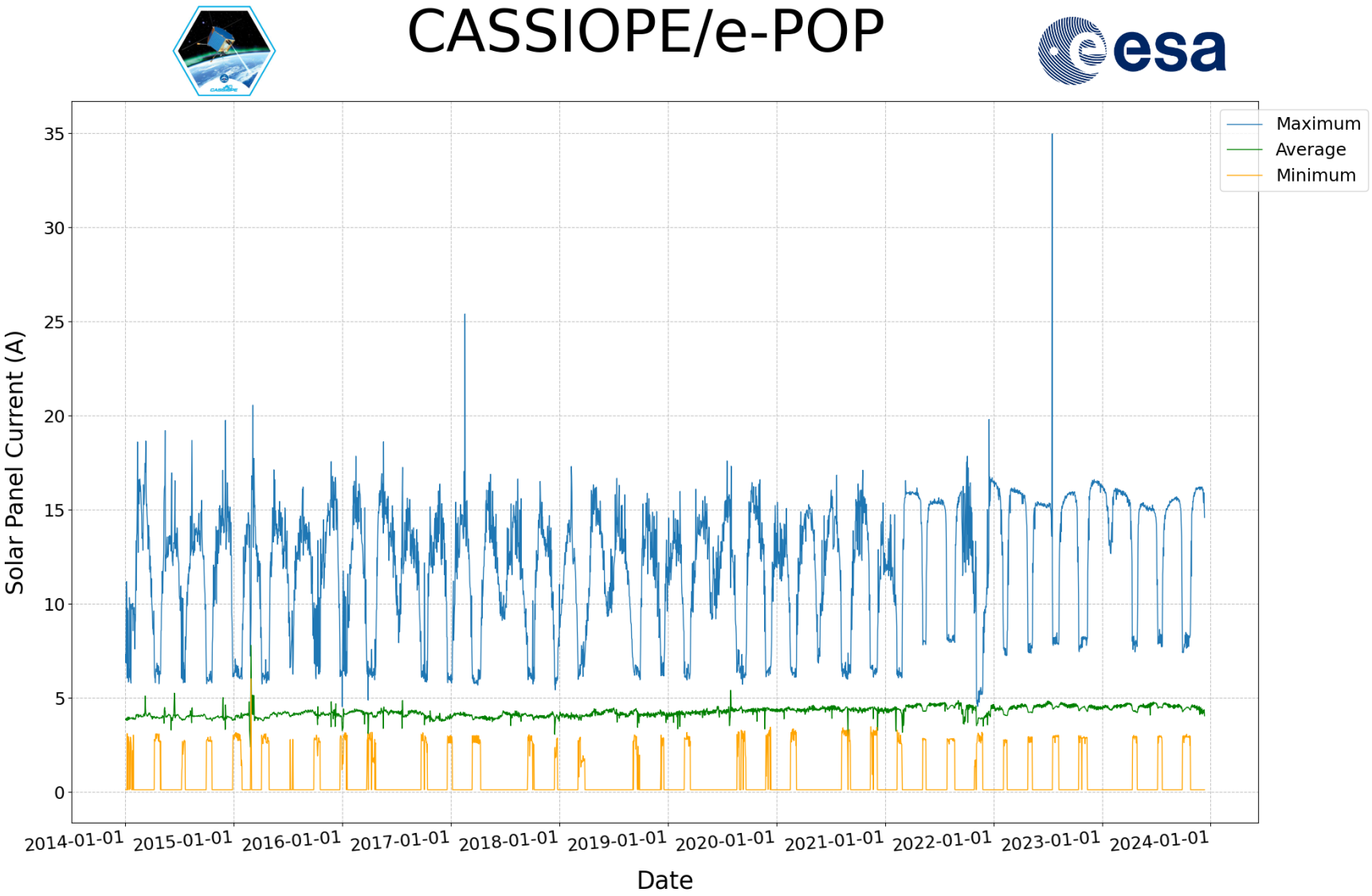

Figure 14: Total solar panel system current for CASSIOPE/Swarm-E

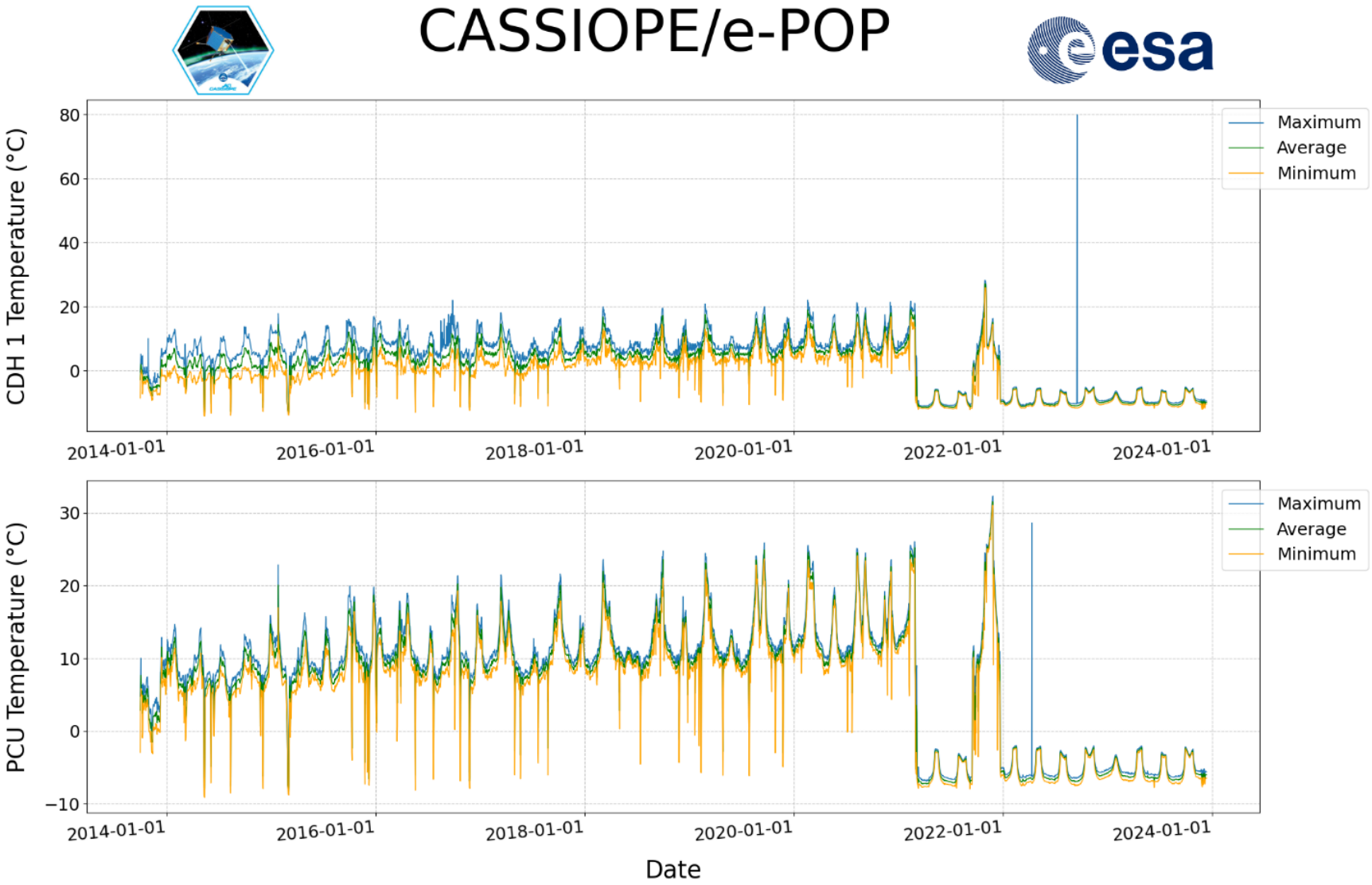

Figure 15: Command and Data Handling Unit (CDH) 1 internal temperature (top) and the Power Control Unit (PCU) temperature (bottom) on CASSIOPE/Swarm-E

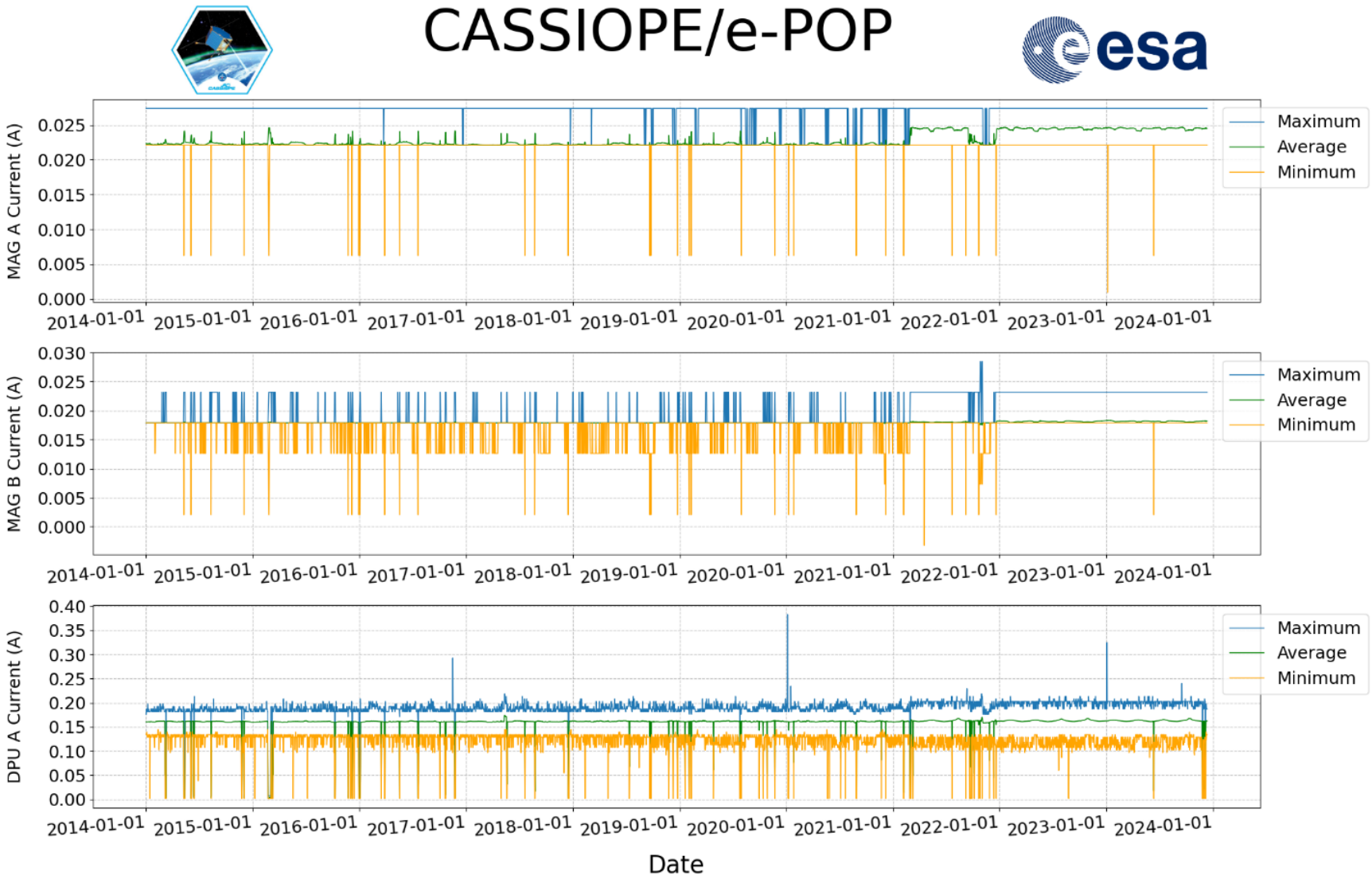

Figure 16: Top-to-bottom: Bus Magnetometer A current draw, Bus Magnetometer B current draw, and Star Tracker Digital Processing Unit (DPU) current draw for CASSIOPE/Swarm-E

4 SCIENCE OBSERVATIONS

4.1 OBSERVATIONAL STATISTICS

The amount of data captured by the e-POP instruments over the mission varies based on numerous factors including the number of ground contact sessions per day, orbit plane configuration, attitude control system status, and more. Figure 17 to Figure 23 below are charts of the monthly data volumes per instrument, in GB (except for FAI where the plot shows the number of images per month). Unsurprisingly, RRI gathered the most data per month over the mission owing to its 4.9 Mb/s data collection rate.

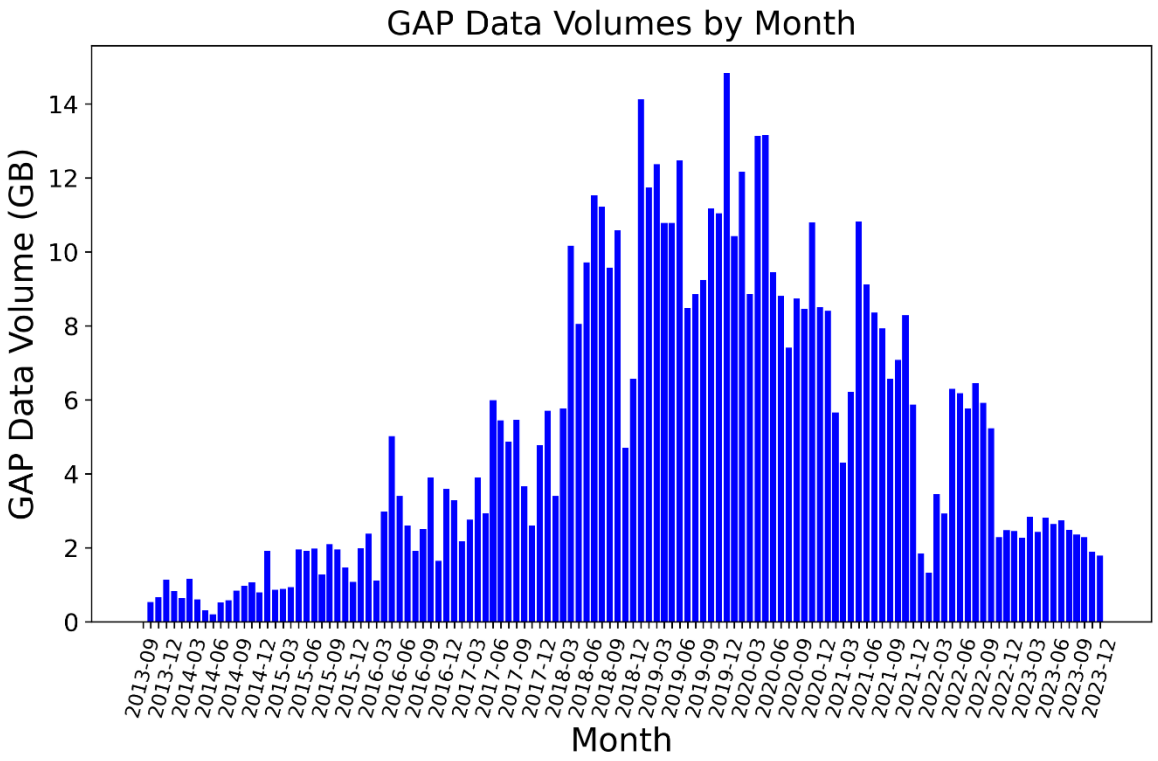

Figure 17: GAP data volumes by month

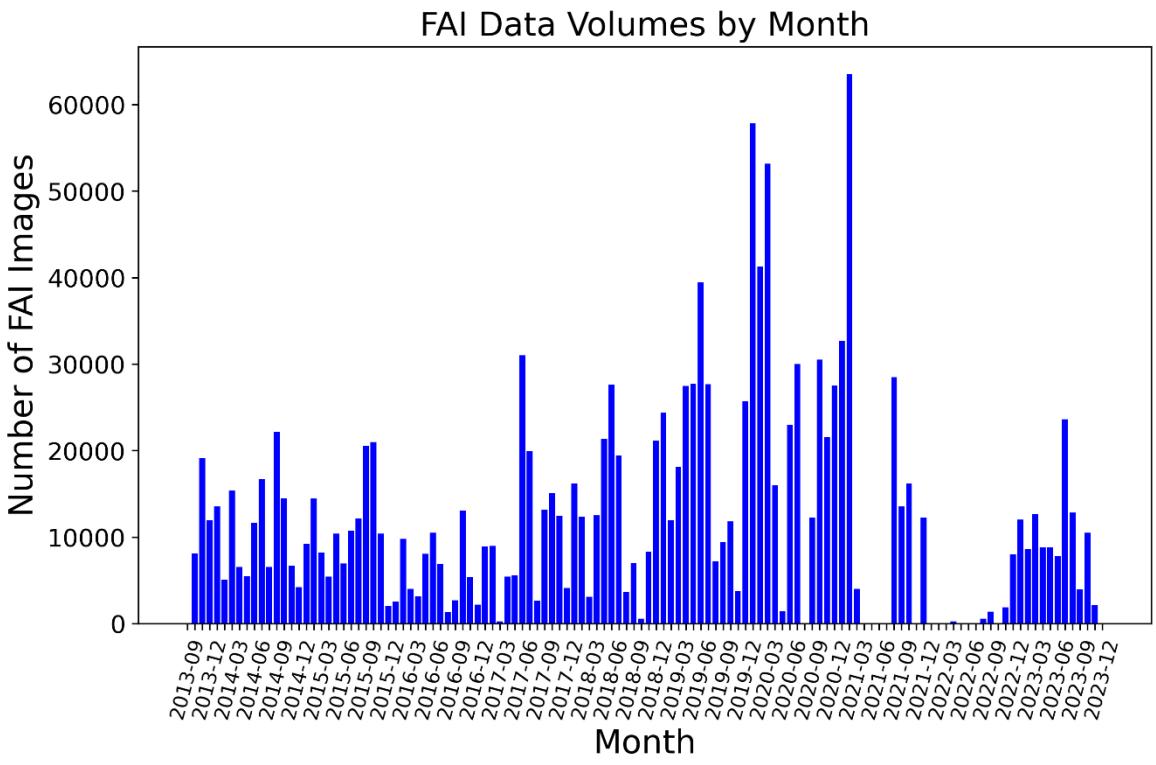

Figure 18: Number of FAI images per month

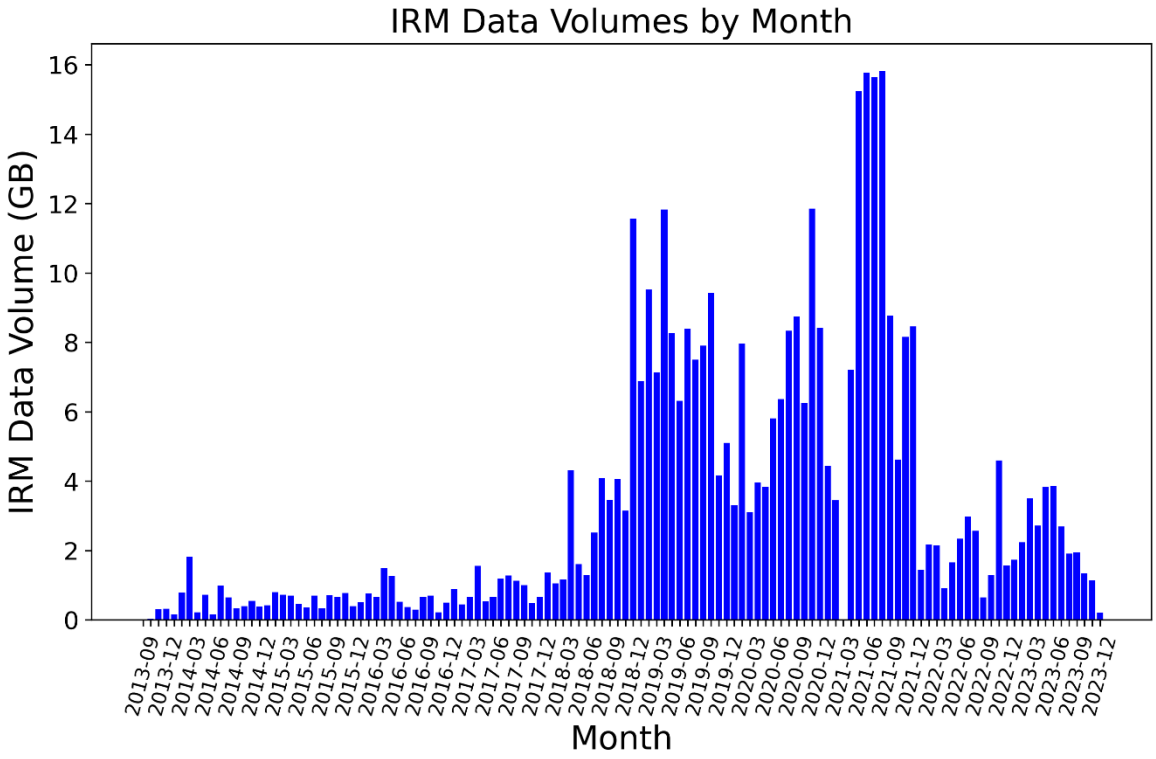

Figure 19: IRM data volumes by month

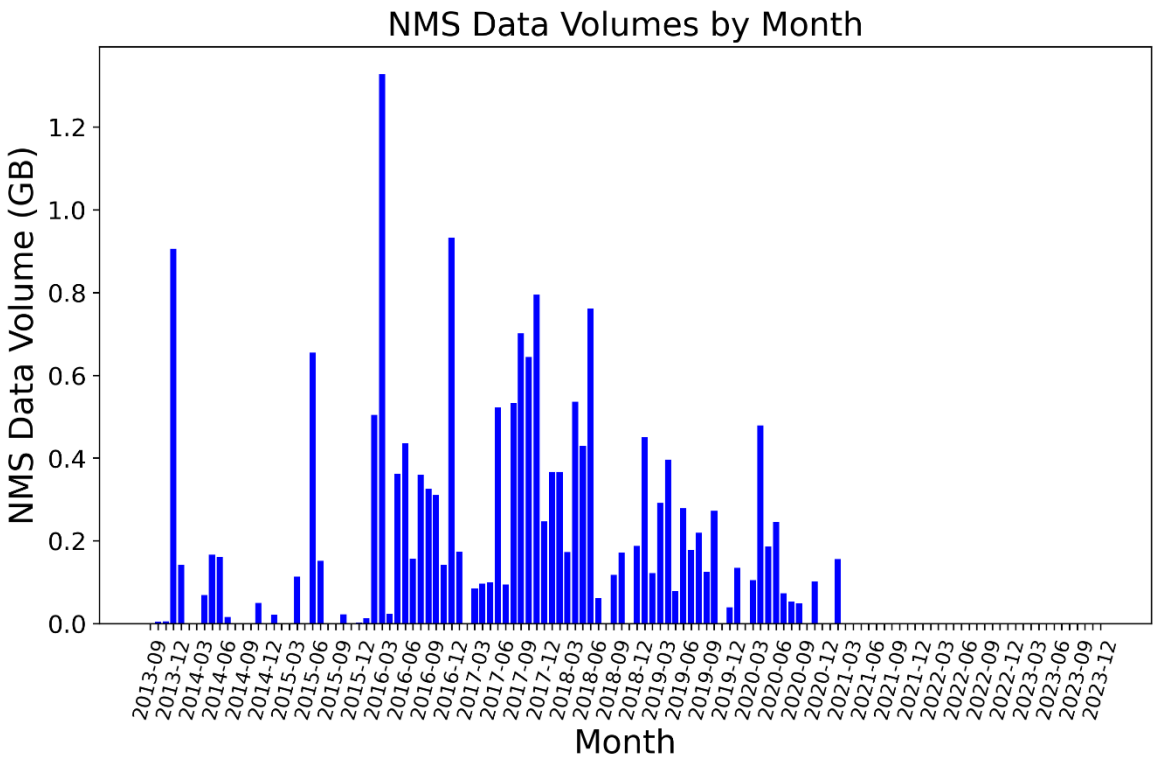

Figure 20: NMS data volumes by month

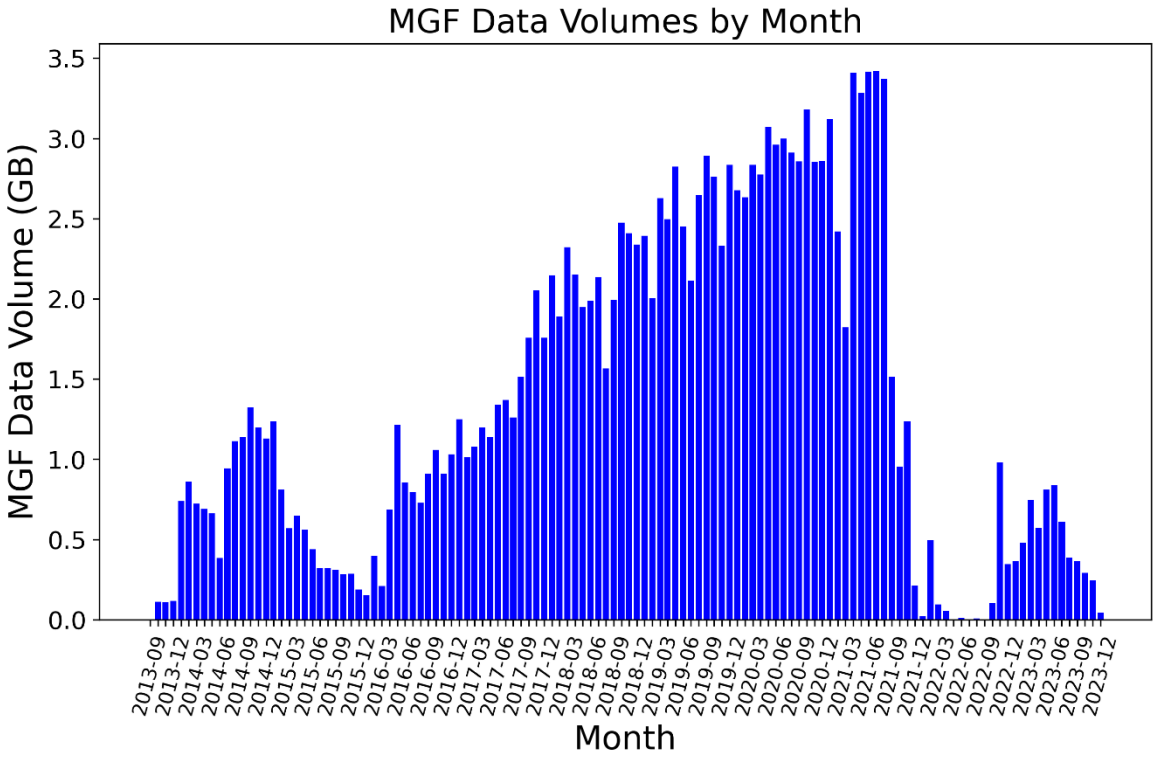

Figure 21: MGF data volumes by month

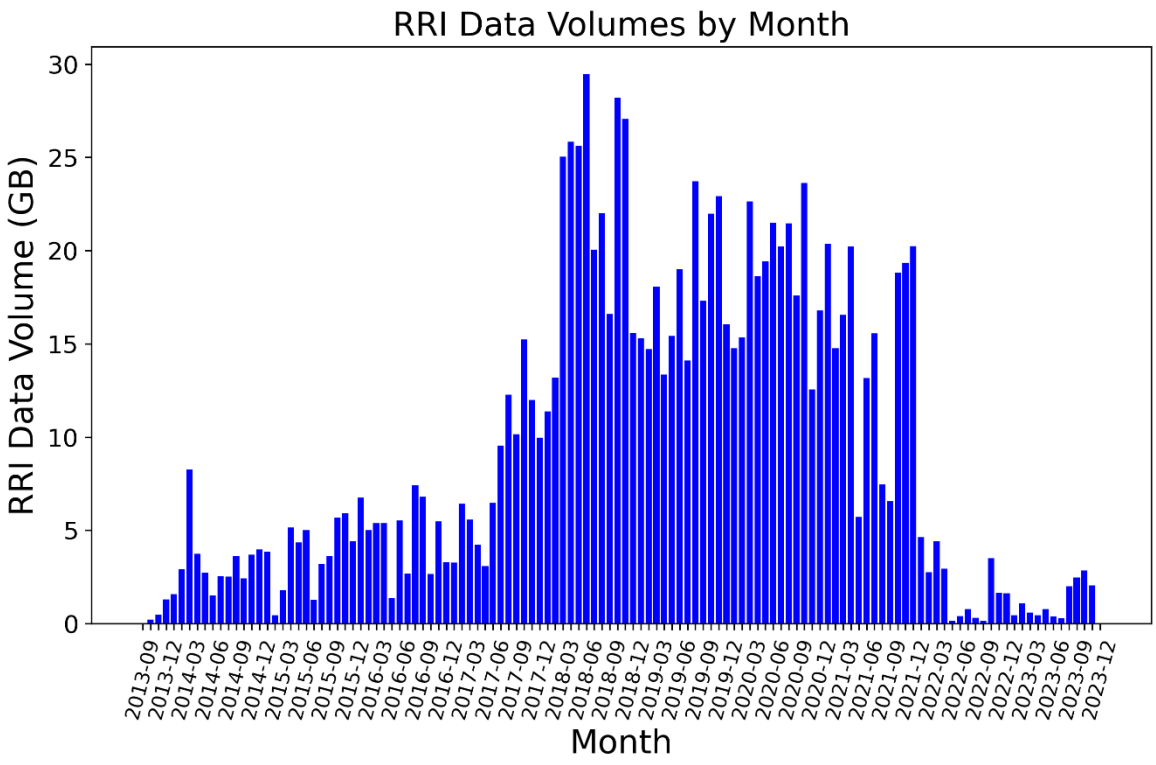

Figure 22: RRI data volumes by month

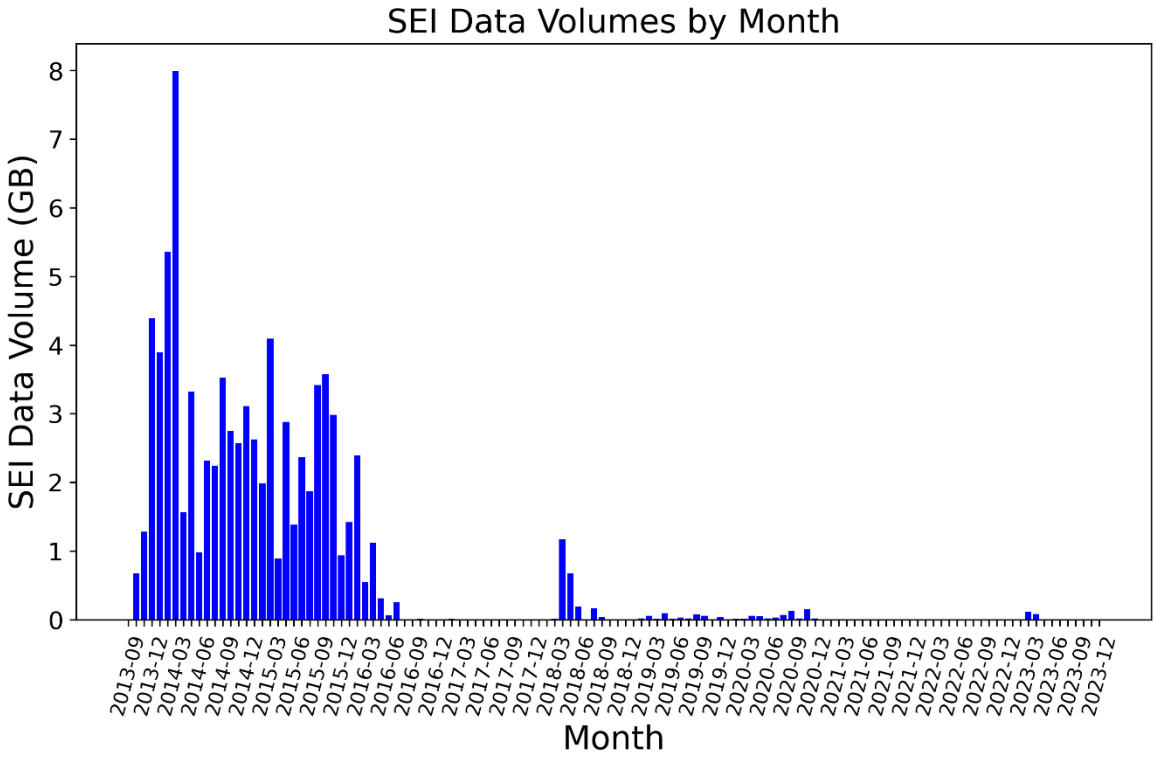

Figure 23: SEI data volumes by month

4.2 DATA COVERAGE

Geographic coverage of scientific measurements is an important metric when searching for and analyzing data. Figure 24 to Figure 104 show the yearly geographic coverage for each of FAI, GAP-A, GAP-O, IRM, MGF, NMS, RRI, and SEI over the mission. Note the variable log scales across the plots.

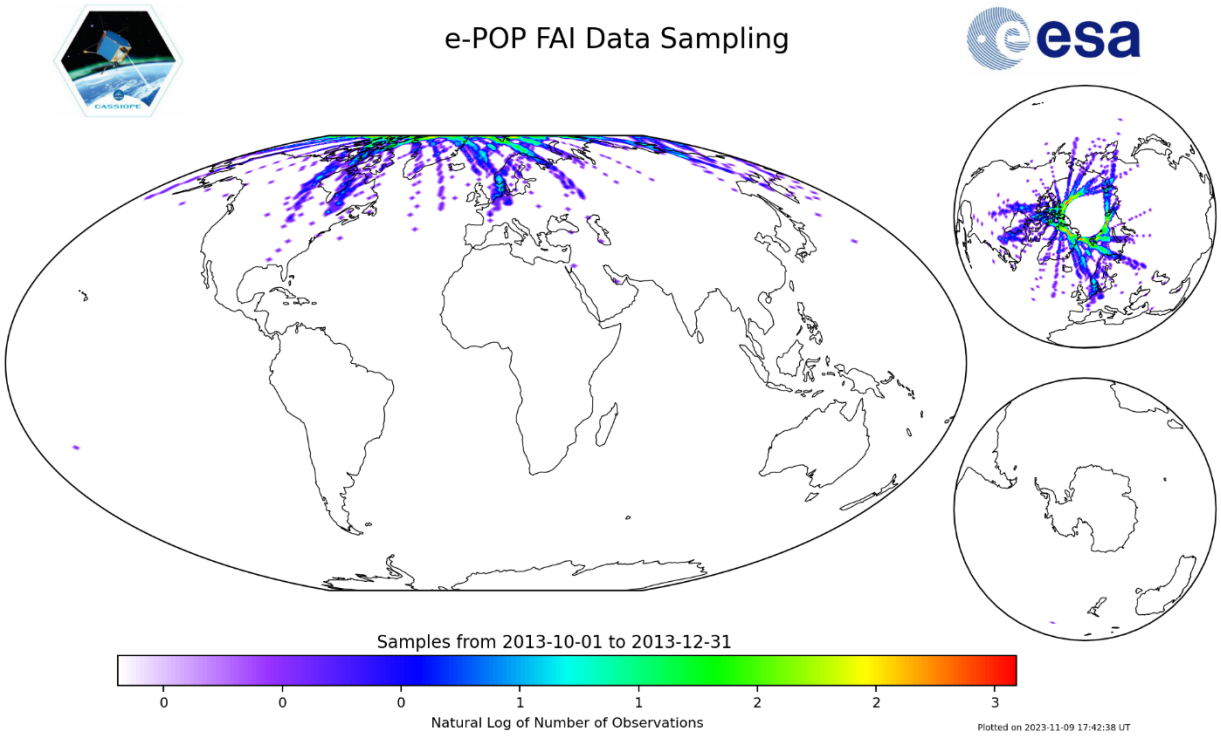

Figure 24: FAI Data Sampling for 2013

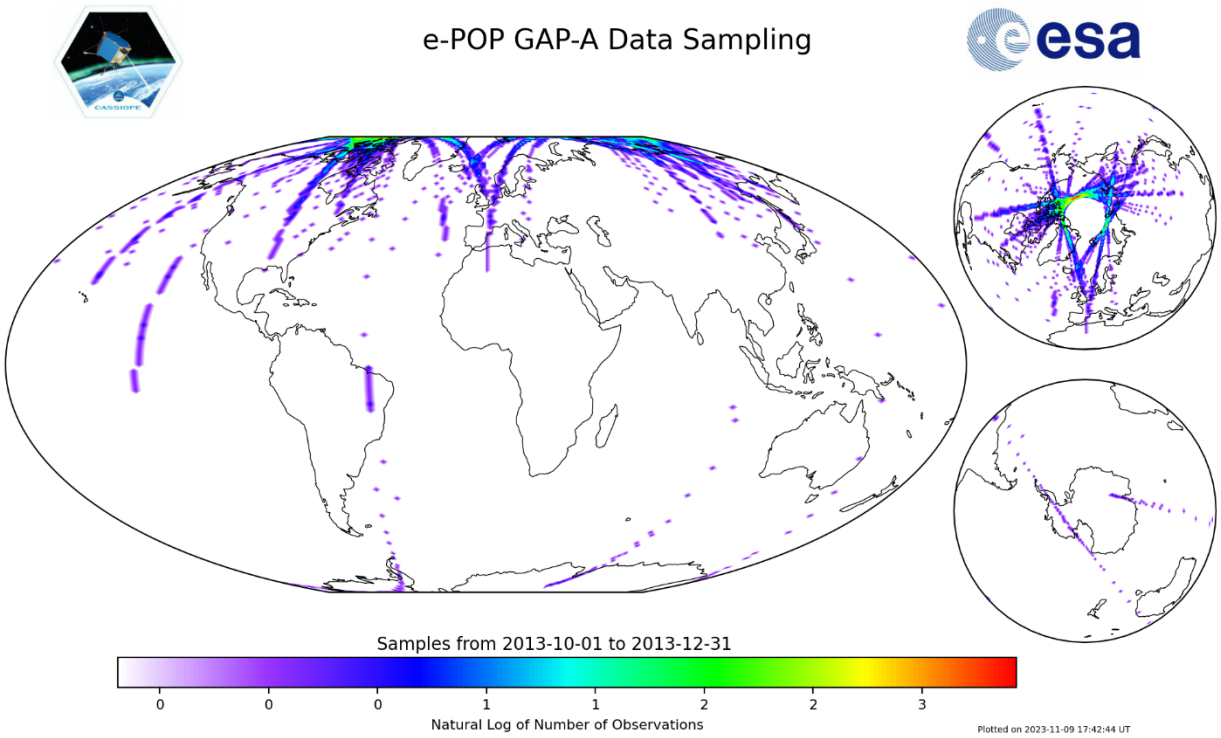

Figure 25: GAP-A Data Sampling for 2013

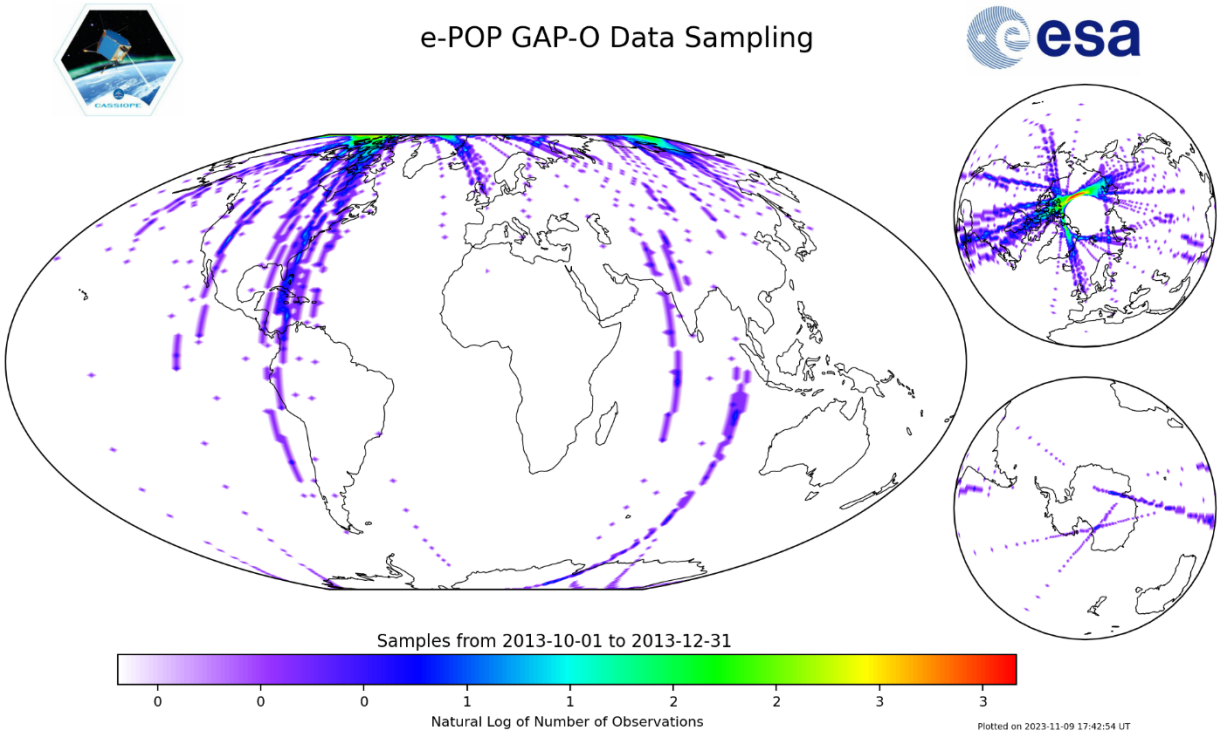

Figure 26: GAP-O Data Sampling for 2013

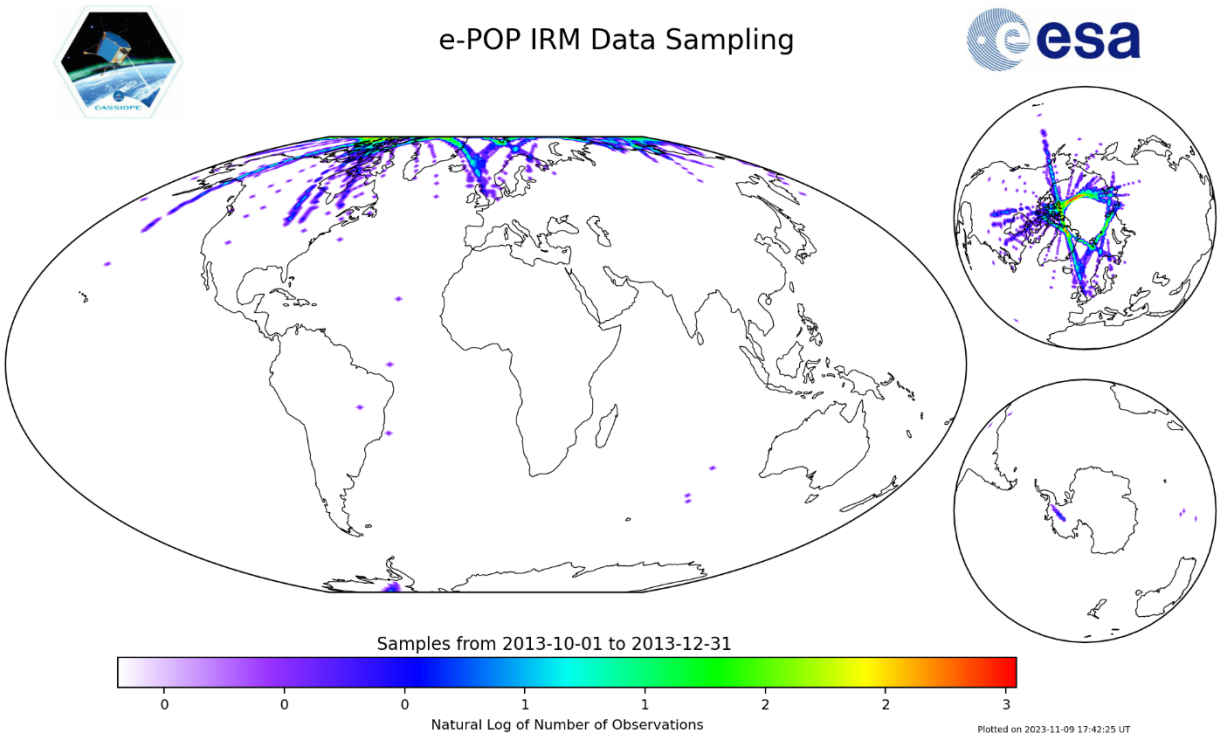

Figure 27: IRM Data Sampling for 2013

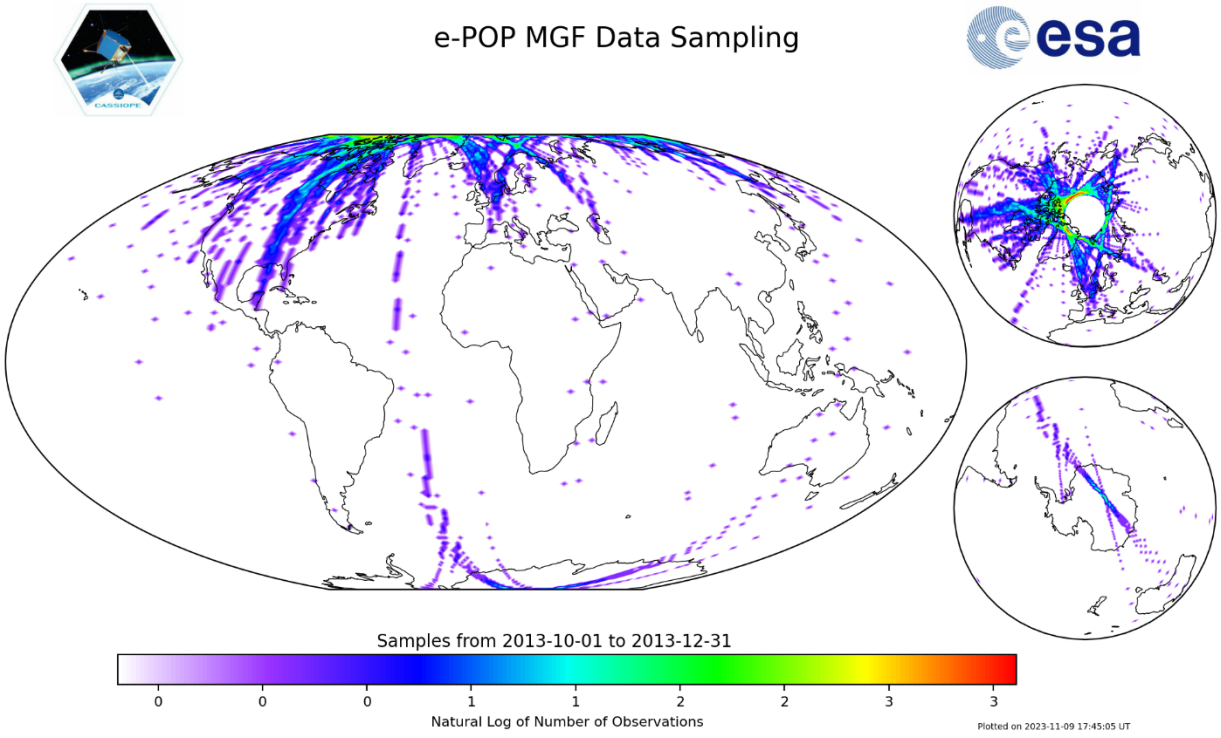

Figure 28: MGF Data Sampling for 2013

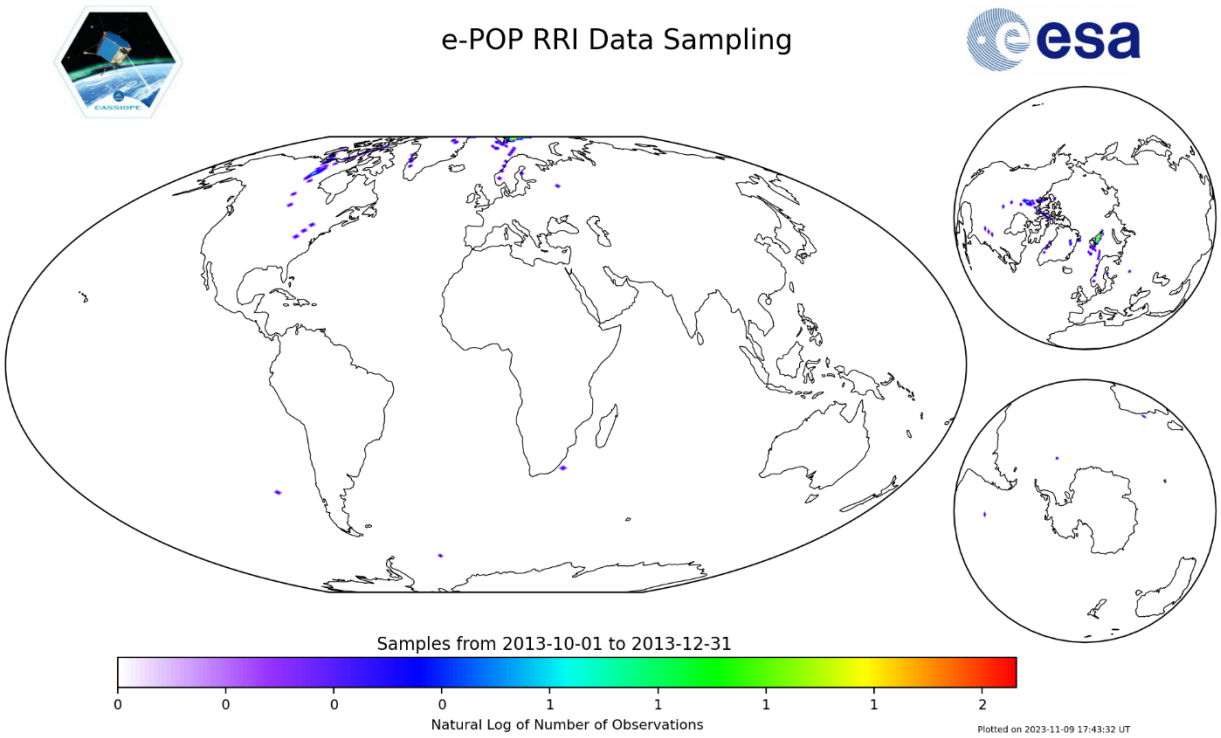

Figure 29: RRI Data Sampling for 2013

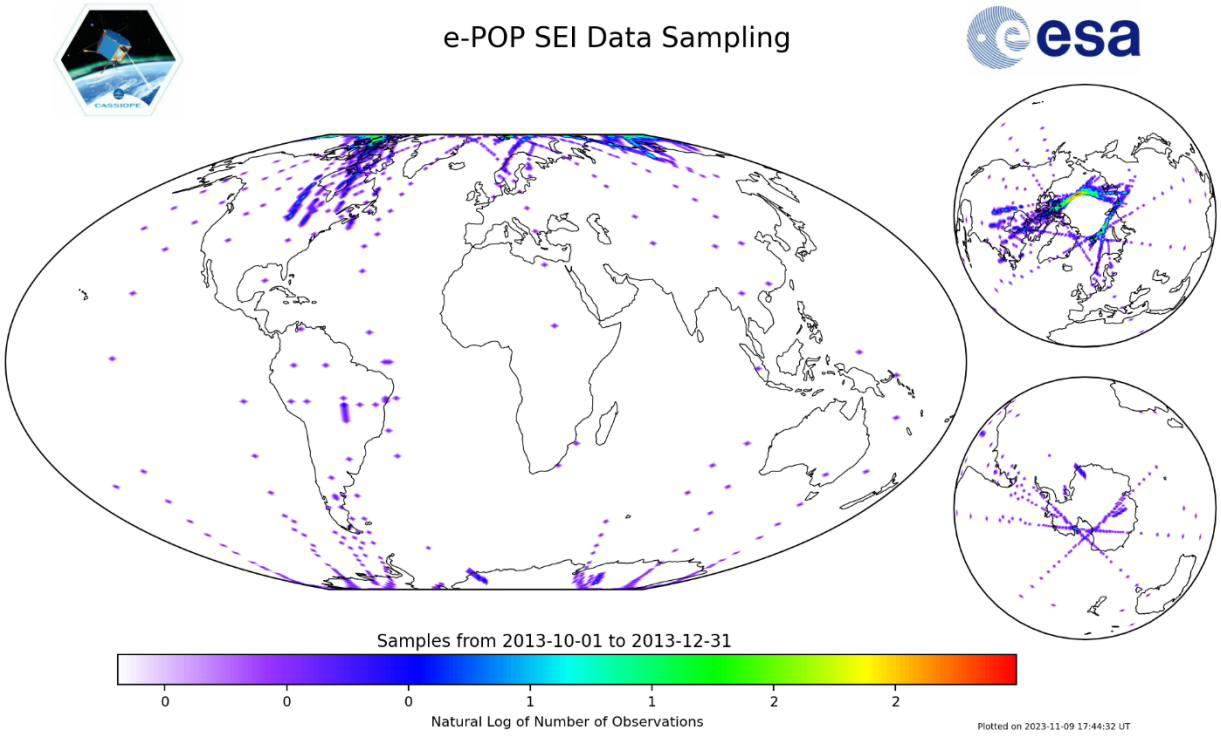

Figure 30: SEI Data Sampling for 2013

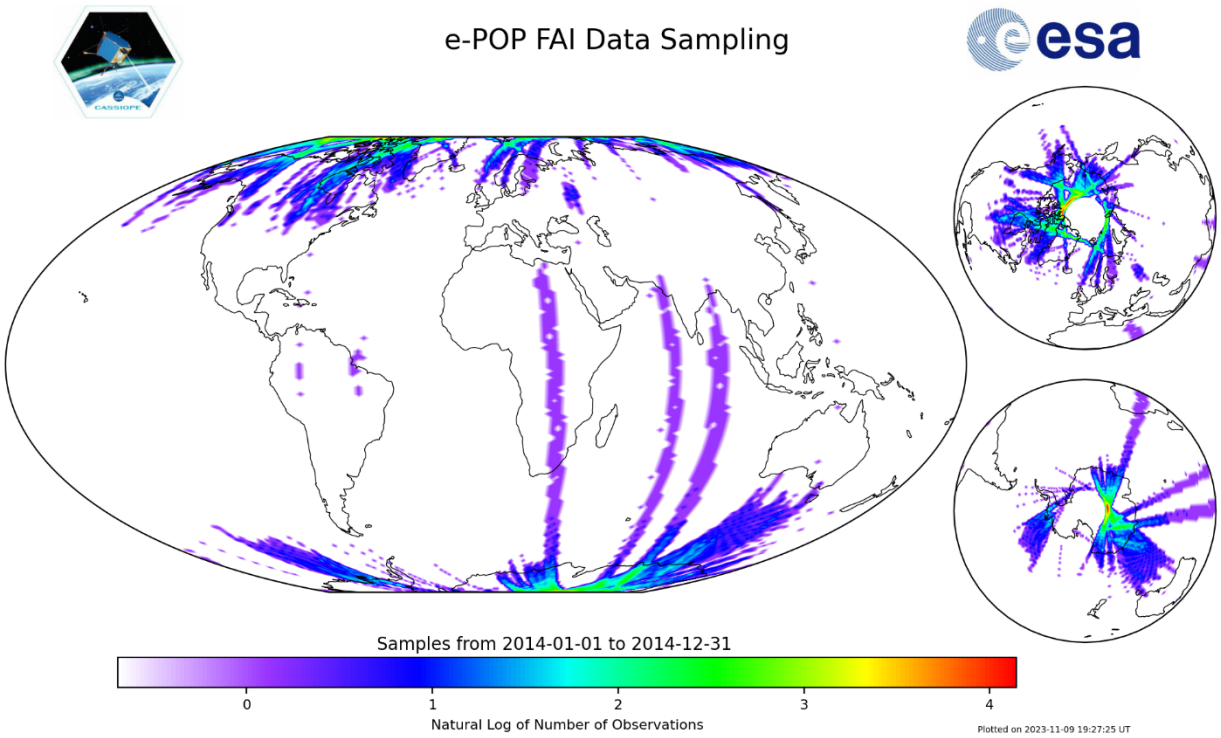

Figure 31: FAI Data Sampling for 2014

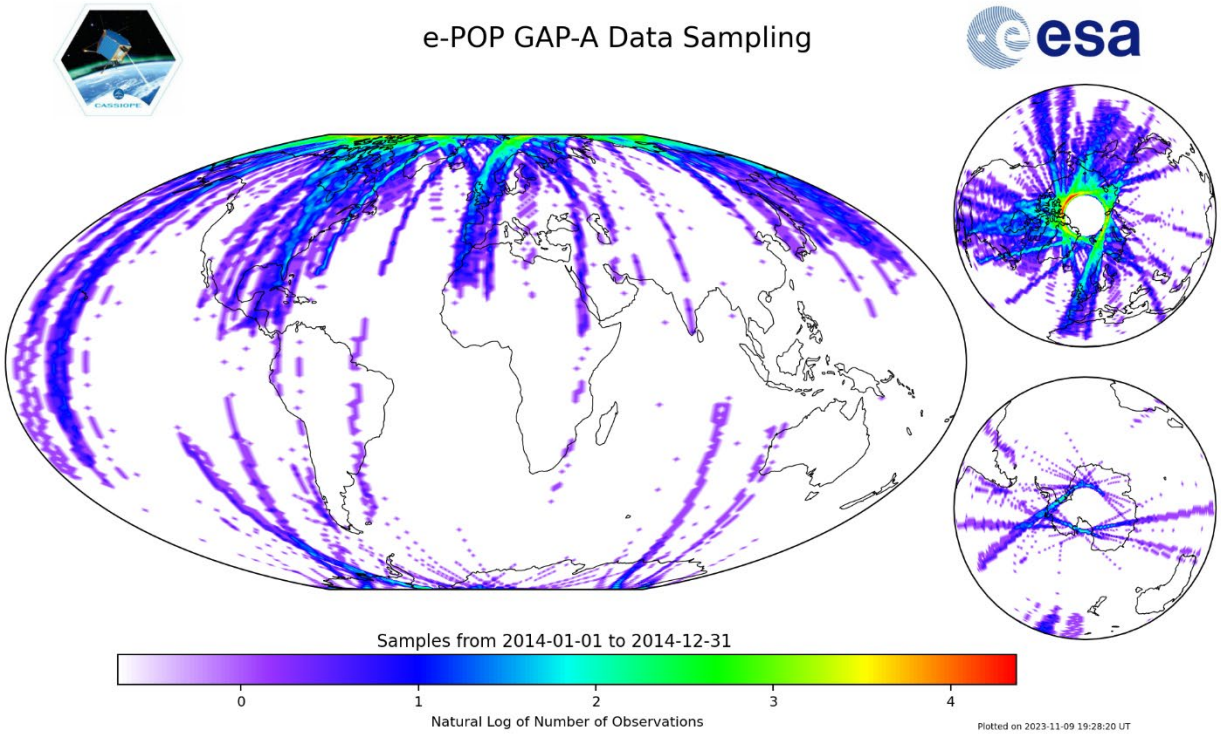

Figure 32: GAP-A Data Sampling for 2014

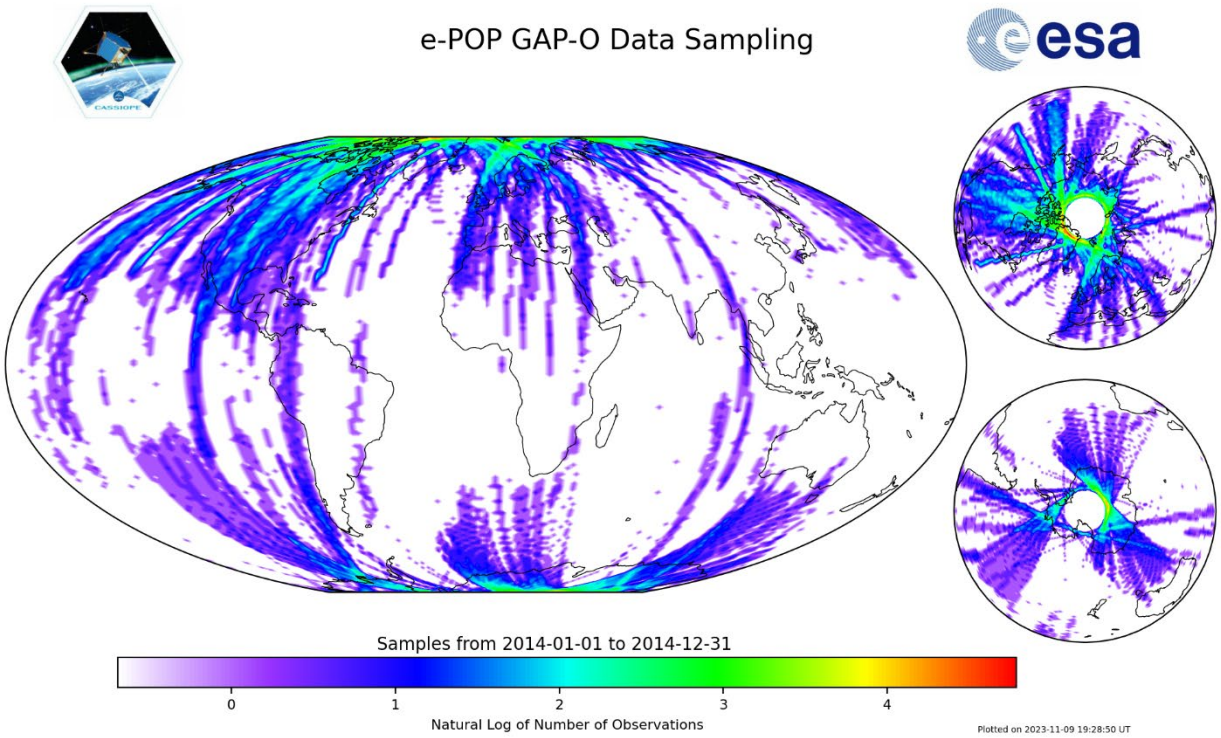

Figure 33: GAP-O Data Sampling for 2014

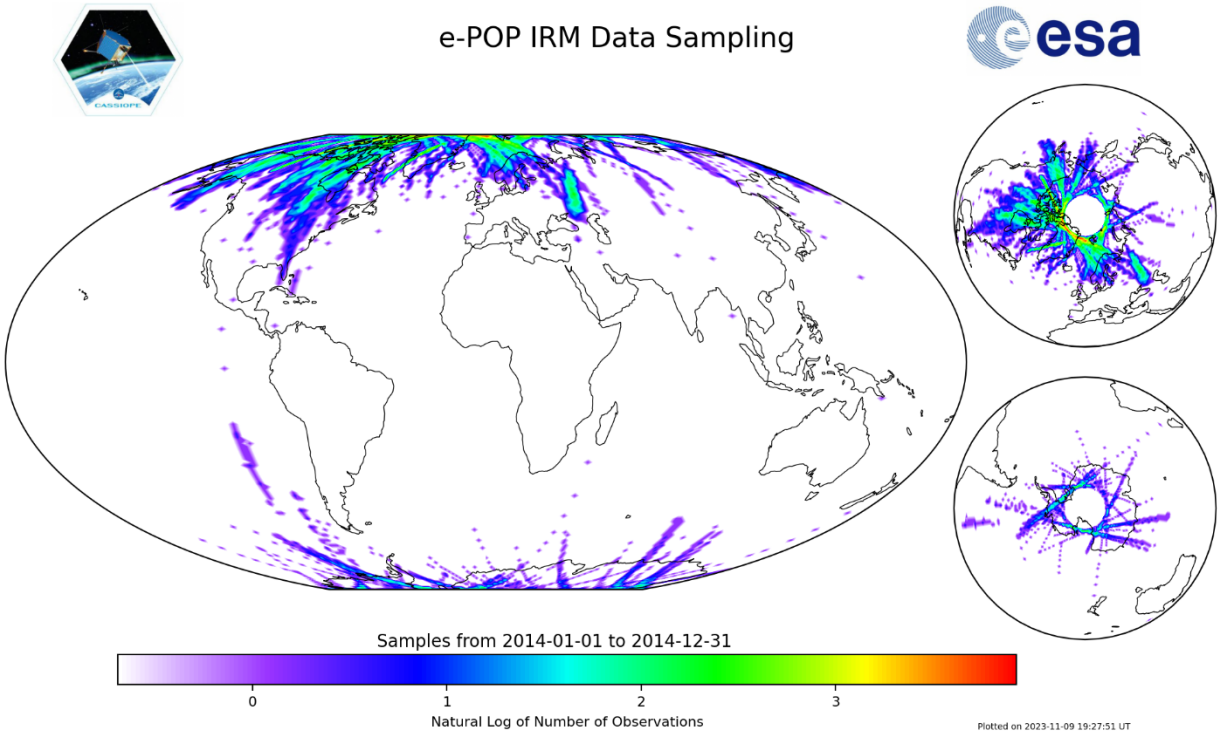

Figure 34: IRM Data Sampling for 2014

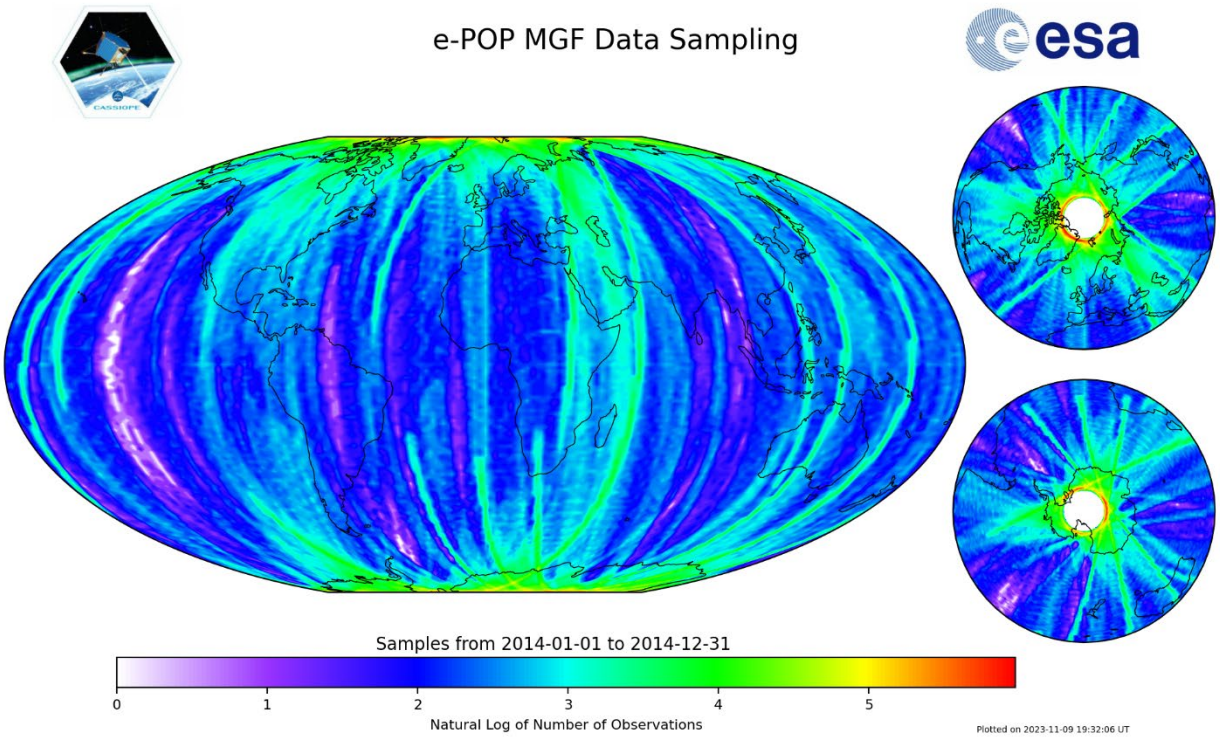

Figure 35: MGF Data Sampling for 2014

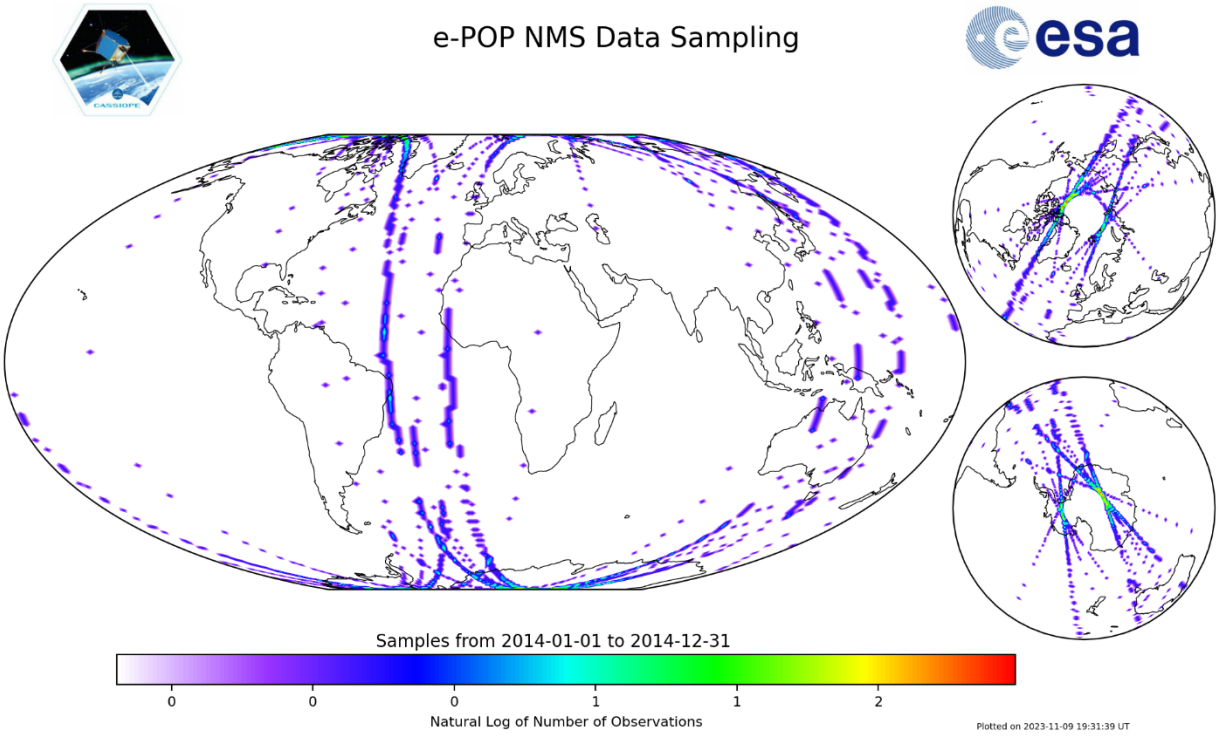

Figure 36: NMS Data Sampling for 2014

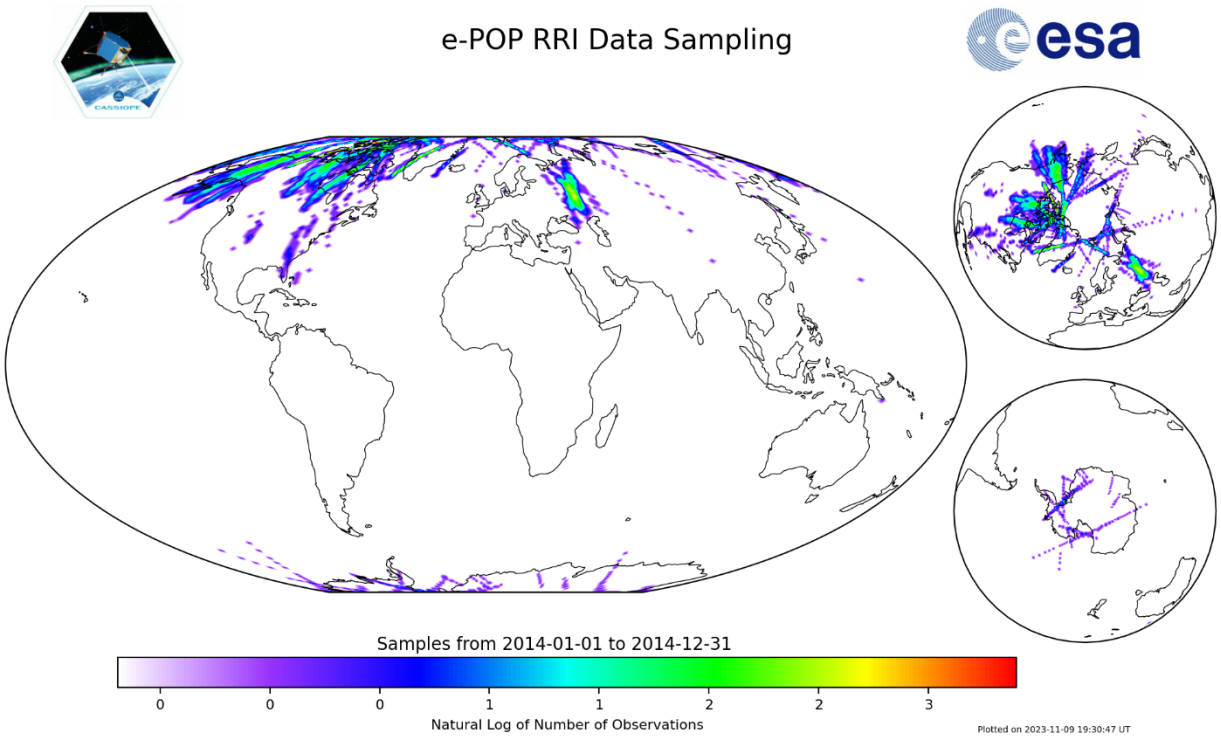

Figure 37: RRI Data Sampling for 2014

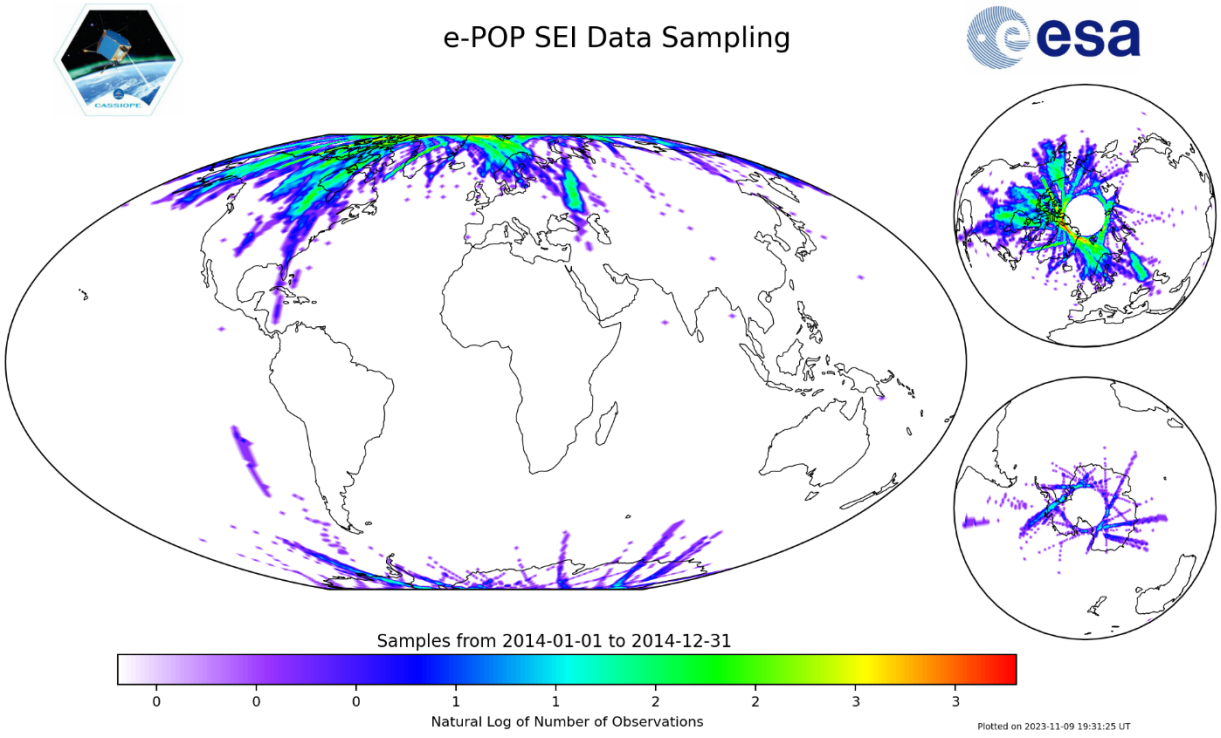

Figure 38: SEI Data Sampling for 2014

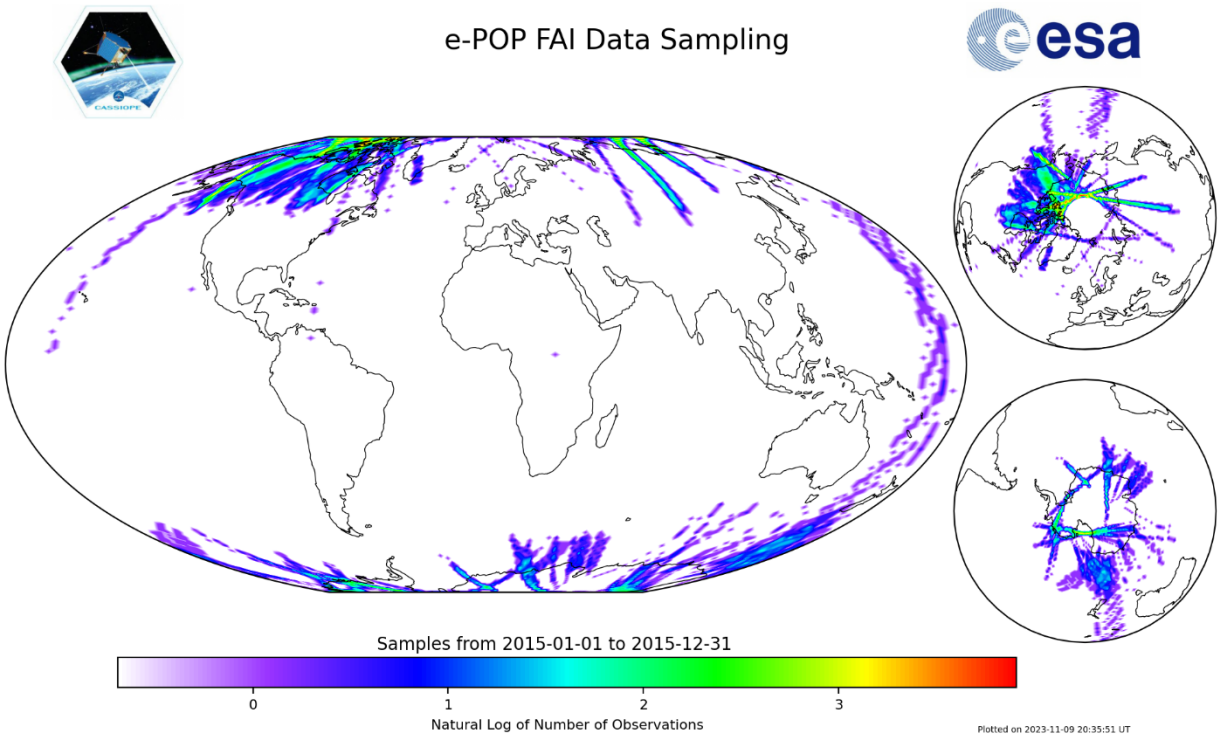

Figure 39: FAI Data Sampling for 2015

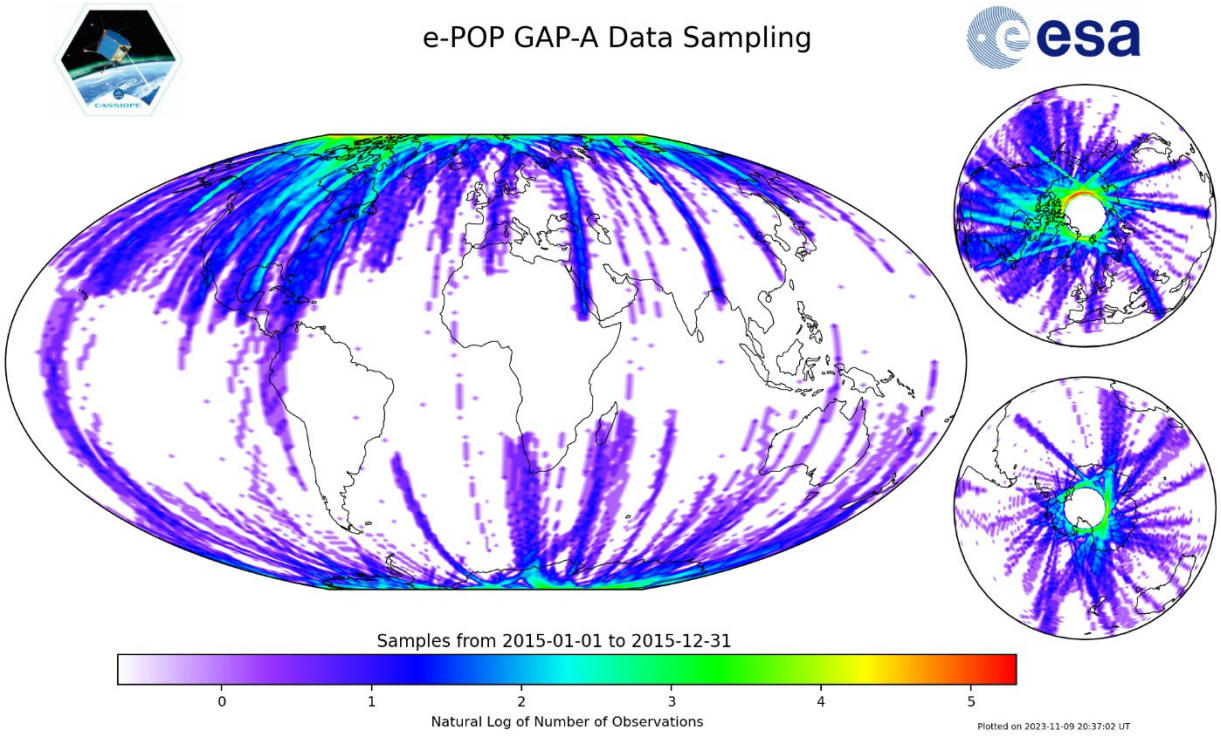

Figure 40: GAP-A Data Sampling for 2015

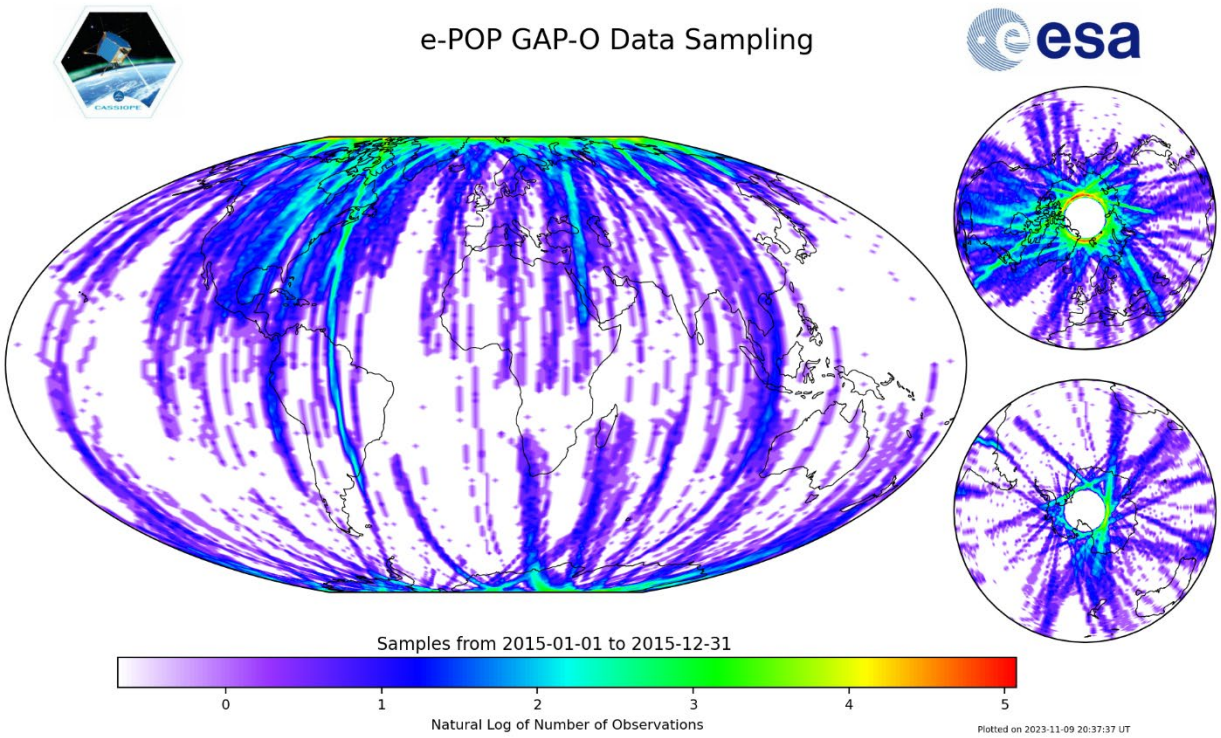

Figure 41: GAP-O Data Sampling for 2015

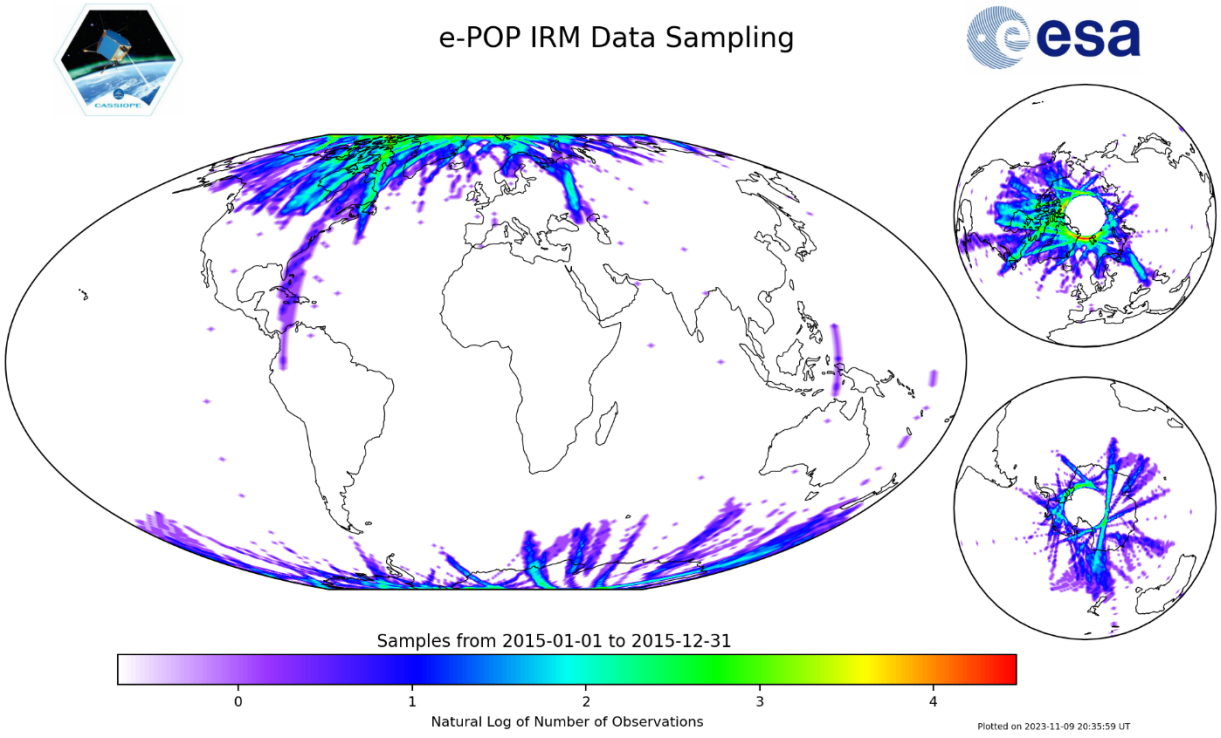

Figure 42: IRM Data Sampling for 2015

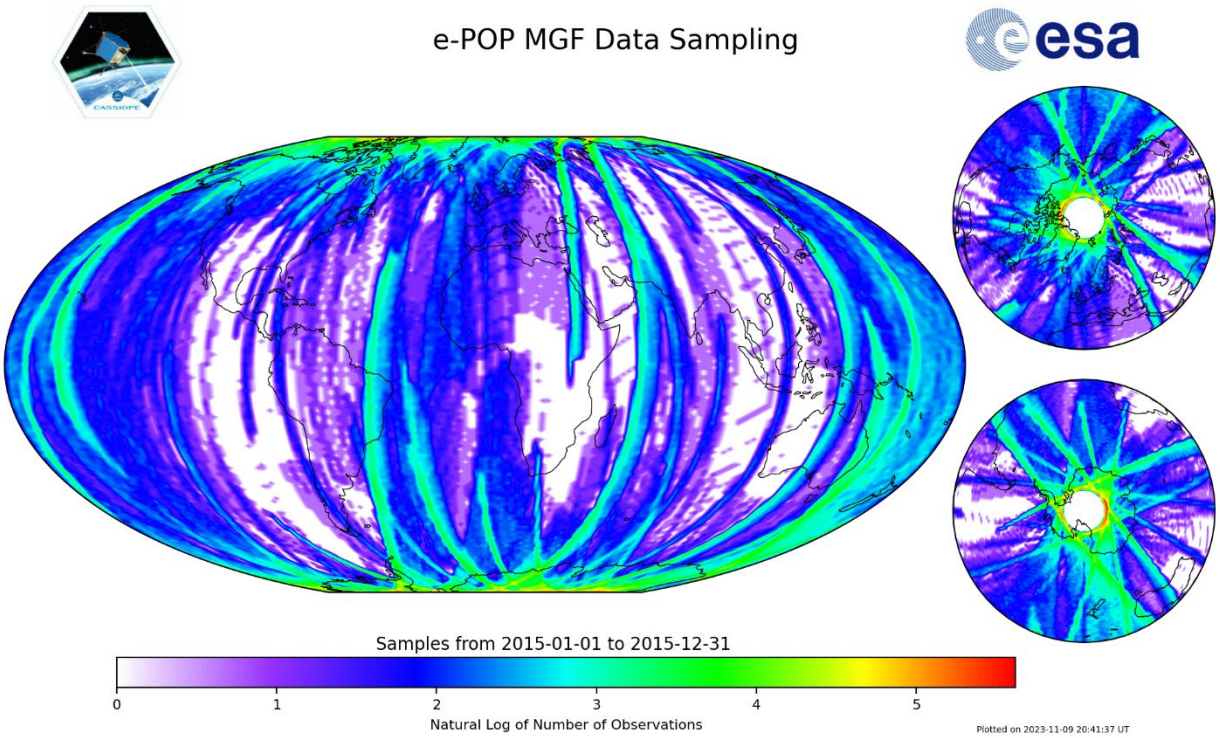

Figure 43: MGF Data Sampling for 2015

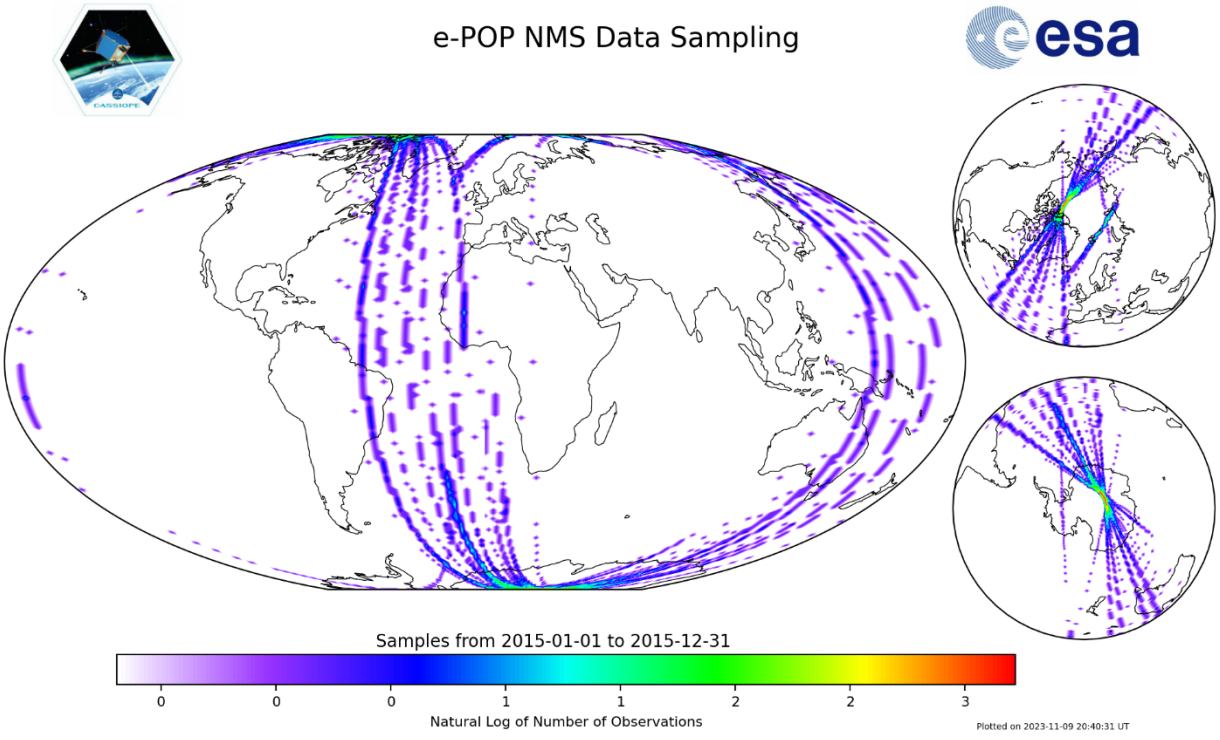

Figure 44: NMS Data Sampling for 2015

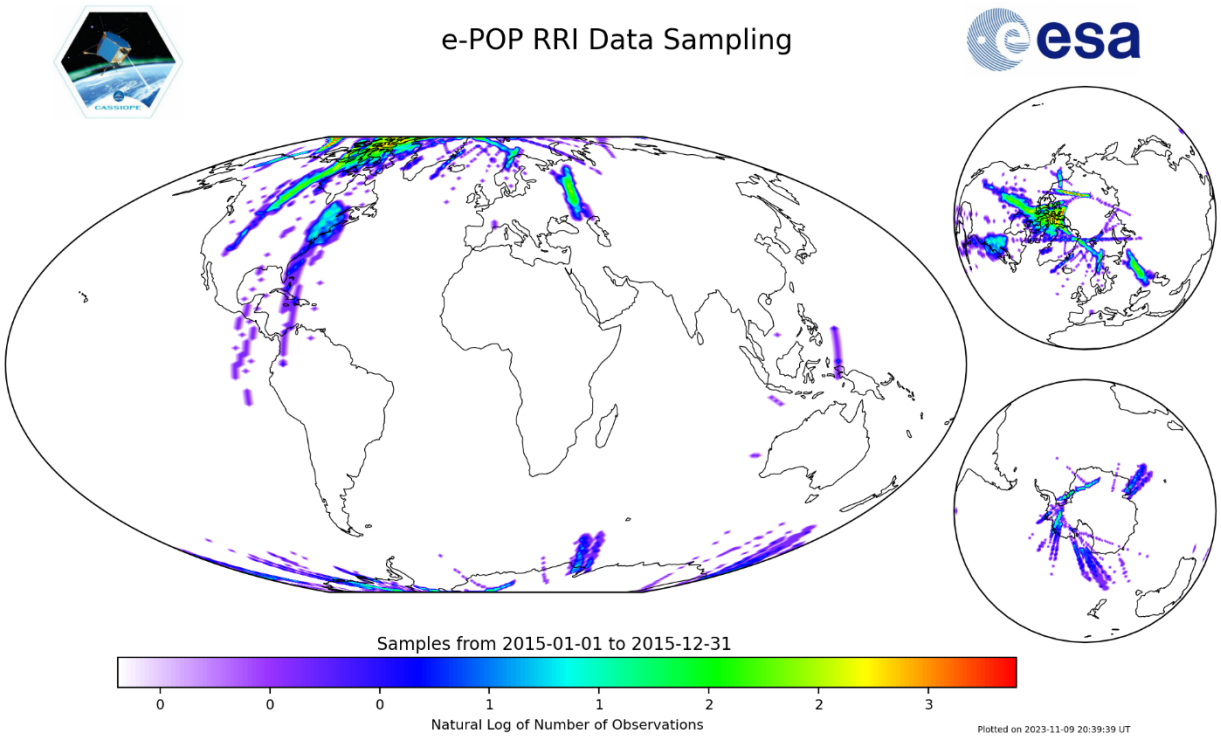

Figure 45: RRI Data Sampling for 2015

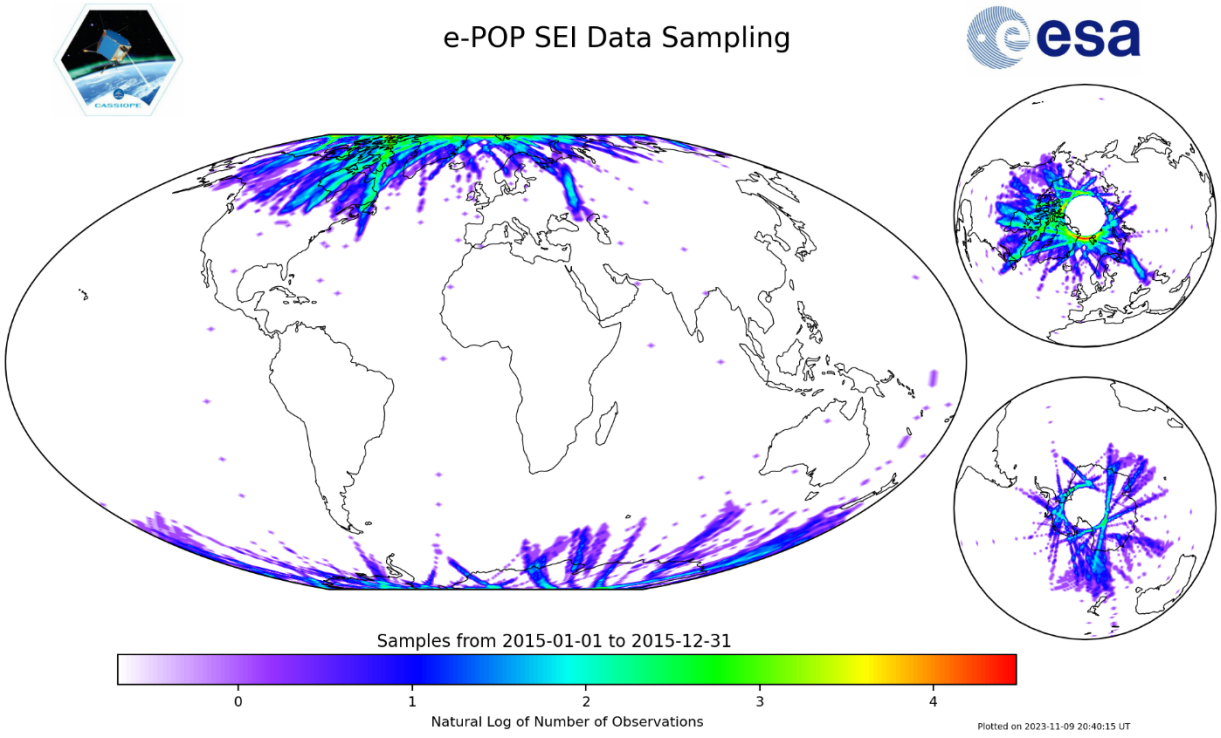

Figure 46: SEI Data Sampling for 2015

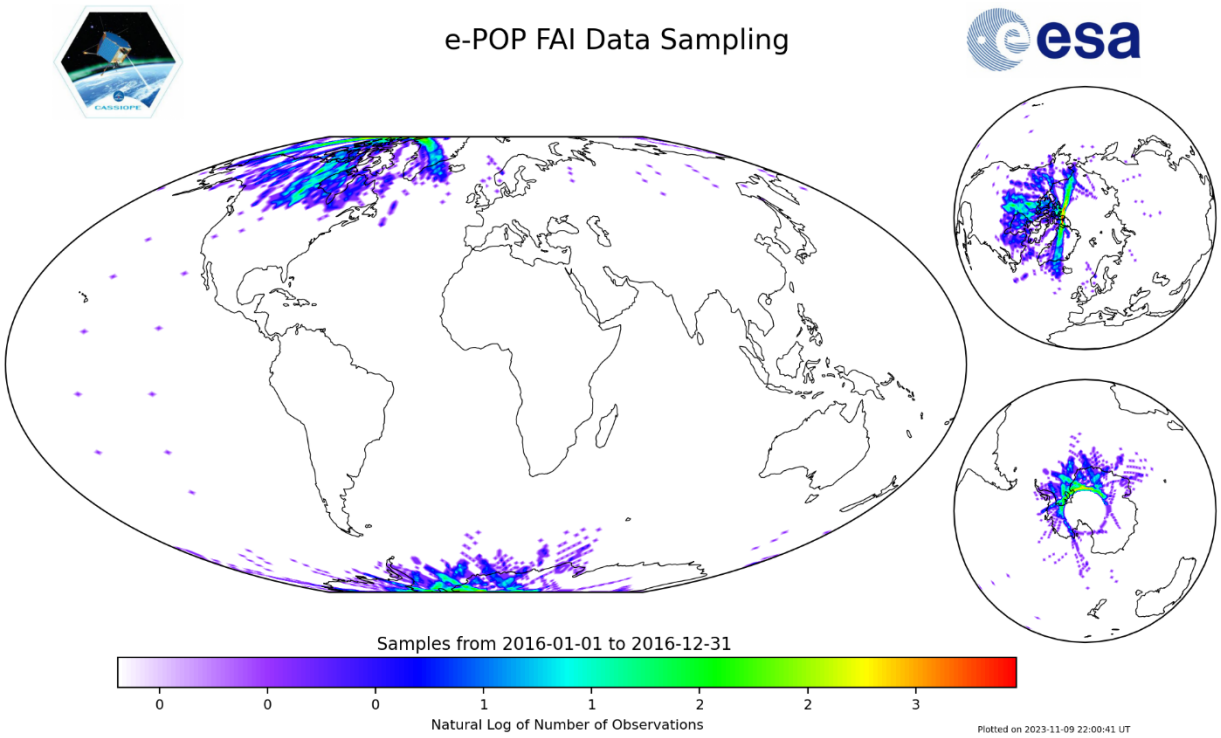

Figure 47: FAI Data Sampling for 2016

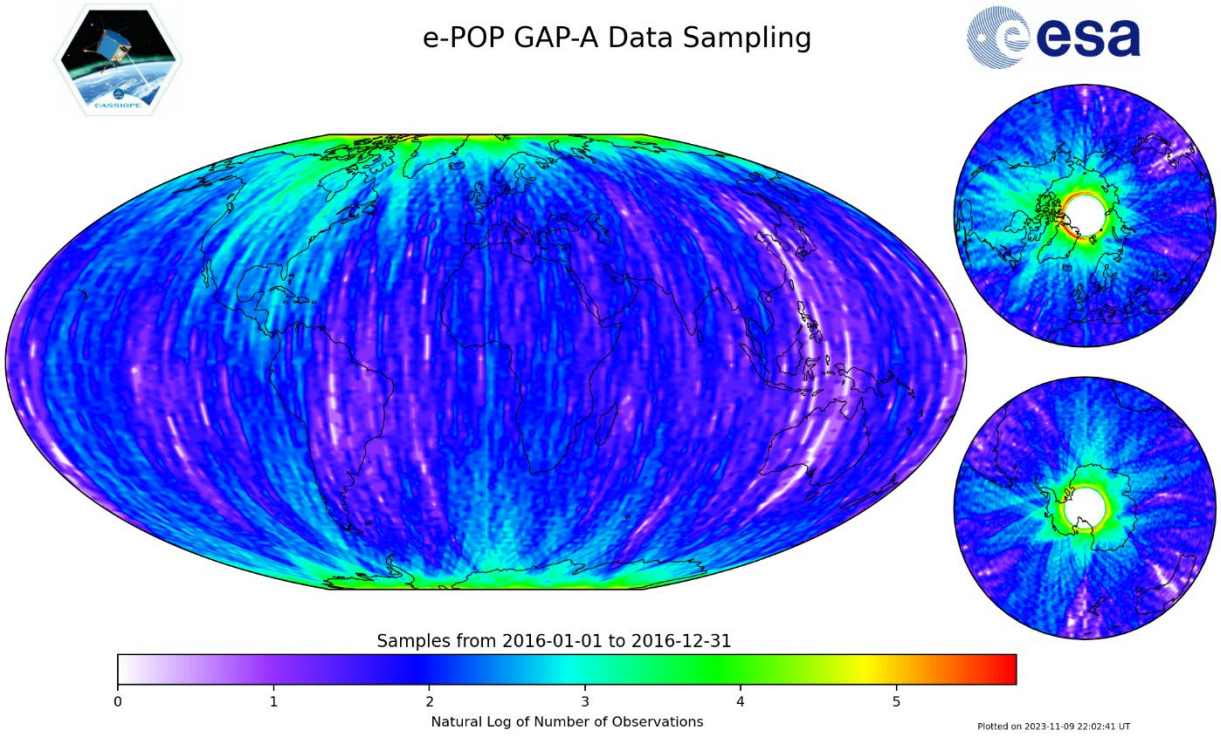

Figure 48: GAP-A Data Sampling for 2016

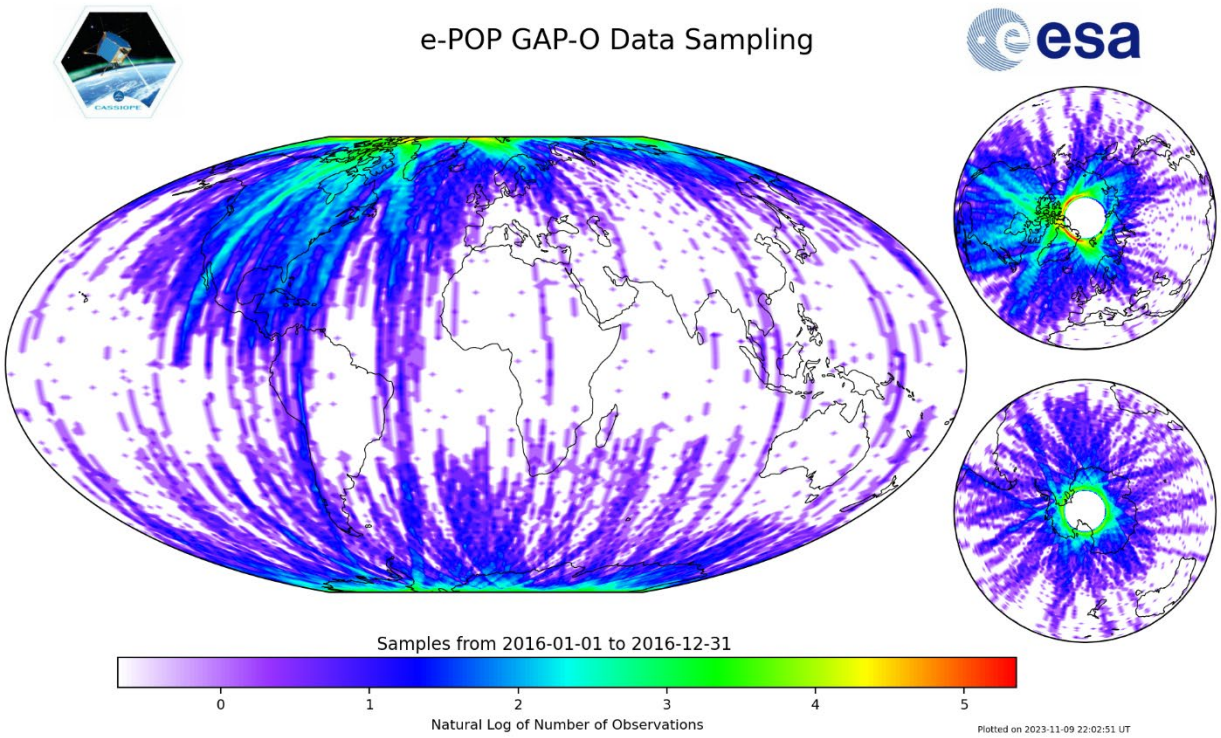

Figure 49: GAP-O Data Sampling for 2016

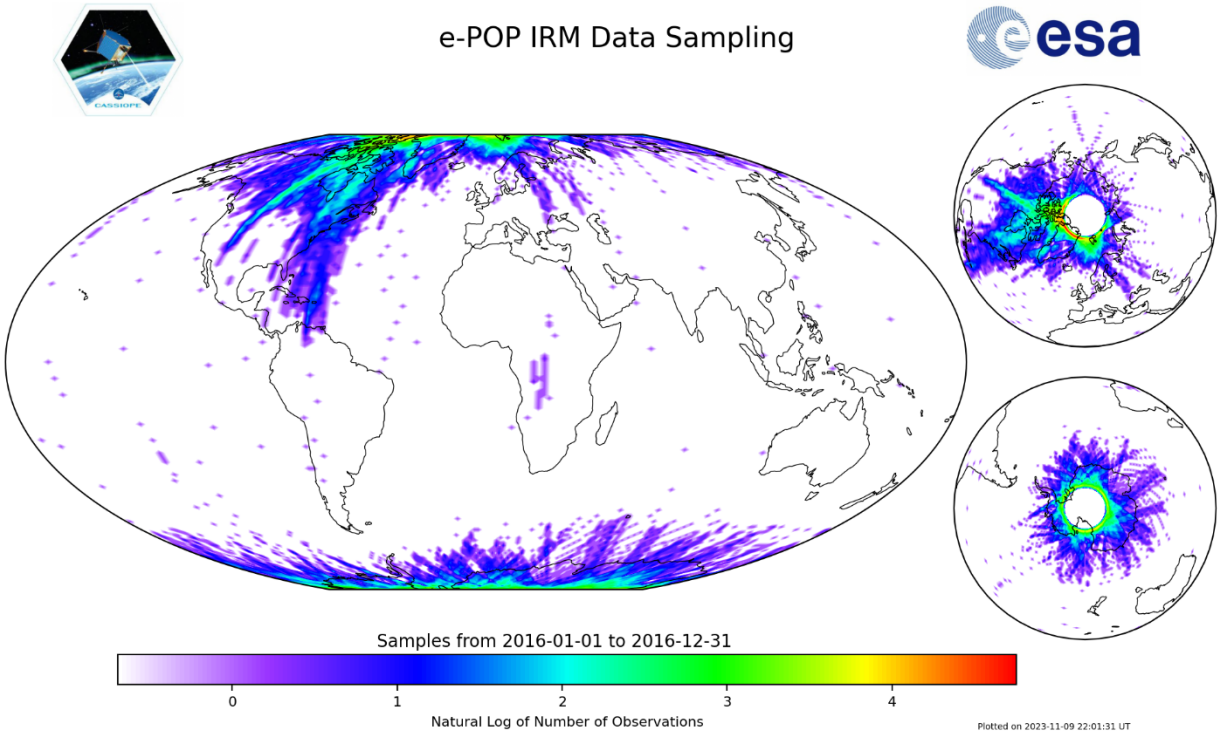

Figure 50: IRM Data Sampling for 2016

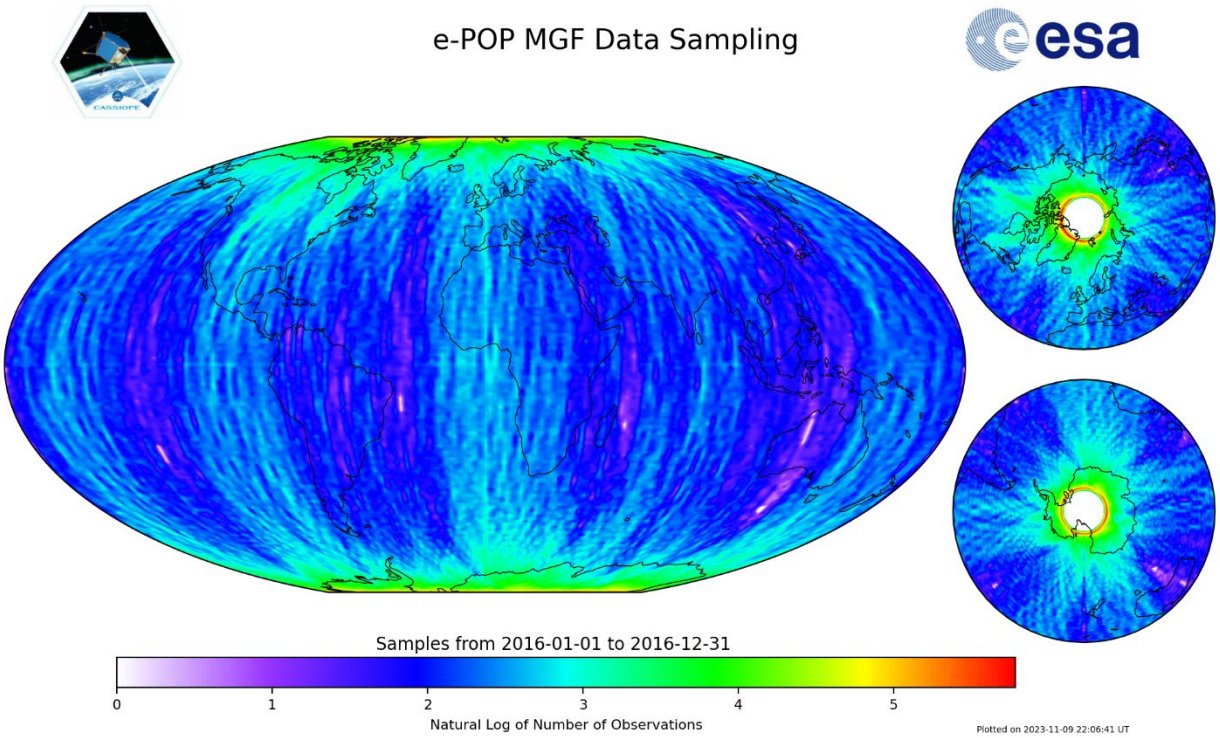

Figure 51: MGF Data Sampling for 2016

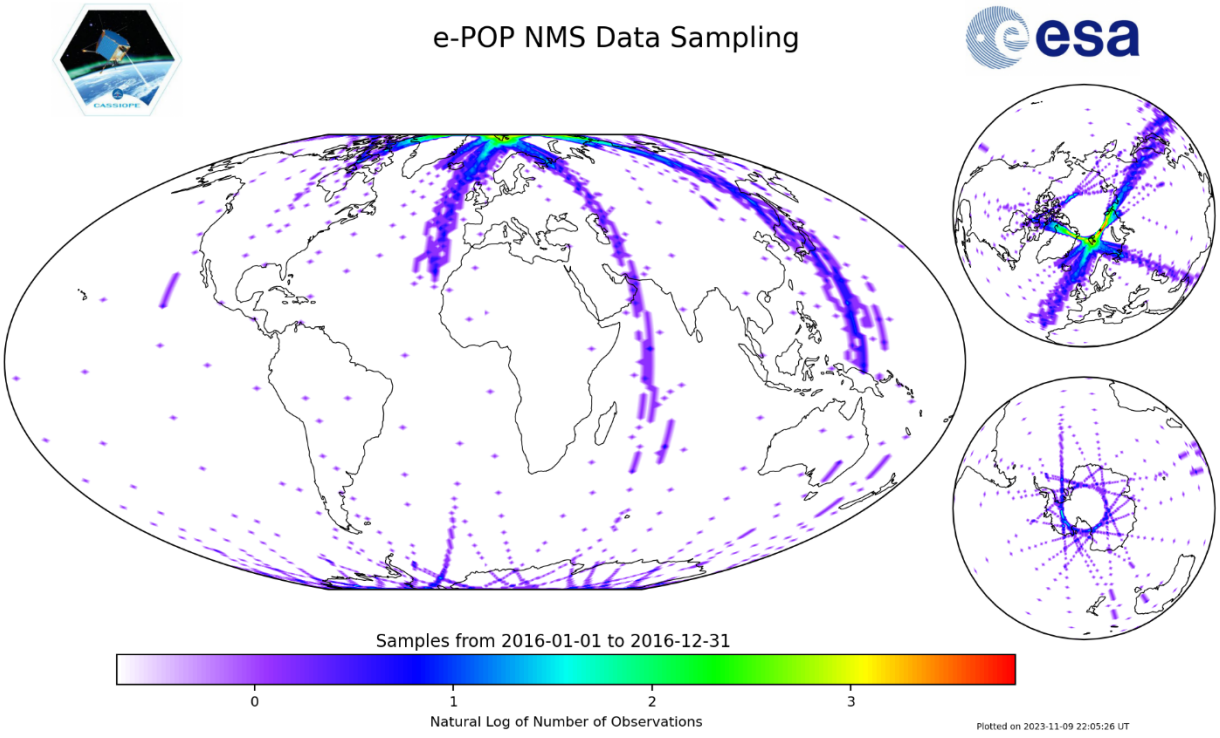

Figure 52: NMS Data Sampling for 2016

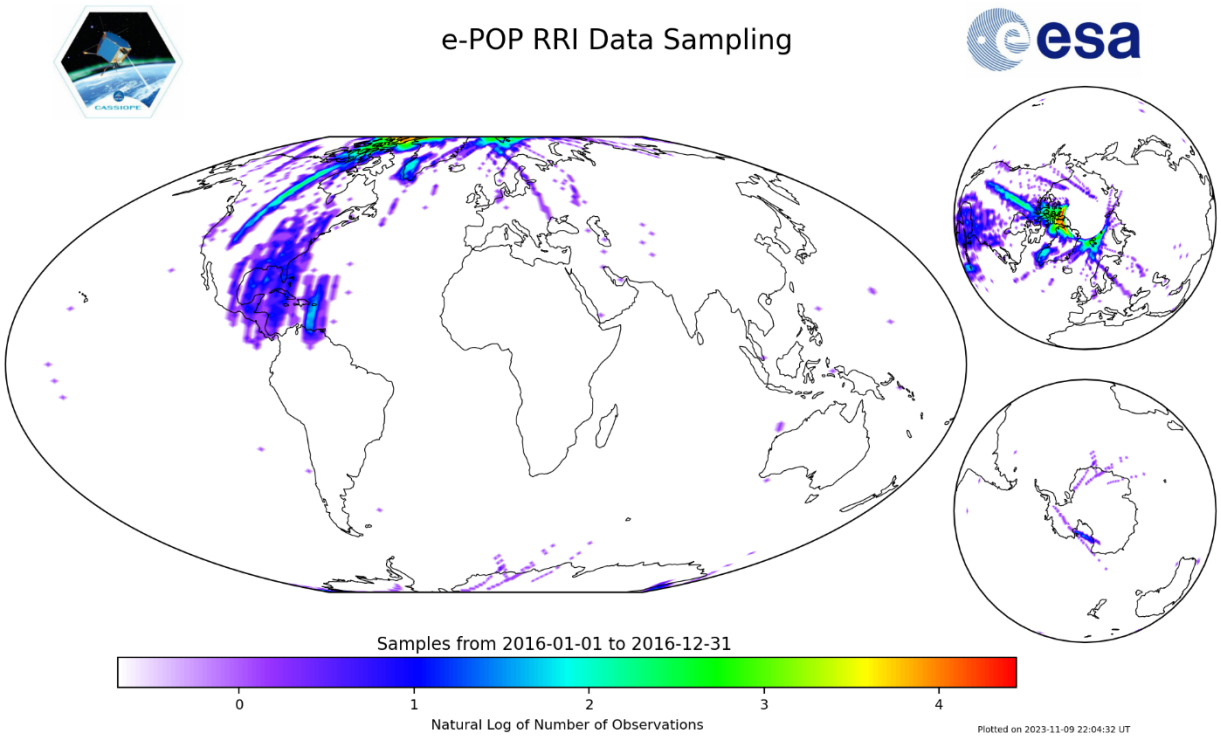

Figure 53: RRI Data Sampling for 2016

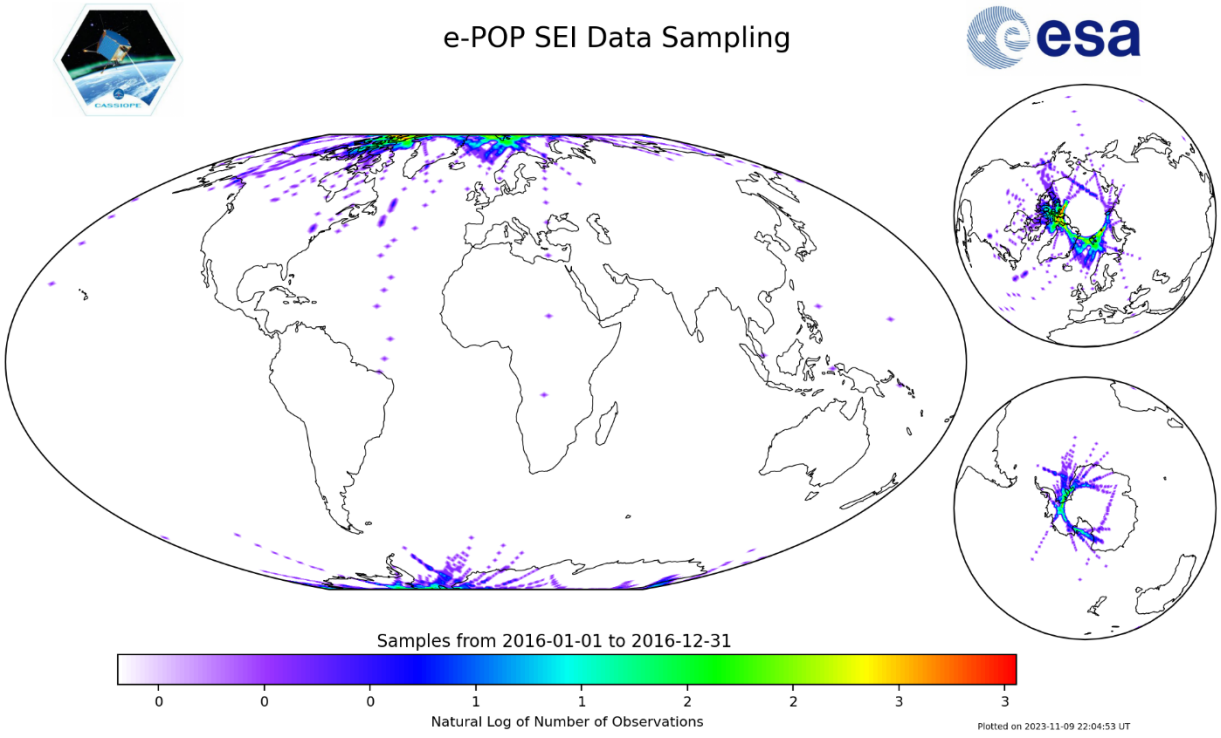

Figure 54: SEI Data Sampling for 2016

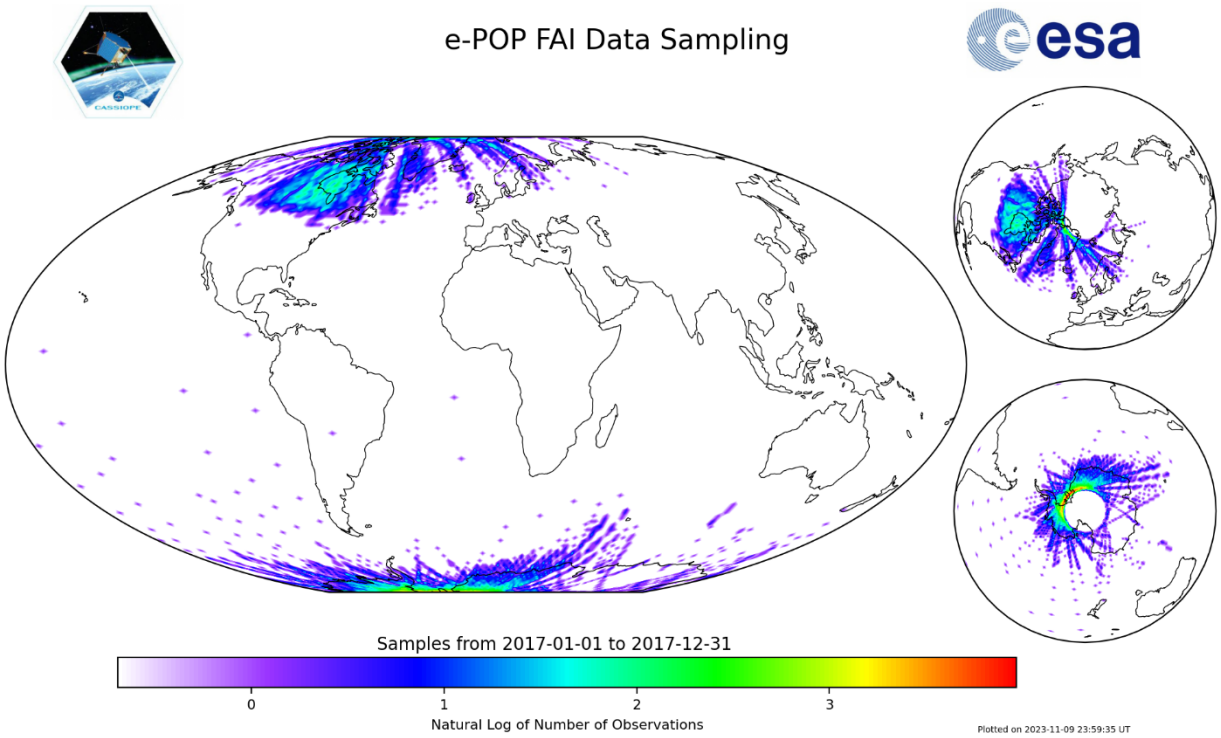

Figure 55: FAI Data Sampling for 2017

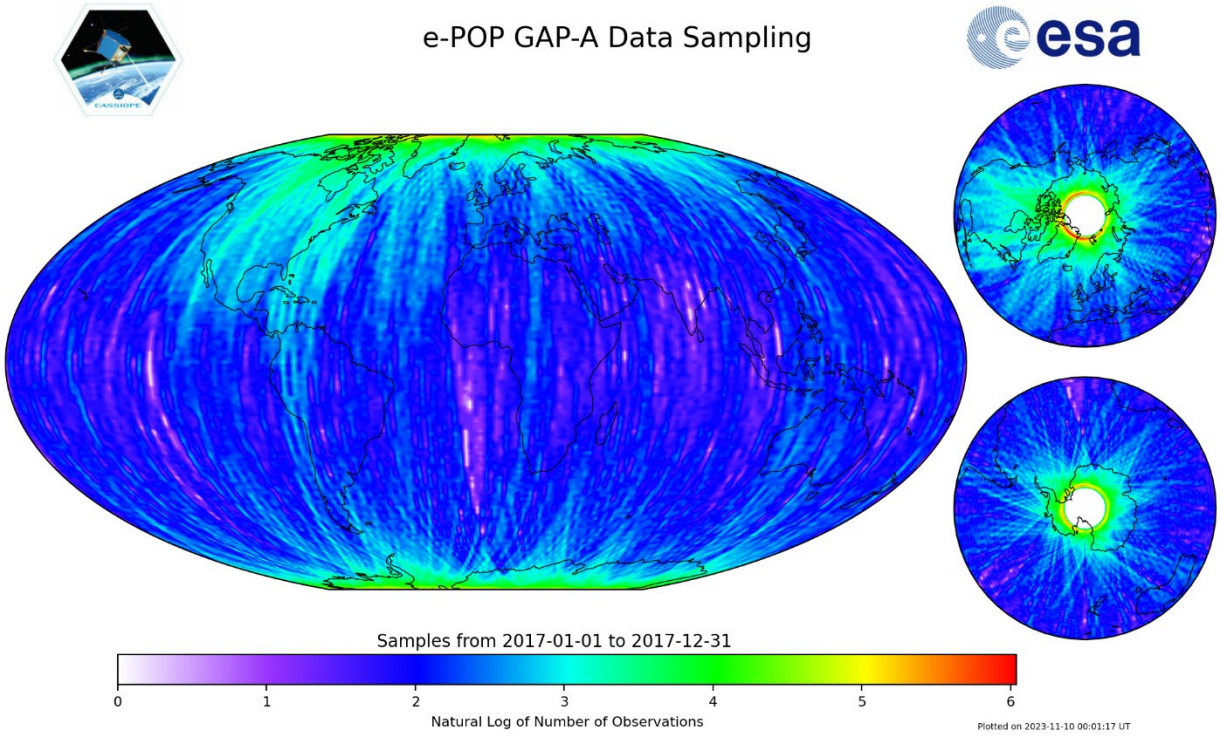

Figure 56: GAP-A Data Sampling for 2017

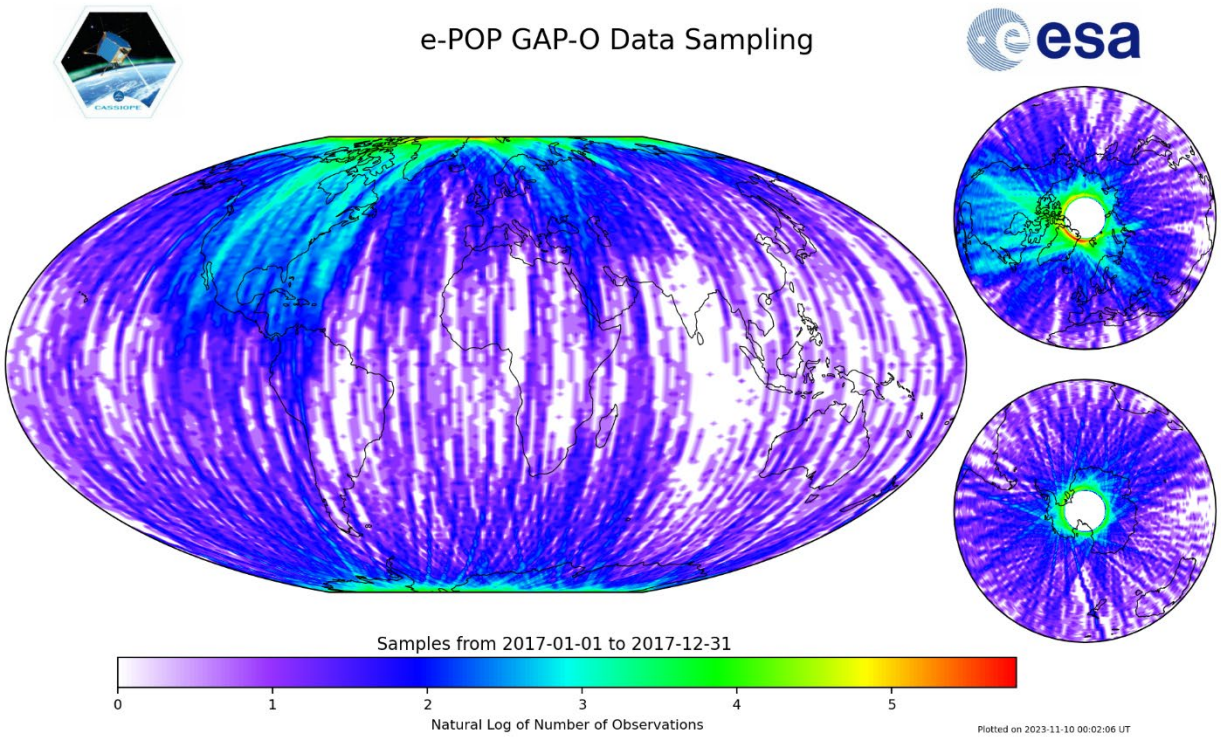

Figure 57: GAP-O Data Sampling for 2017

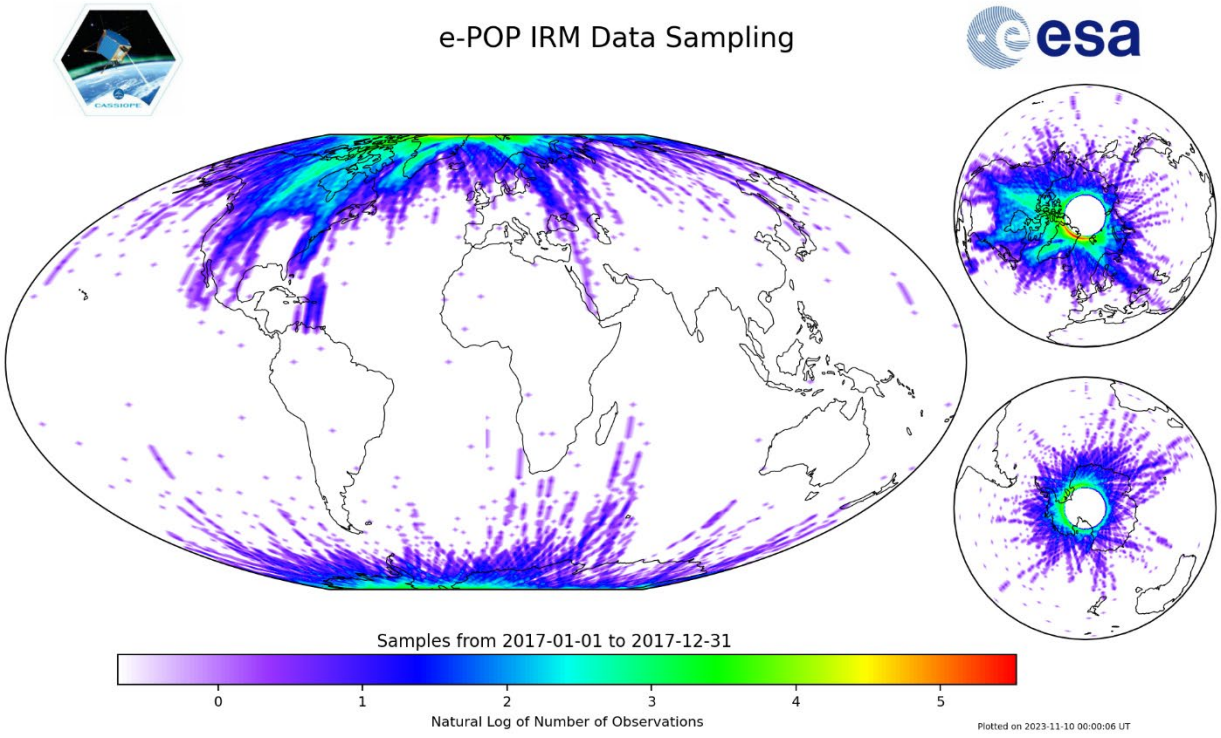

Figure 58: IRM Data Sampling for 2017

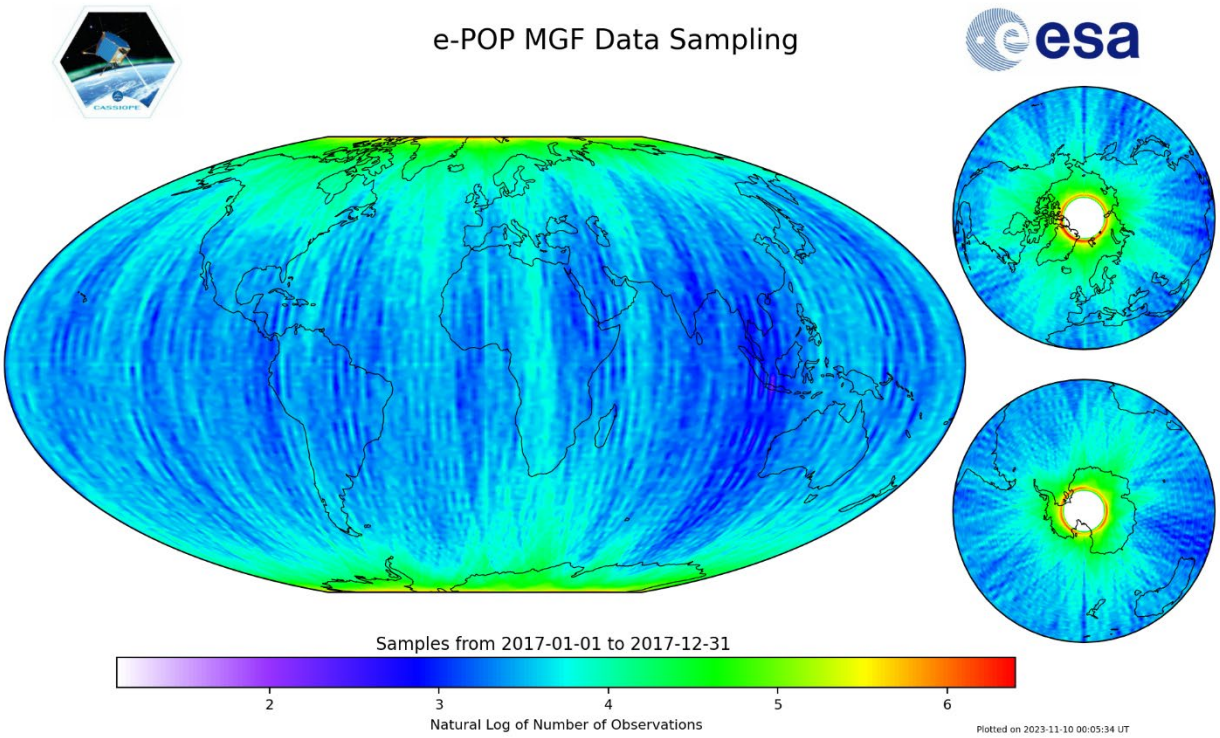

Figure 59: MGF Data Sampling for 2017

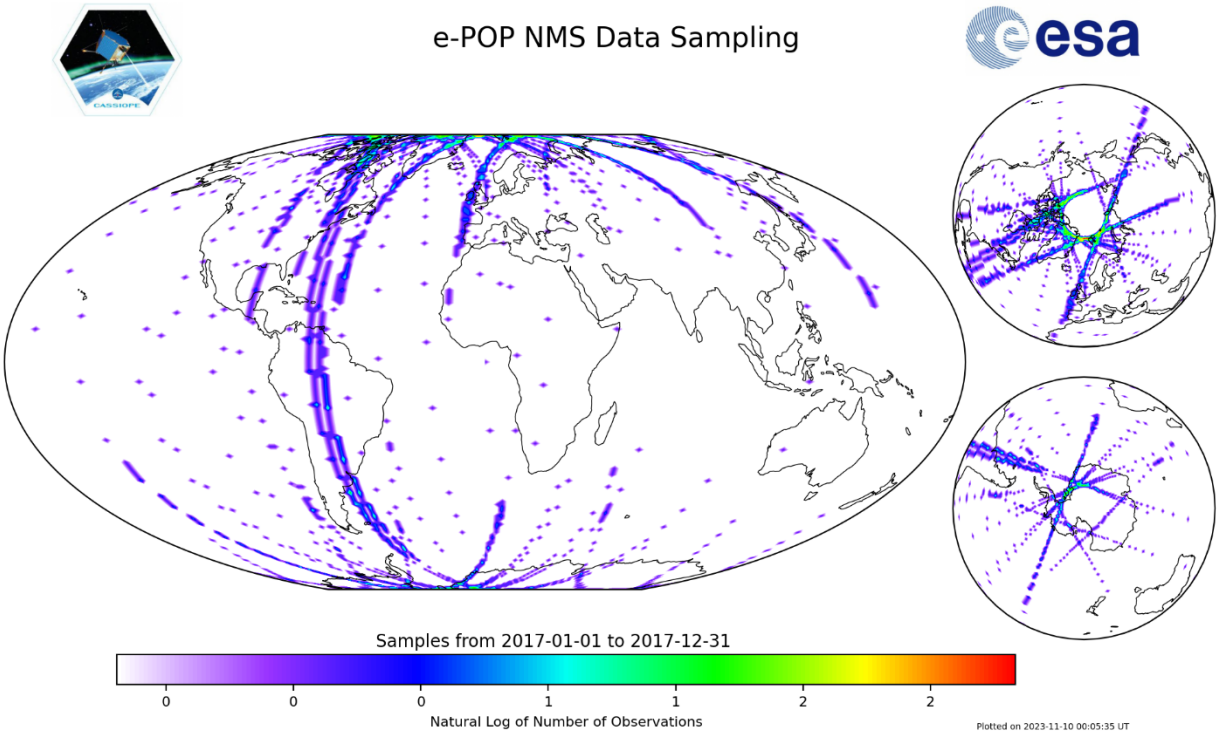

Figure 60: NMS Data Sampling for 2017

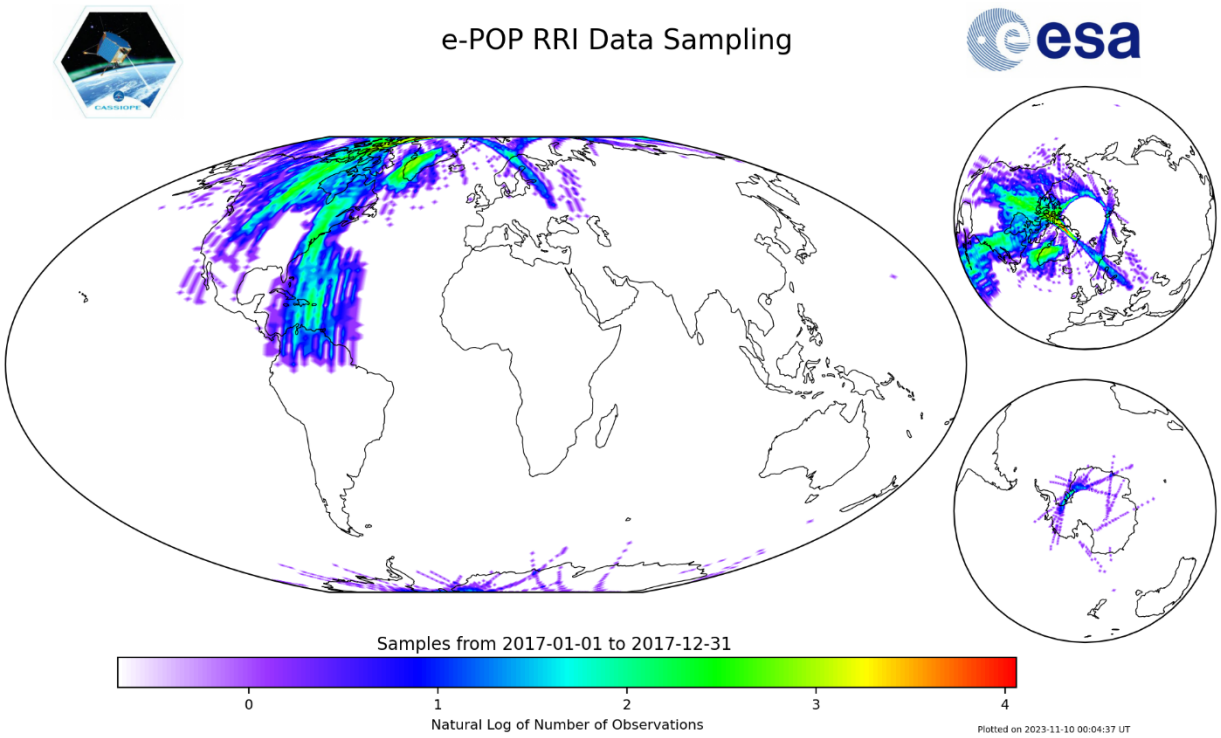

Figure 61: RRI Data Sampling for 2017

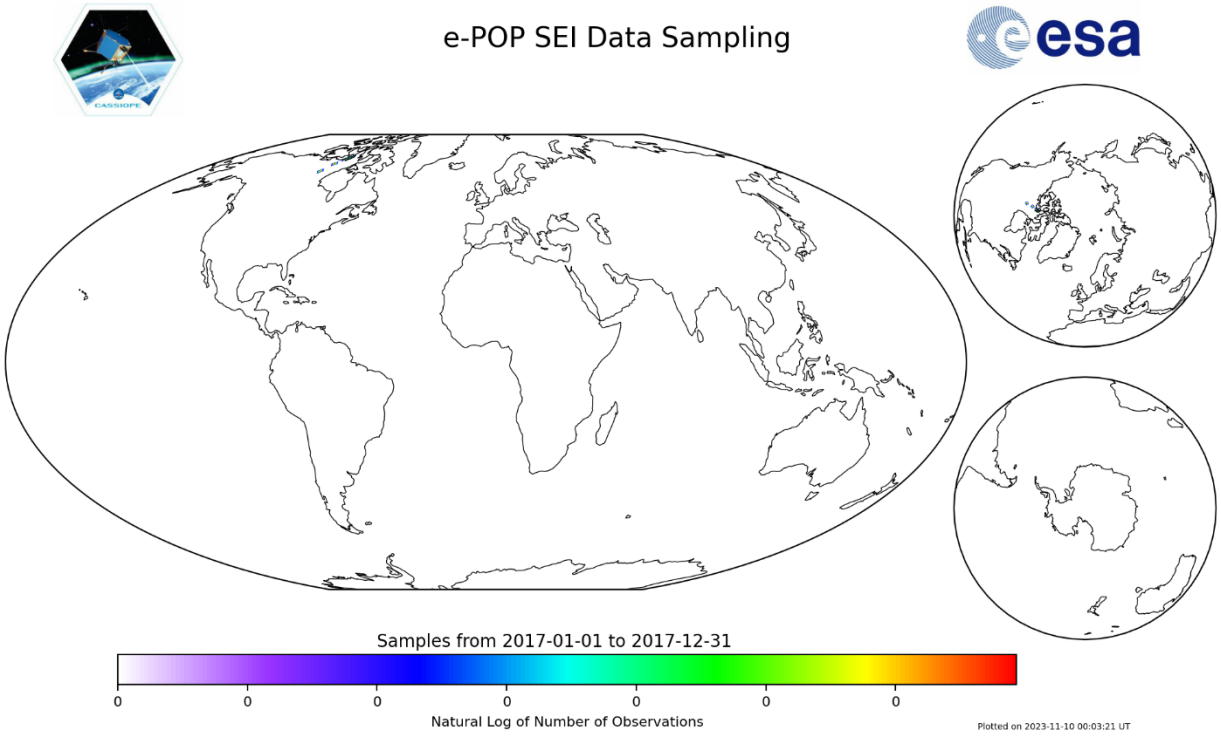

Figure 62: SEI Data Sampling for 2017

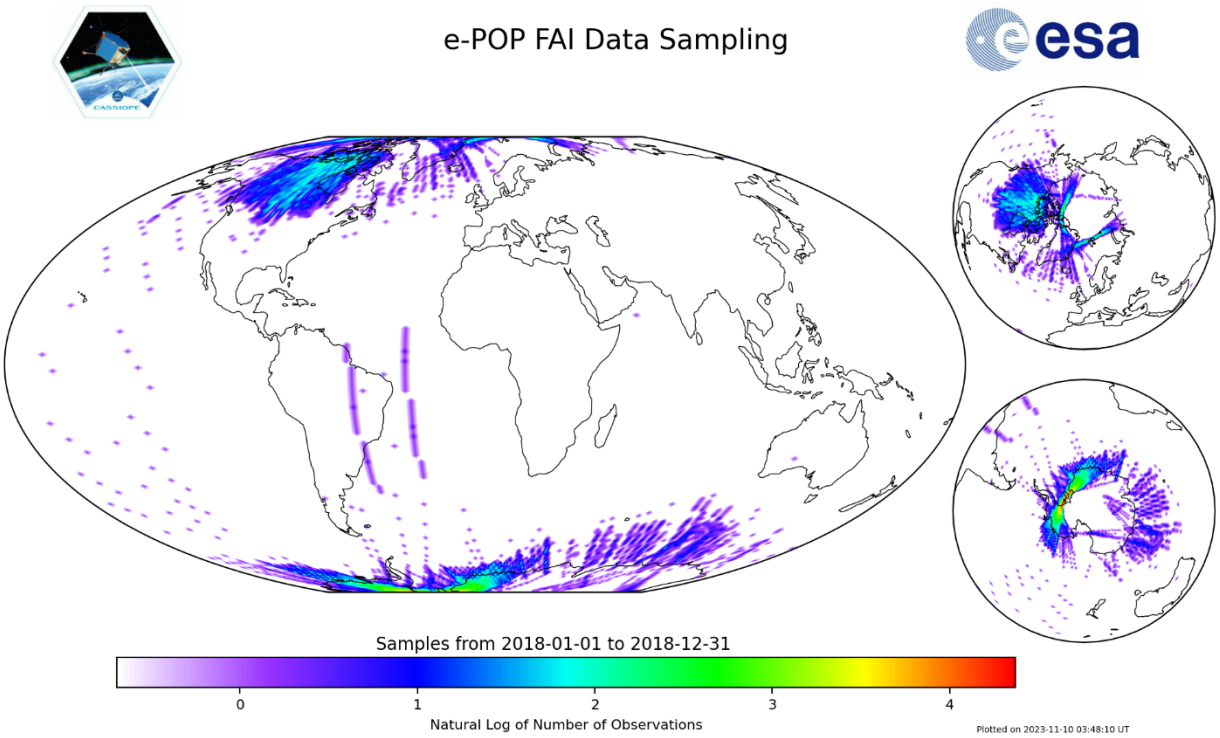

Figure 63: FAI Data Sampling for 2018

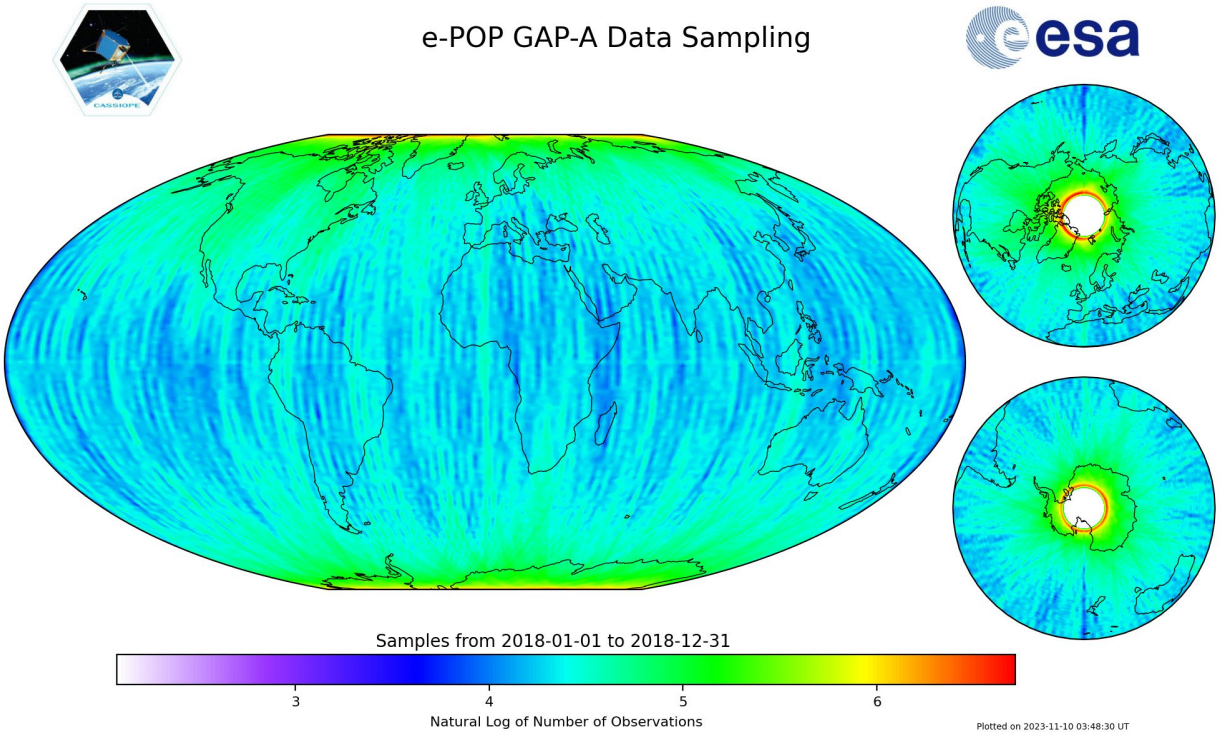

Figure 64: GAP-A Data Sampling for 2018

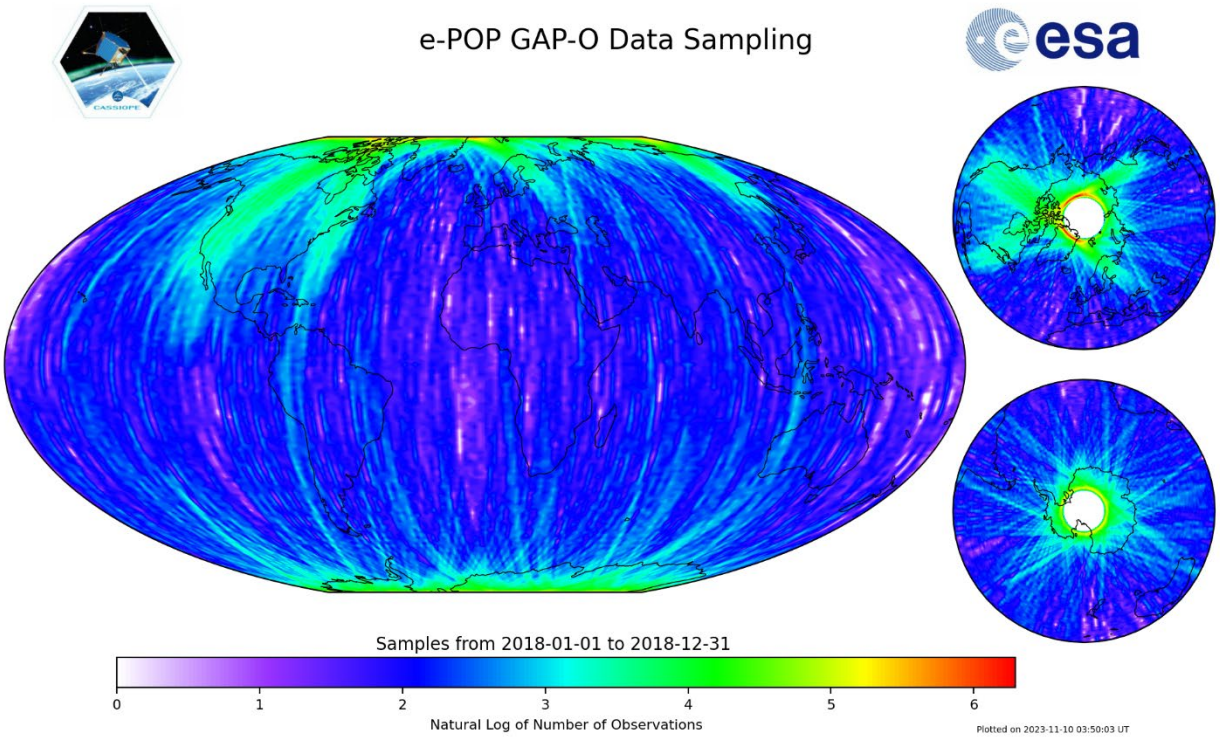

Figure 65: GAP-O Data Sampling for 2018

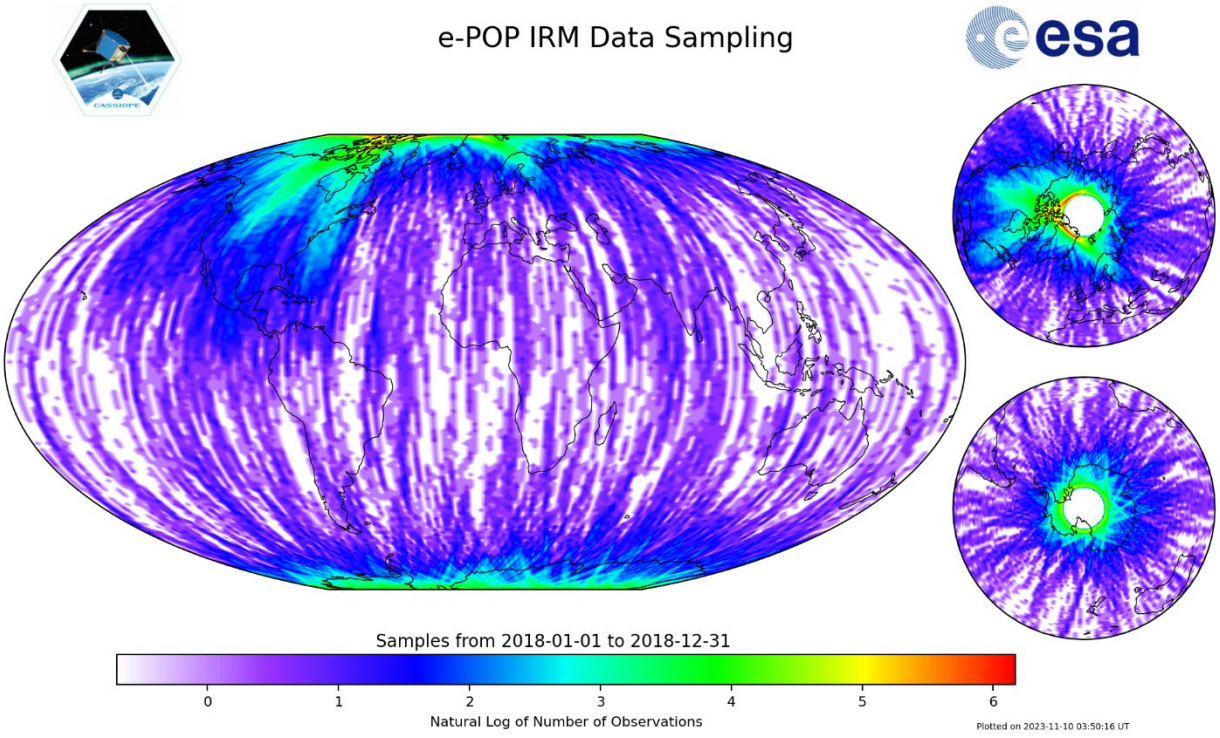

Figure 66: IRM Data Sampling for 2018

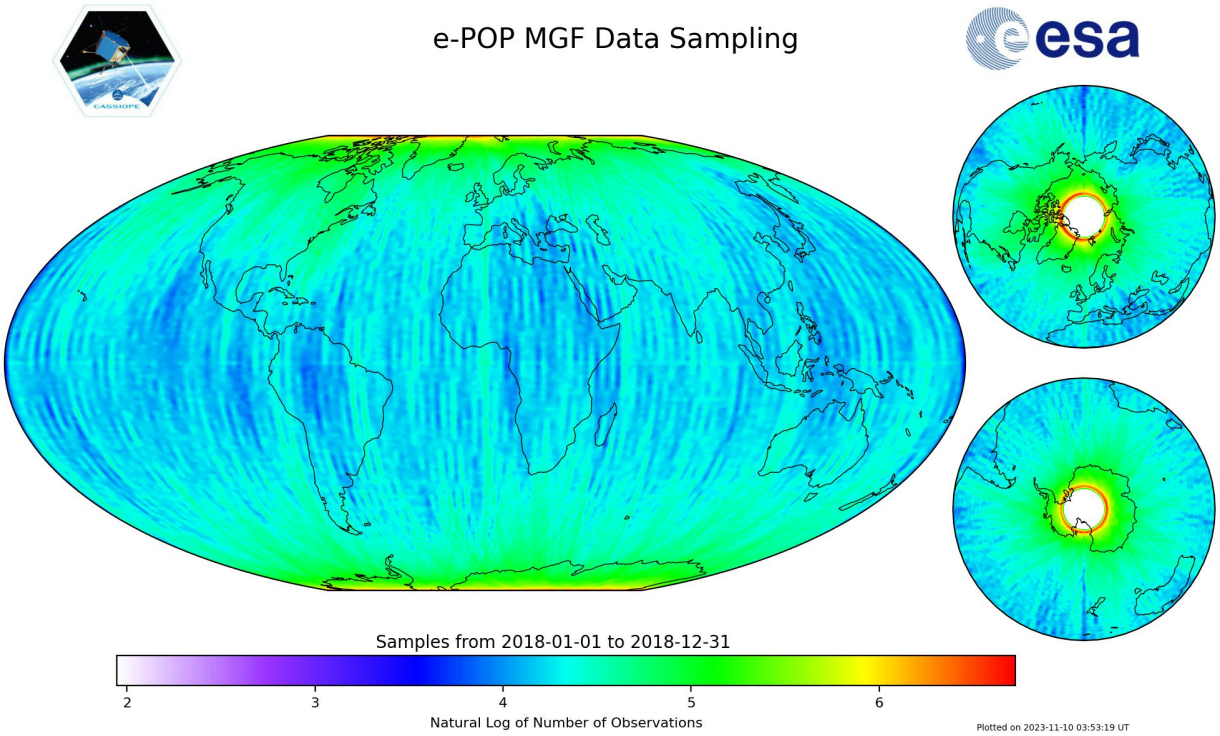

Figure 67: MGF Data Sampling for 2018

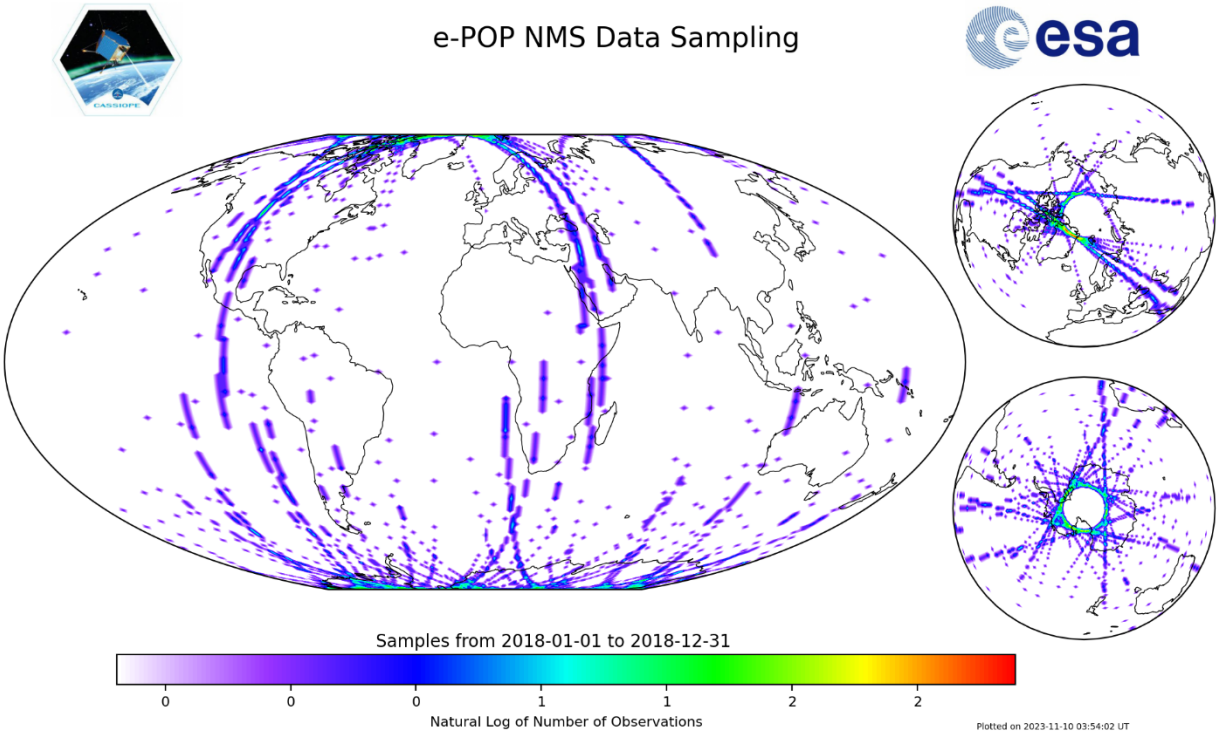

Figure 68: NMS Data Sampling for 2018

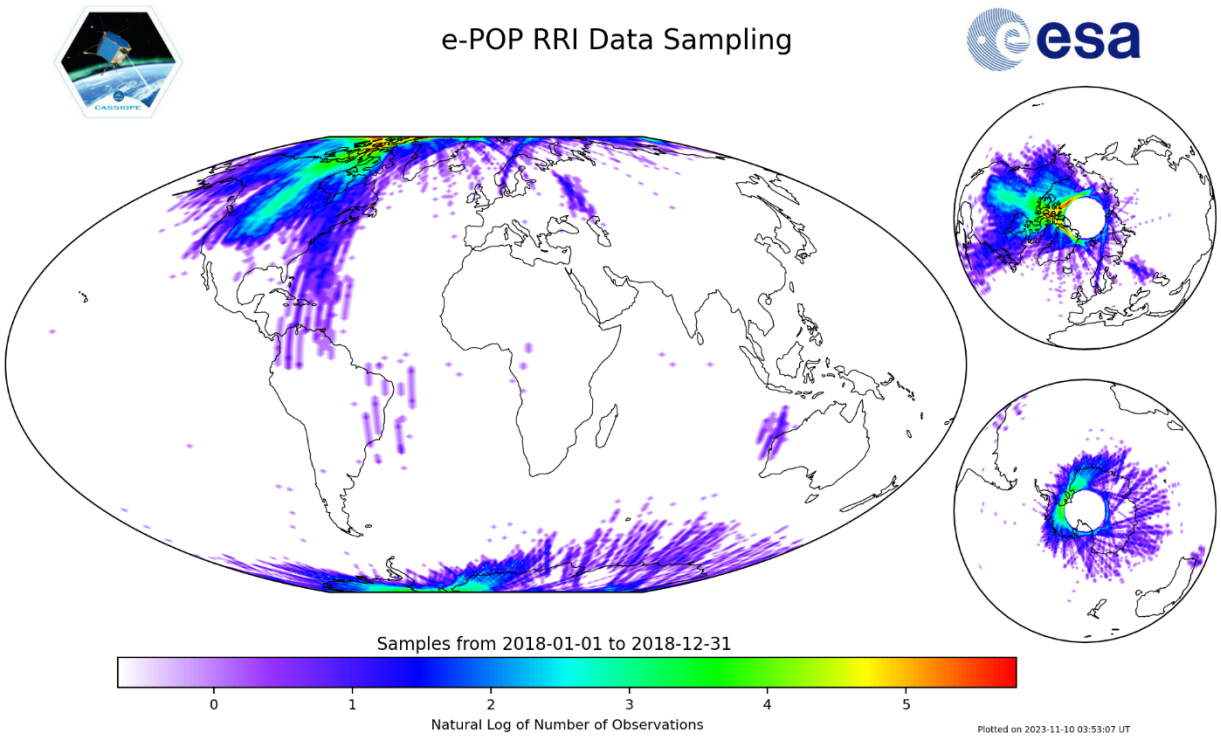

Figure 69: RRI Data Sampling for 2018

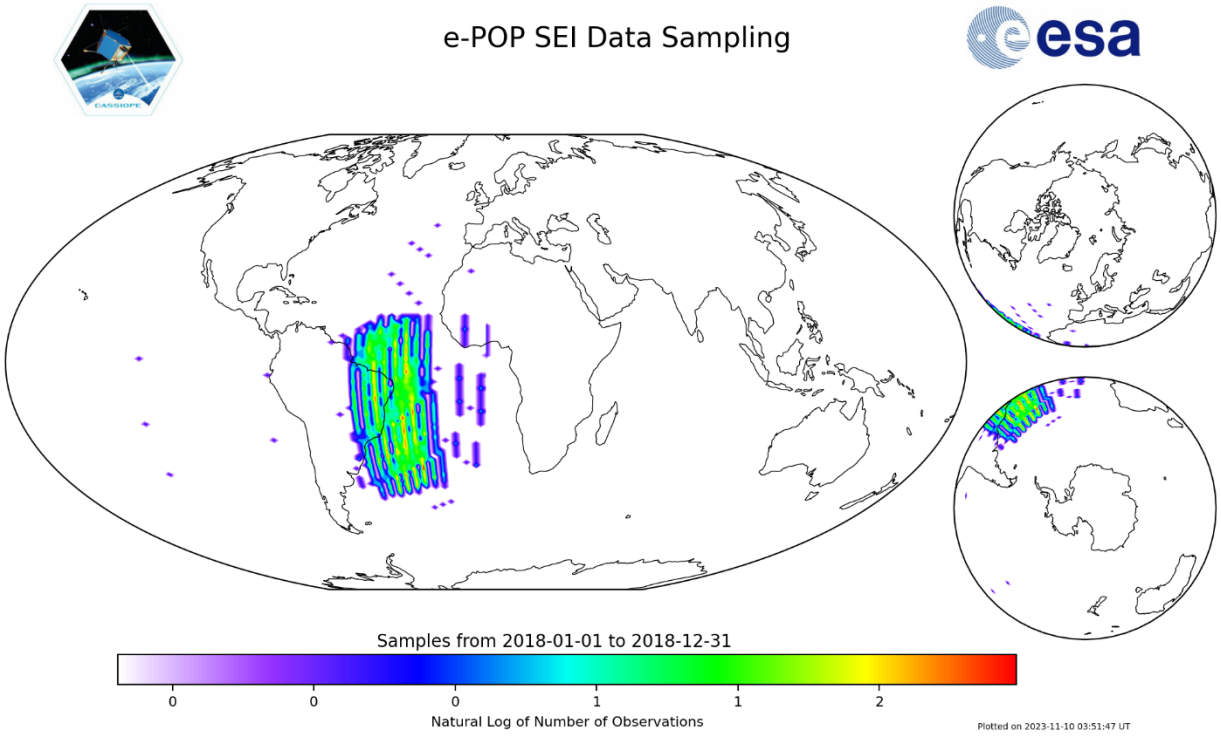

Figure 70: SEI Data Sampling for 2018

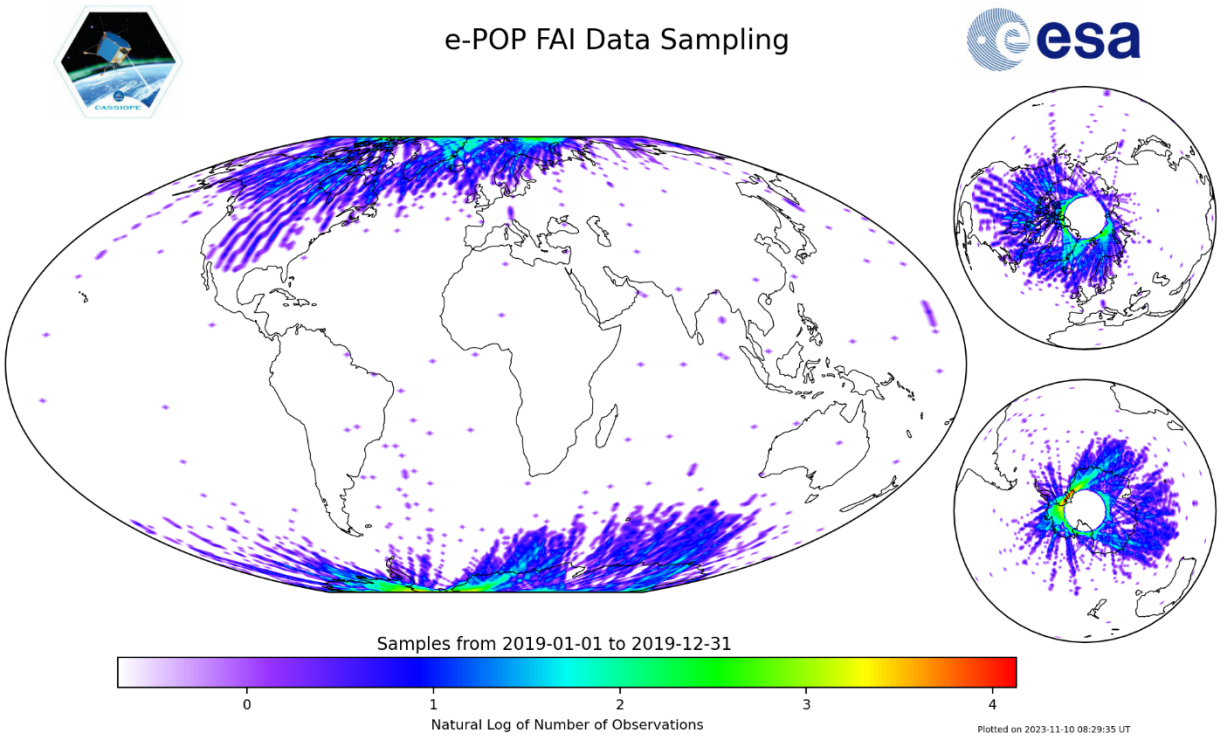

Figure 71: FAI Data Sampling for 2019

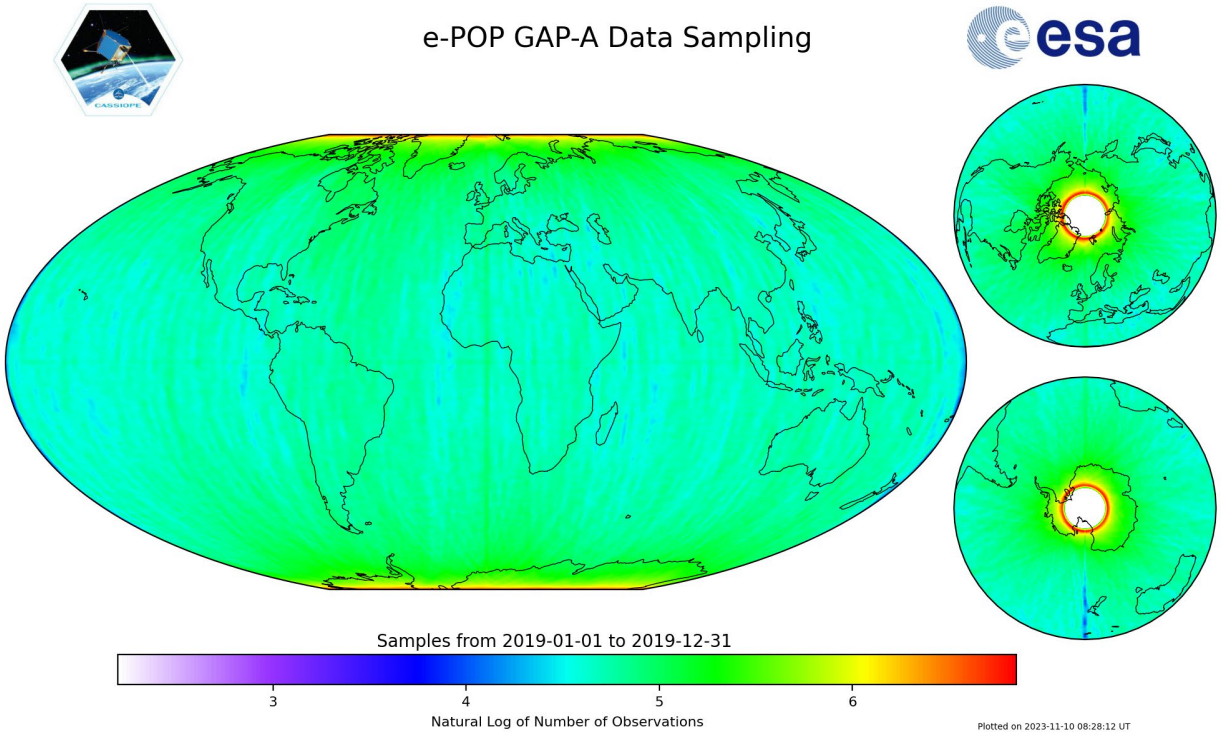

Figure 72: GAP-A Data Sampling for 2019

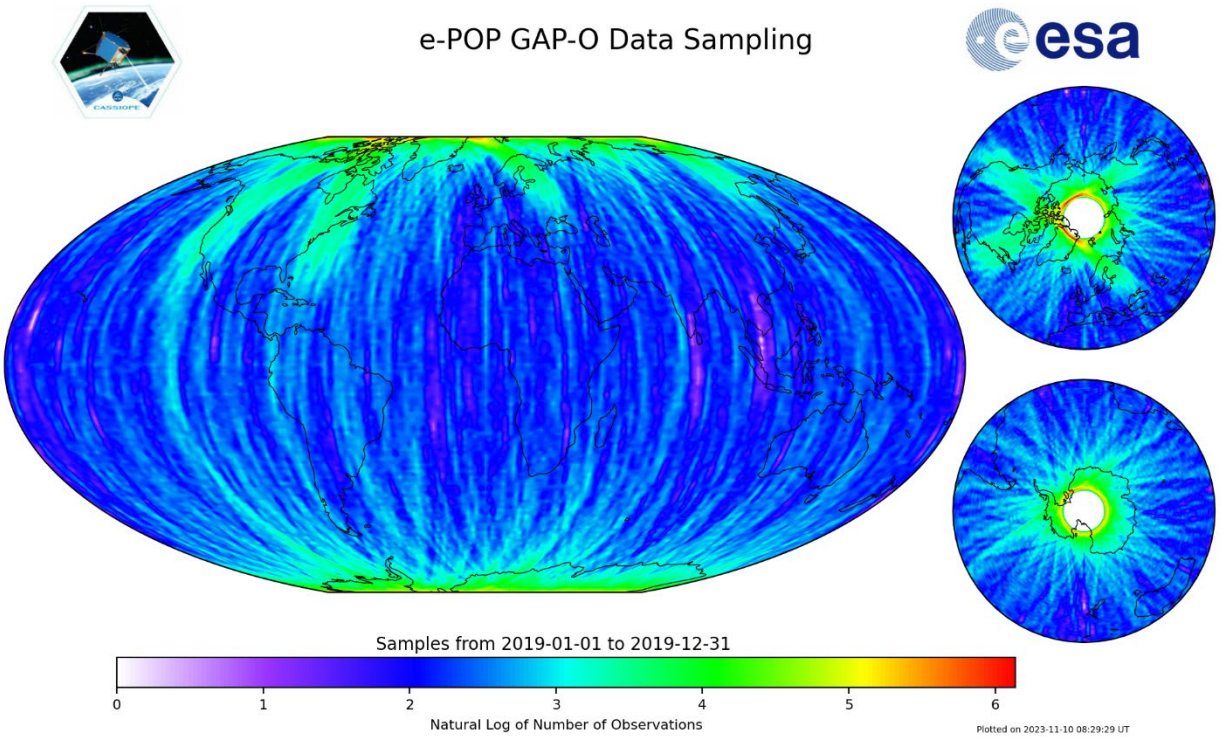

Figure 73: GAP-O Data Sampling for 2019

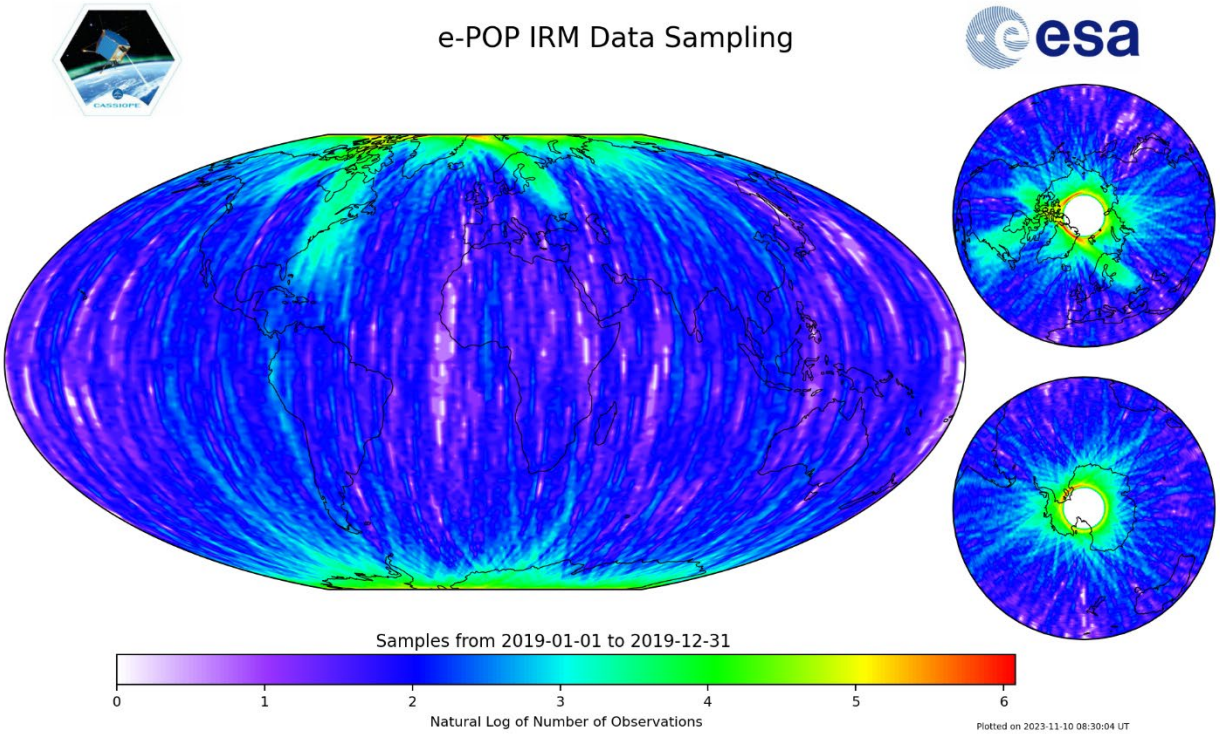

Figure 74: IRM Data Sampling for 2019

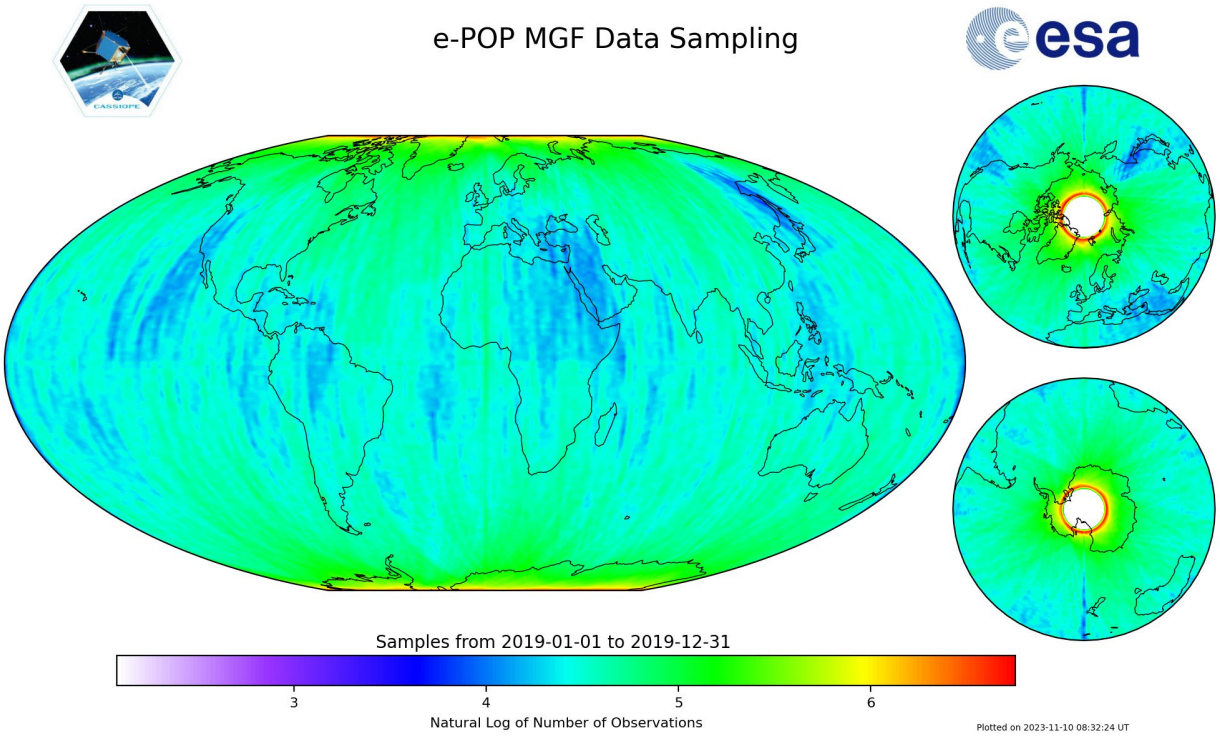

Figure 75: MGF Data Sampling for 2019

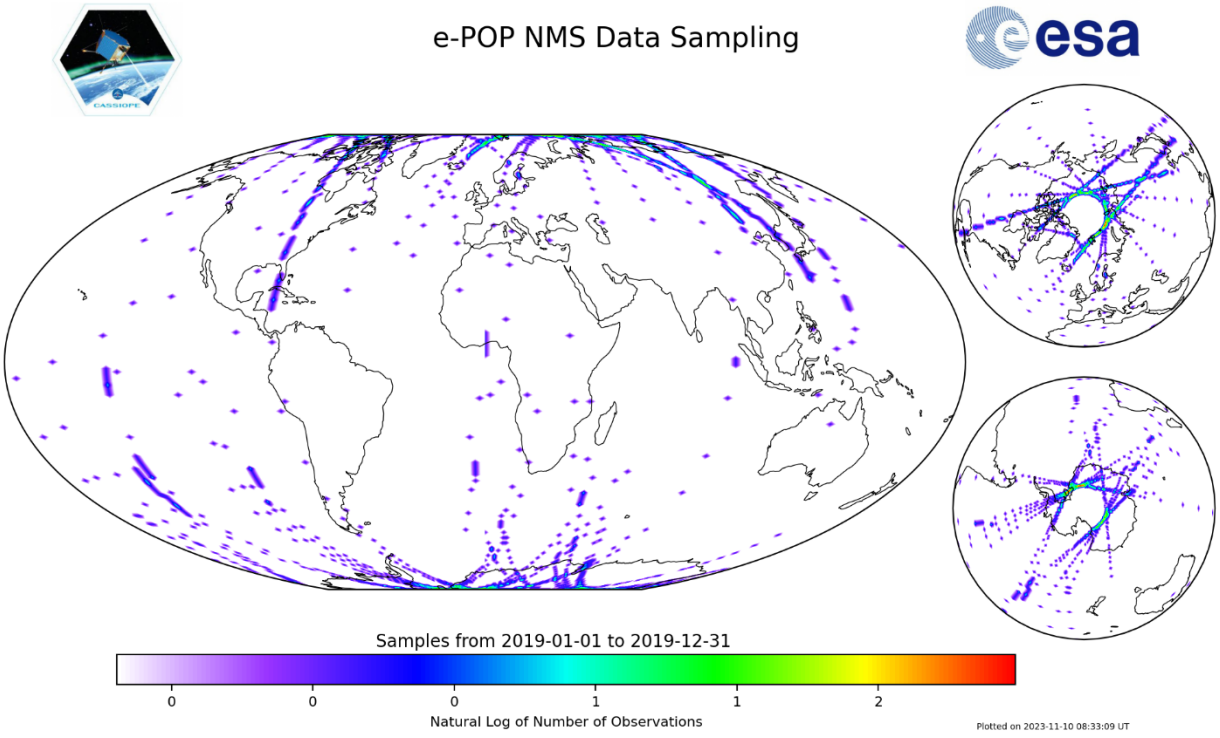

Figure 76: NMS Data Sampling for 2019

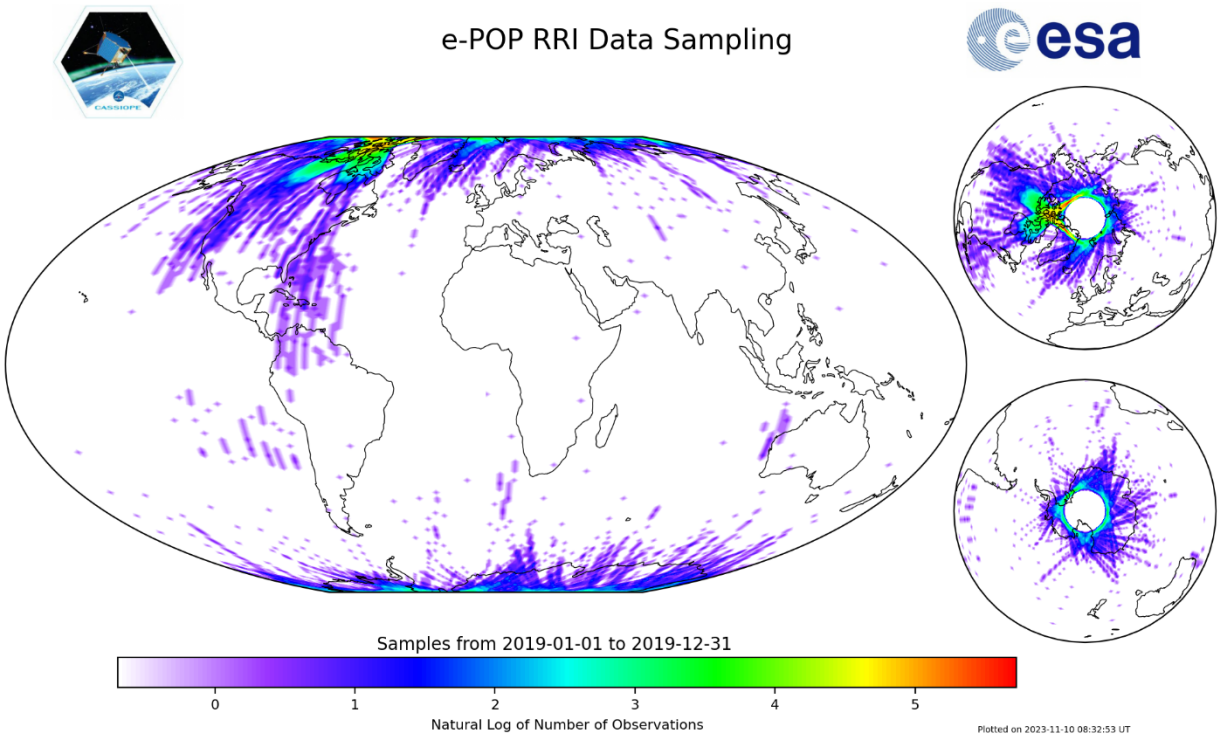

Figure 77: RRI Data Sampling for 2019

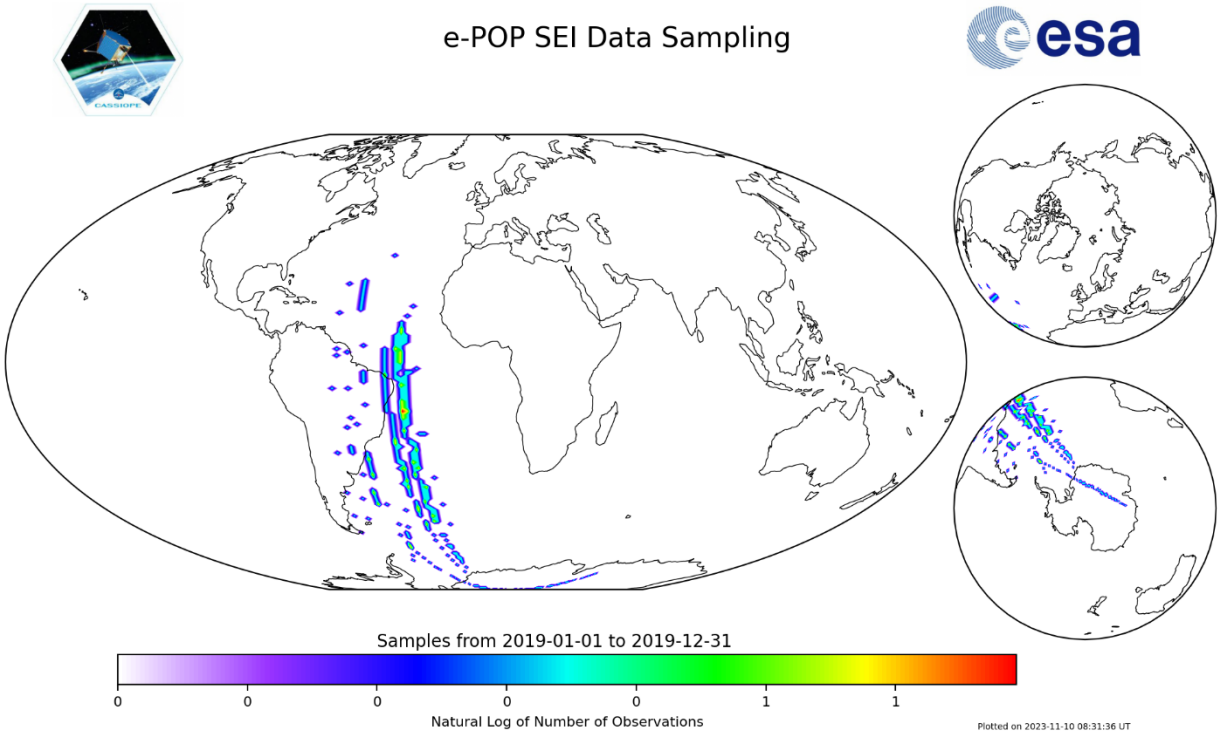

Figure 78: SEI Data Sampling for 2019

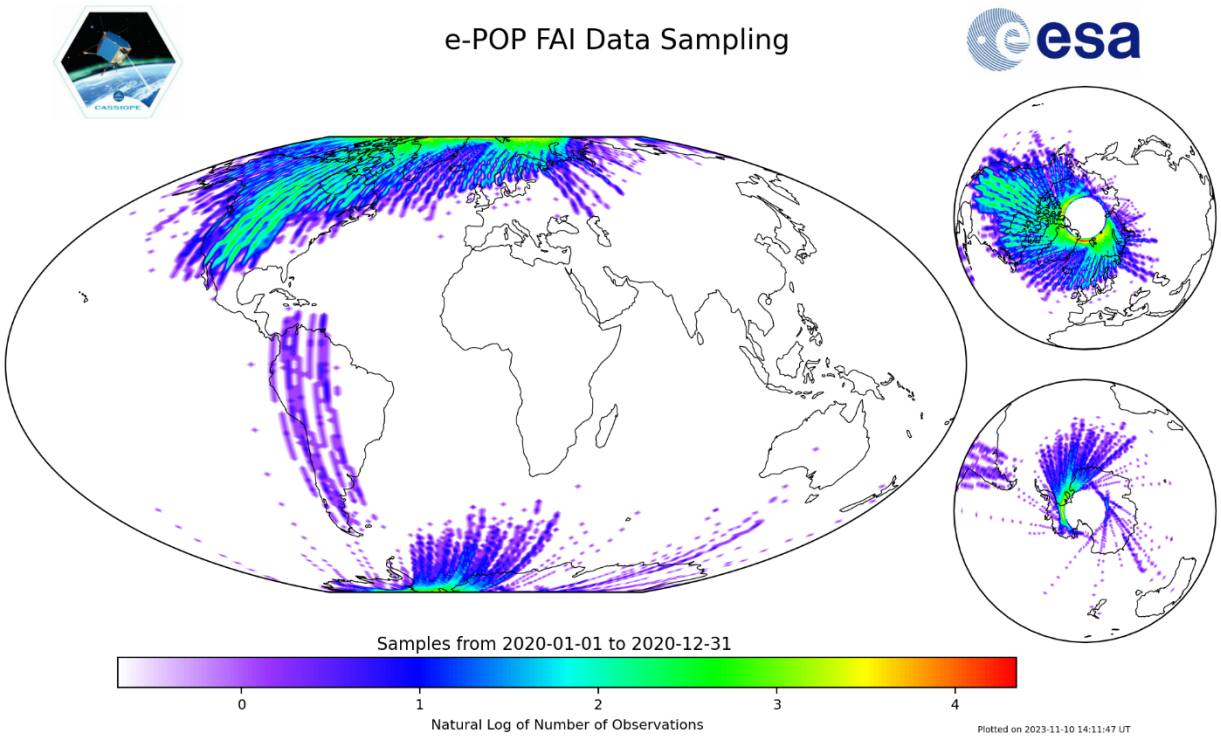

Figure 79: FAI Data Sampling for 2020

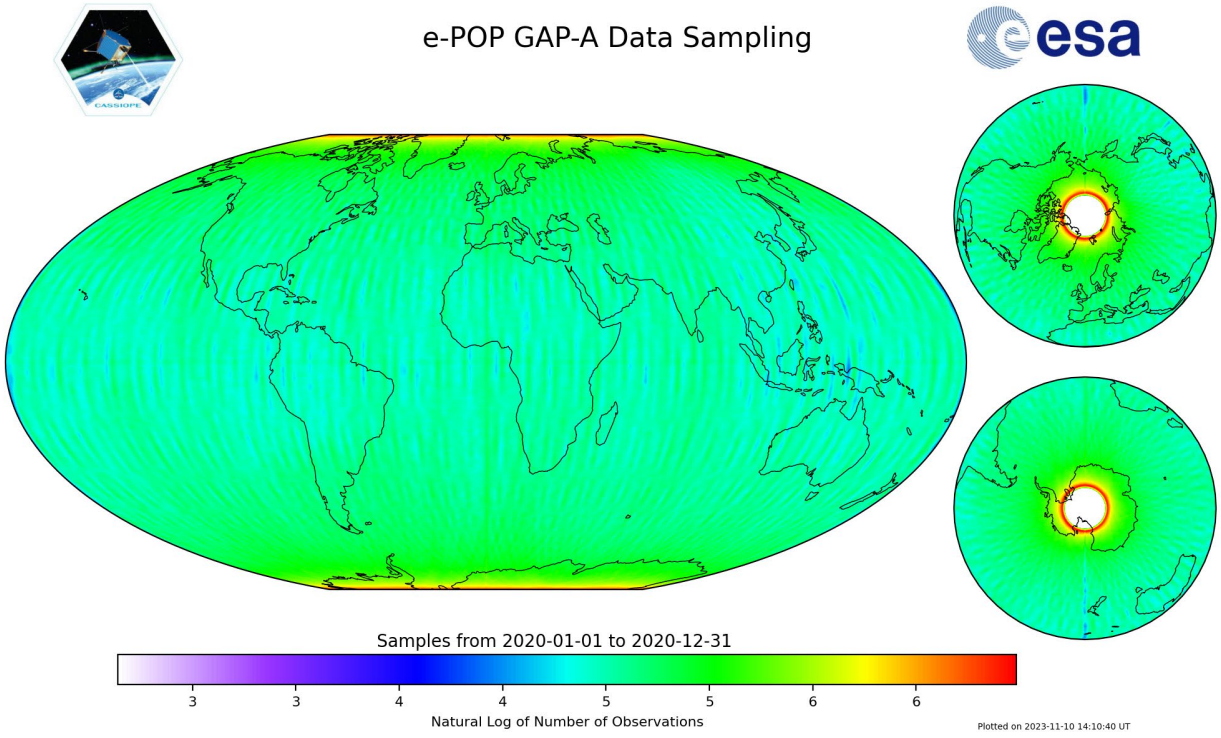

Figure 80: GAP-A Data Sampling for 2020

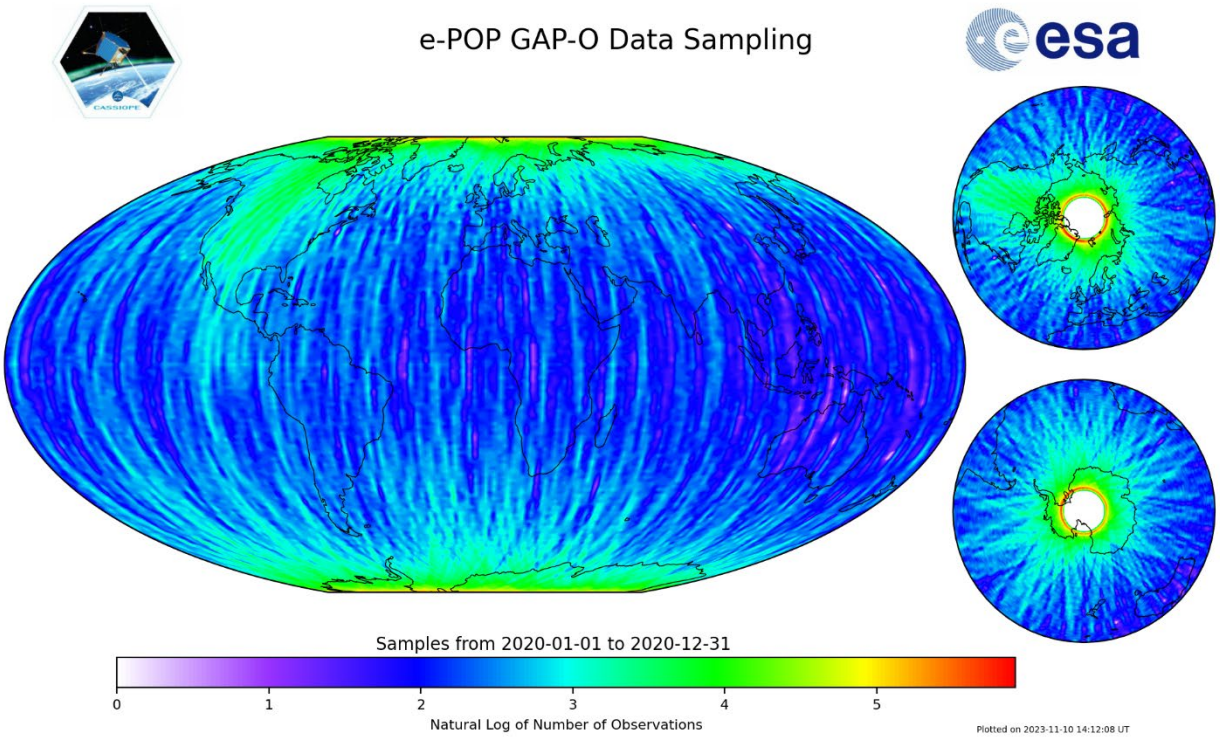

Figure 81: GAP-O Data Sampling for 2020

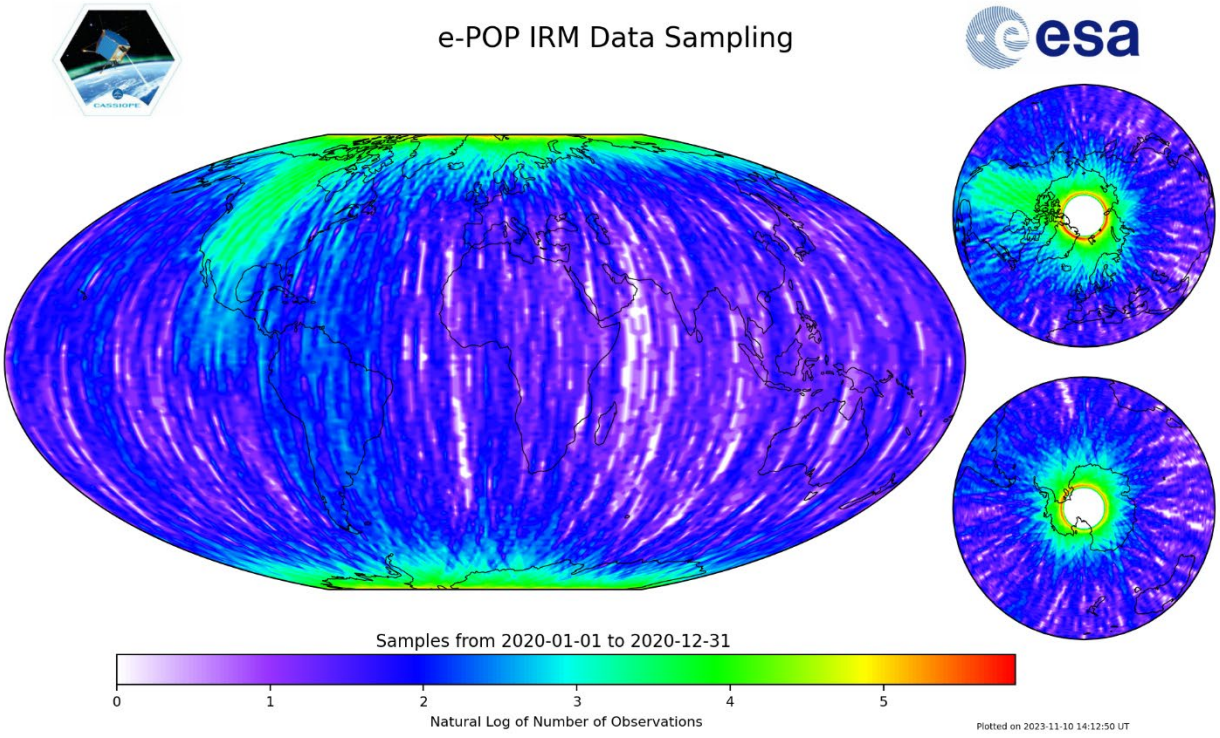

Figure 82: IRM Data Sampling for 2020

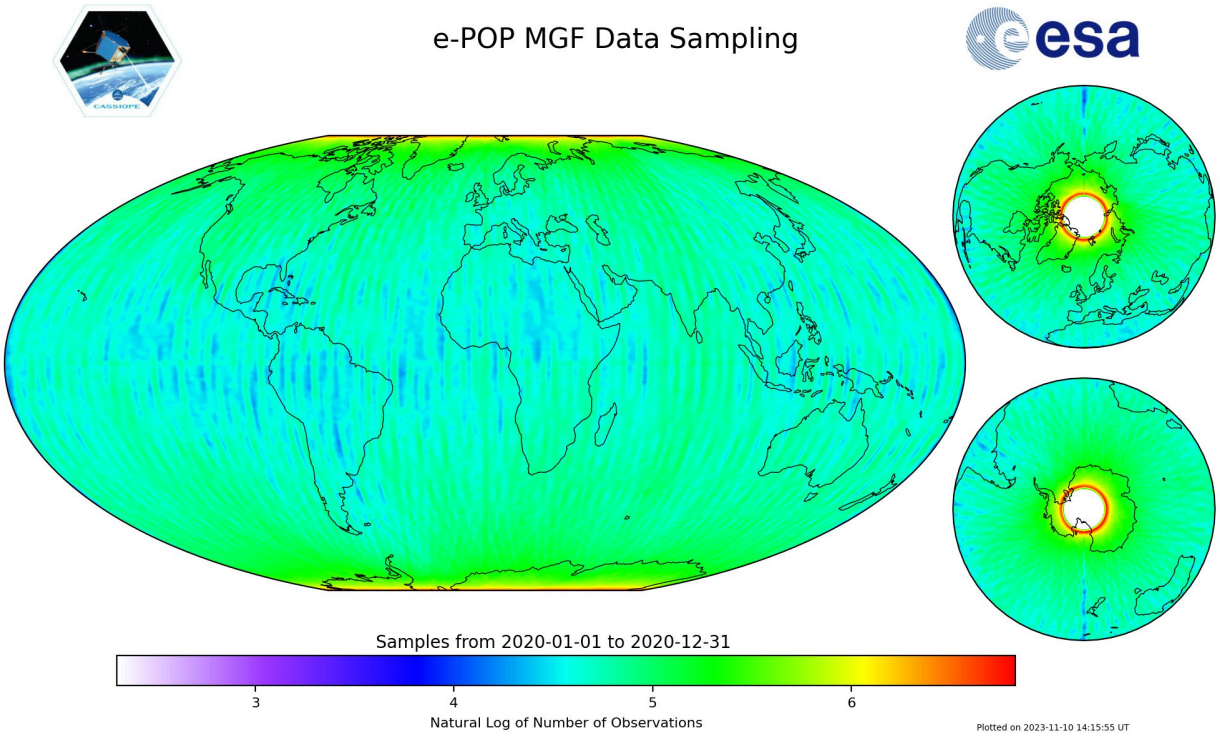

Figure 83: MGF Data Sampling for 2020

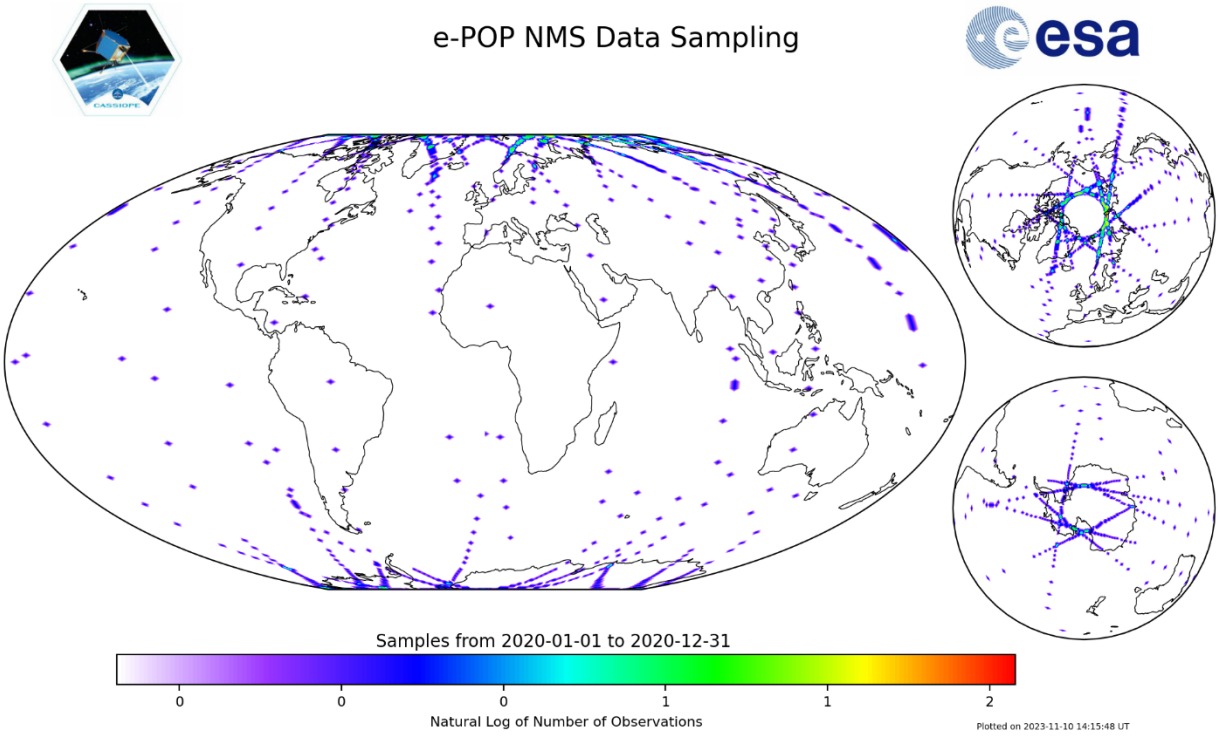

Figure 84: NMS Data Sampling for 2020

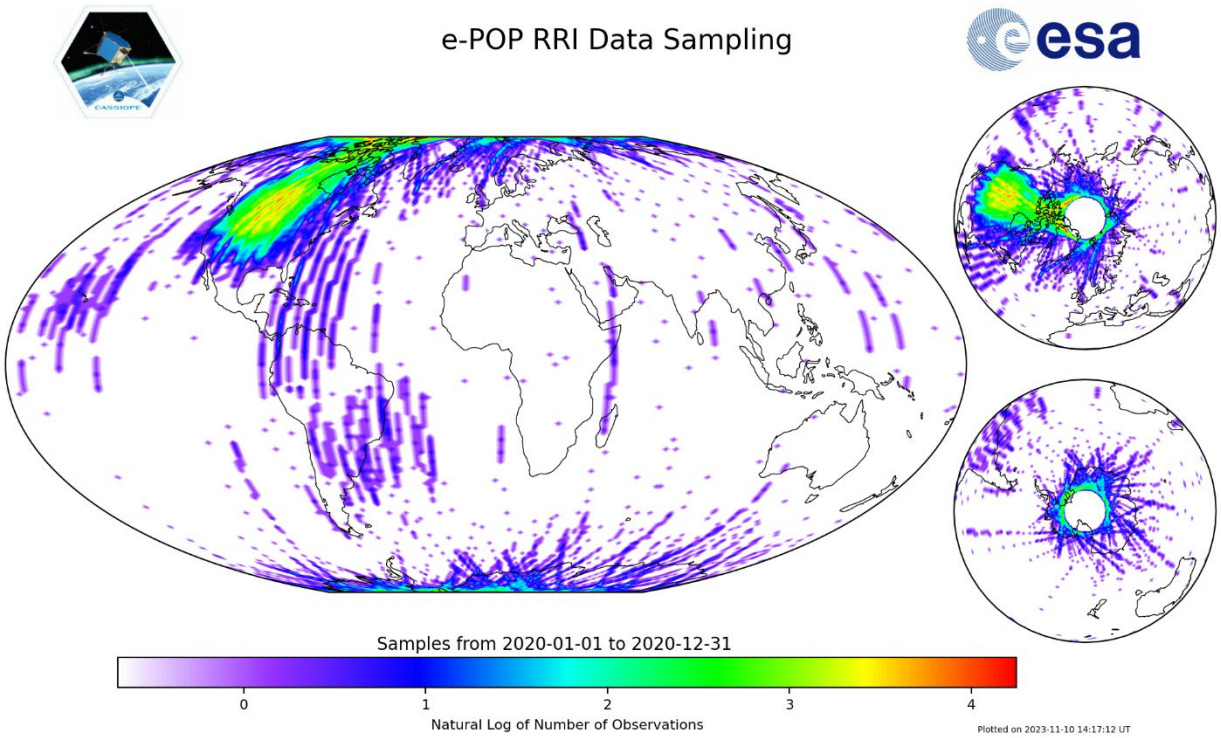

Figure 85: RRI Data Sampling for 2020

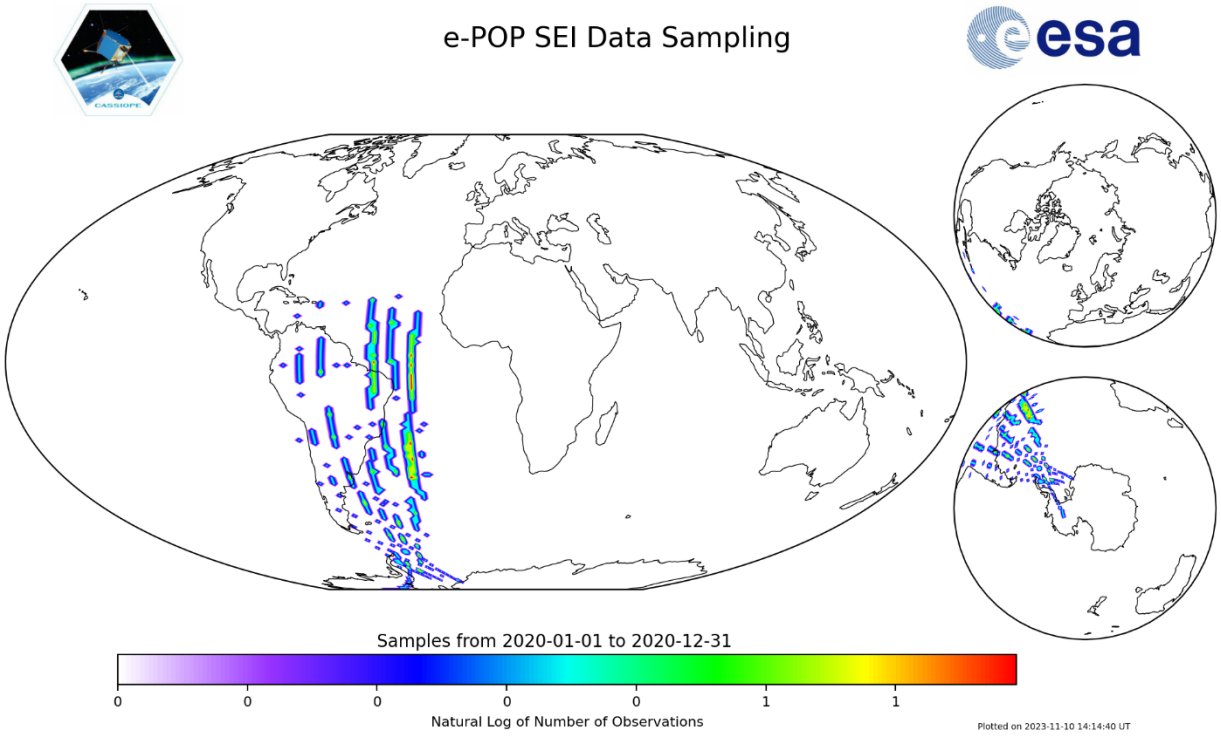

Figure 86: SEI Data Sampling for 2020

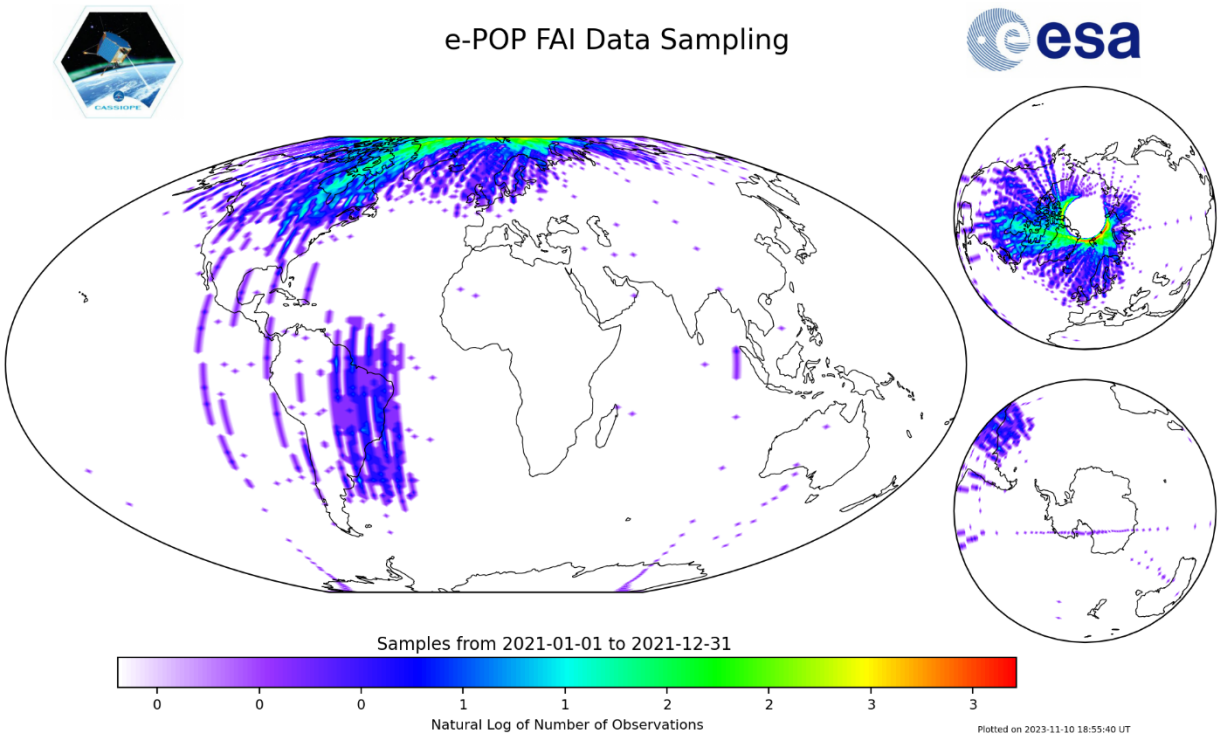

Figure 87: FAI Data Sampling for 2021

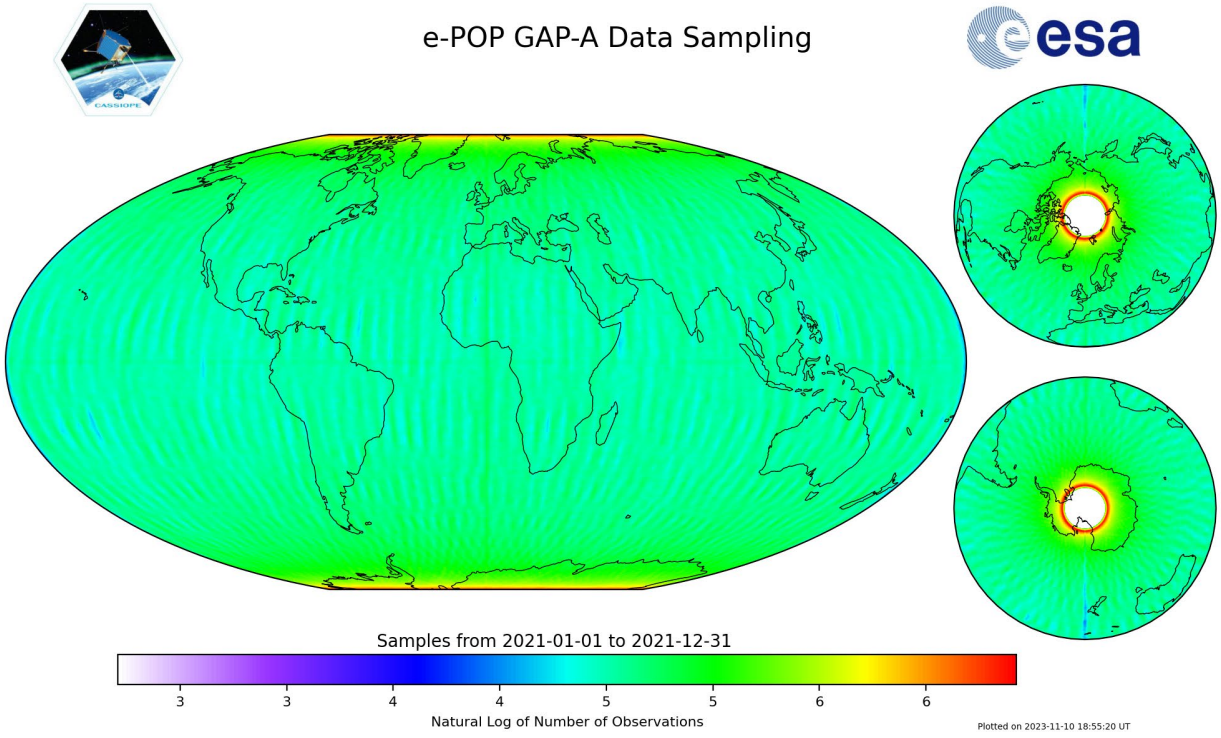

Figure 88: GAP-A Data Sampling for 2021

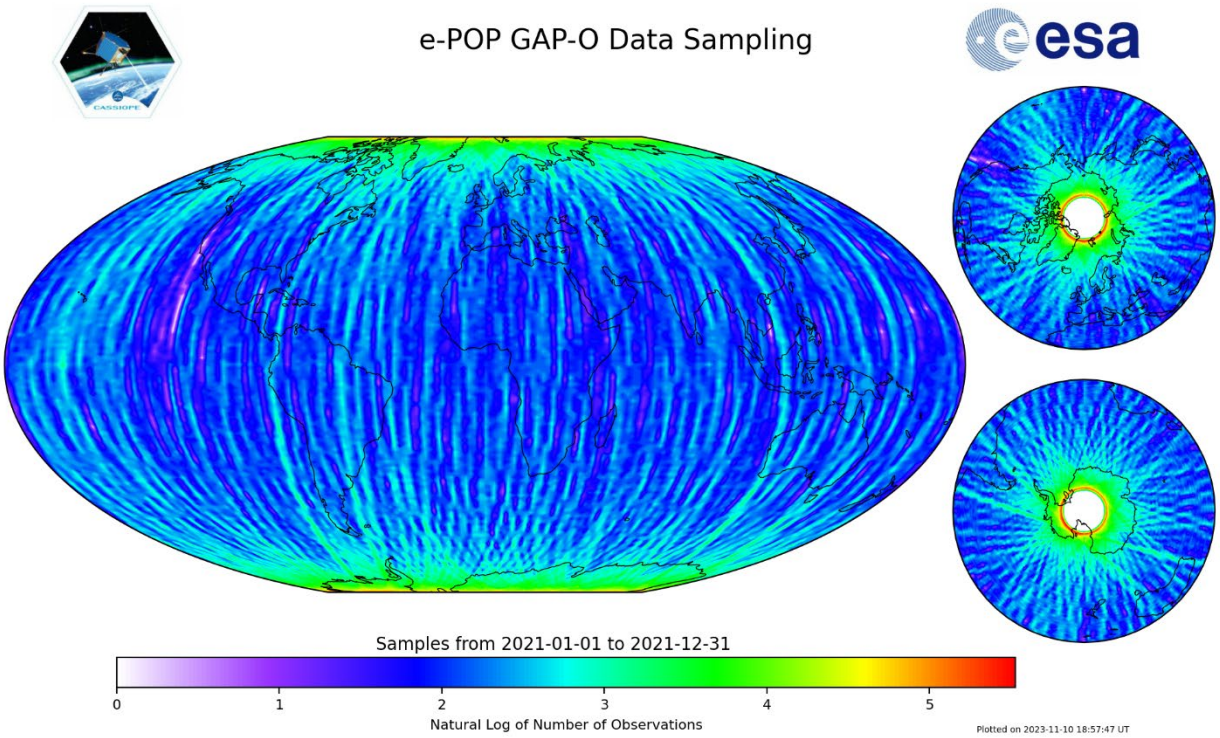

Figure 89: GAP-O Data Sampling for 2021

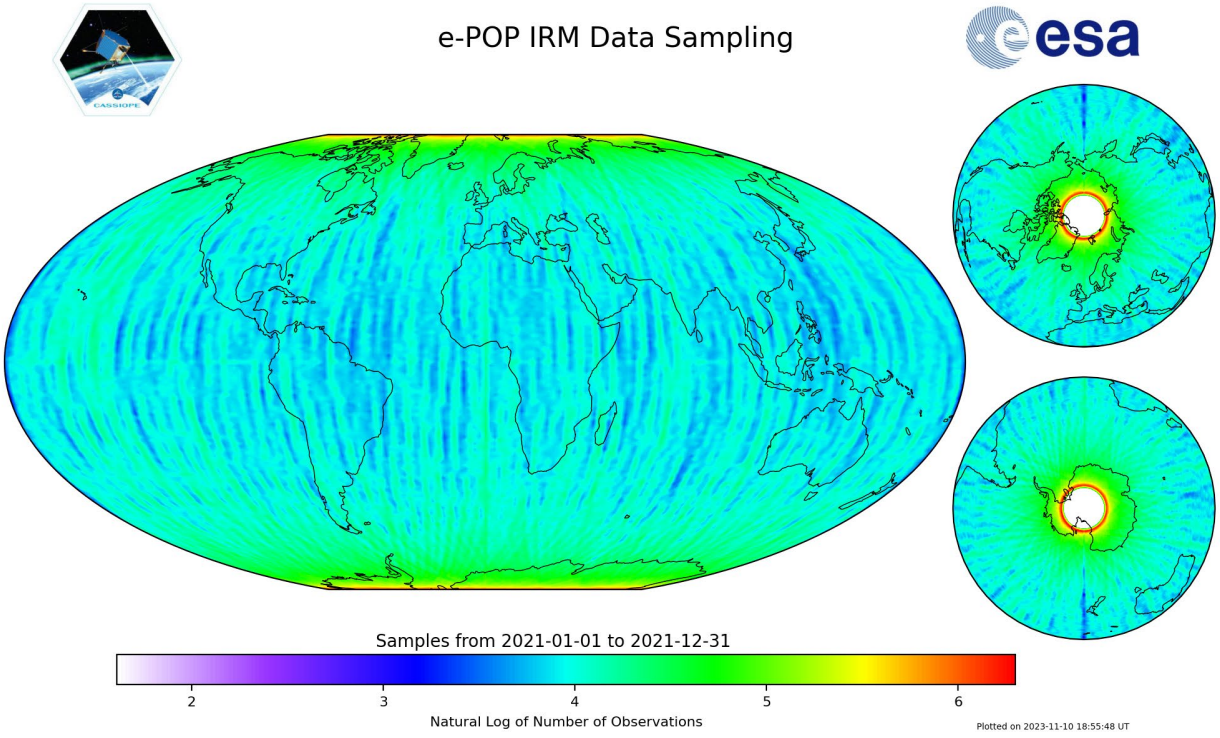

Figure 90: IRM Data Sampling for 2021

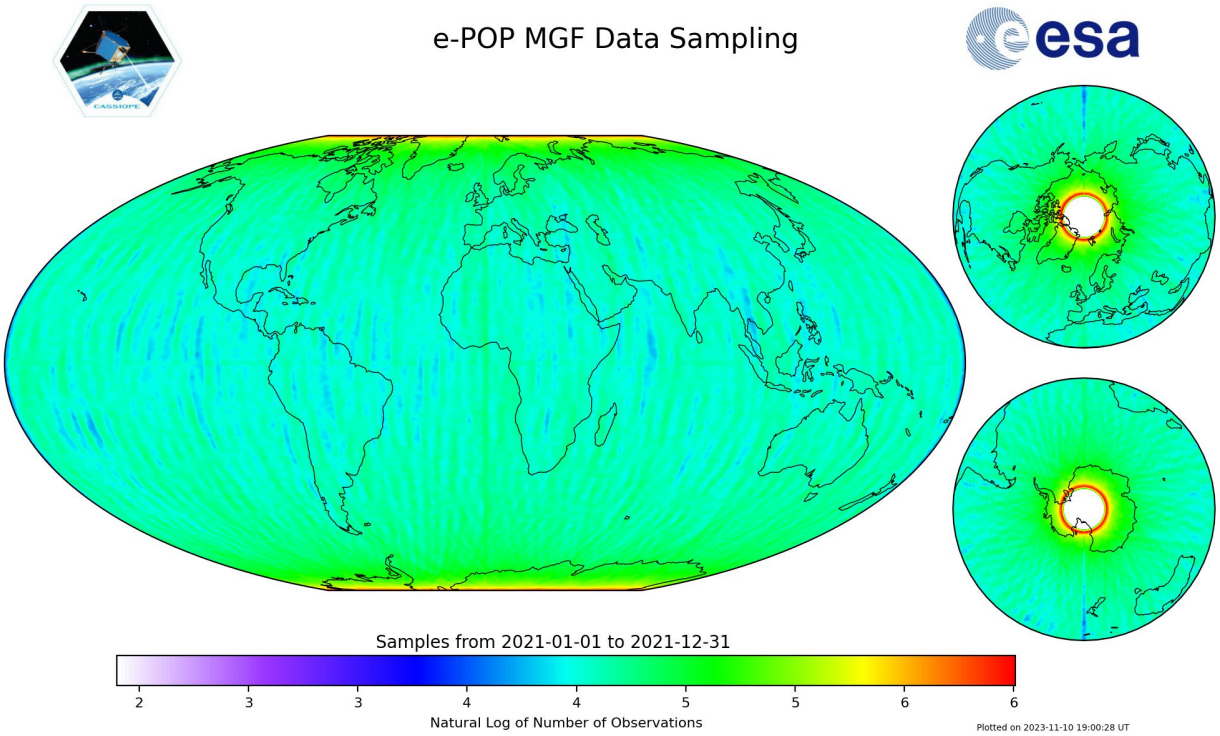

Figure 91: MGF Data Sampling for 2021

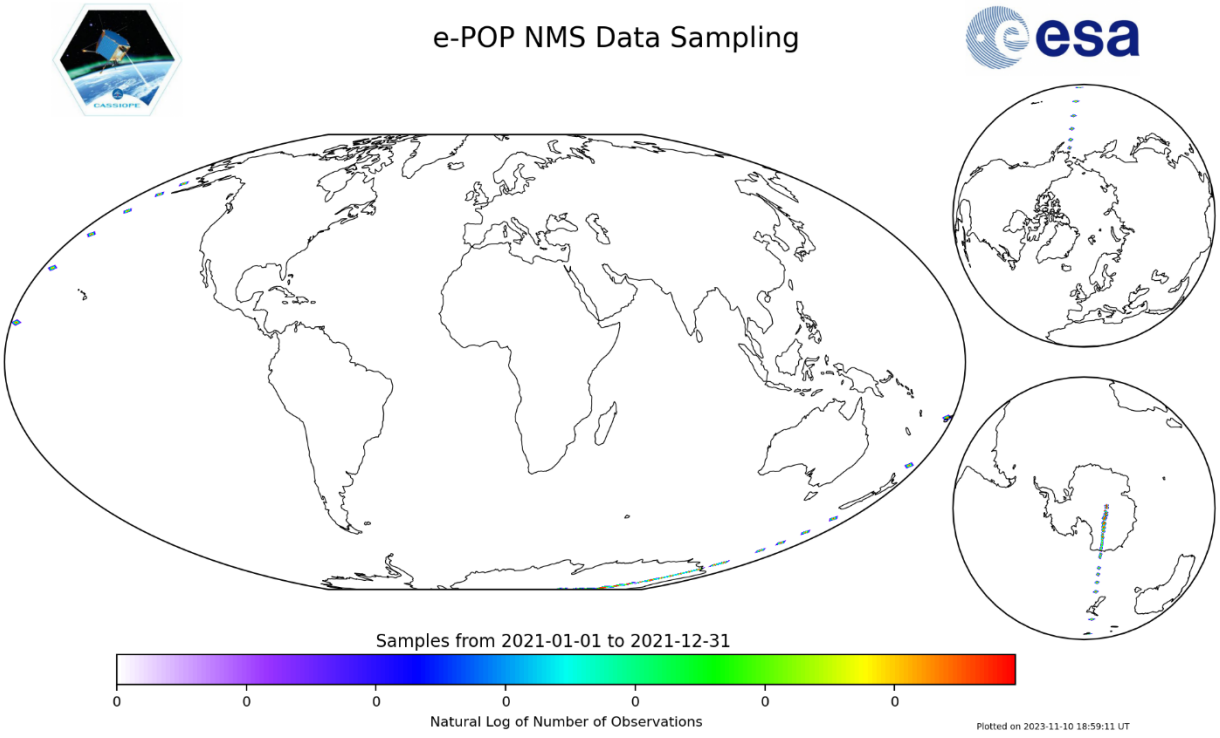

Figure 92: NMS Data Sampling for 2021

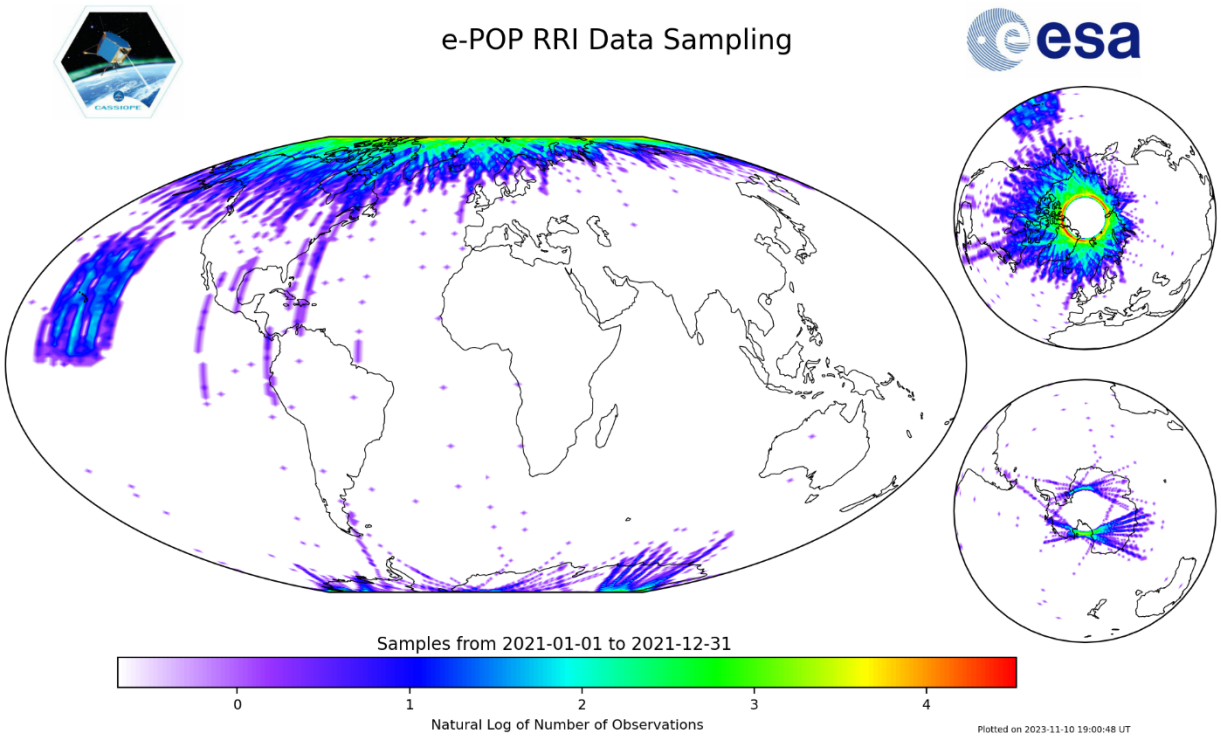

Figure 93: RRI Data Sampling for 2021

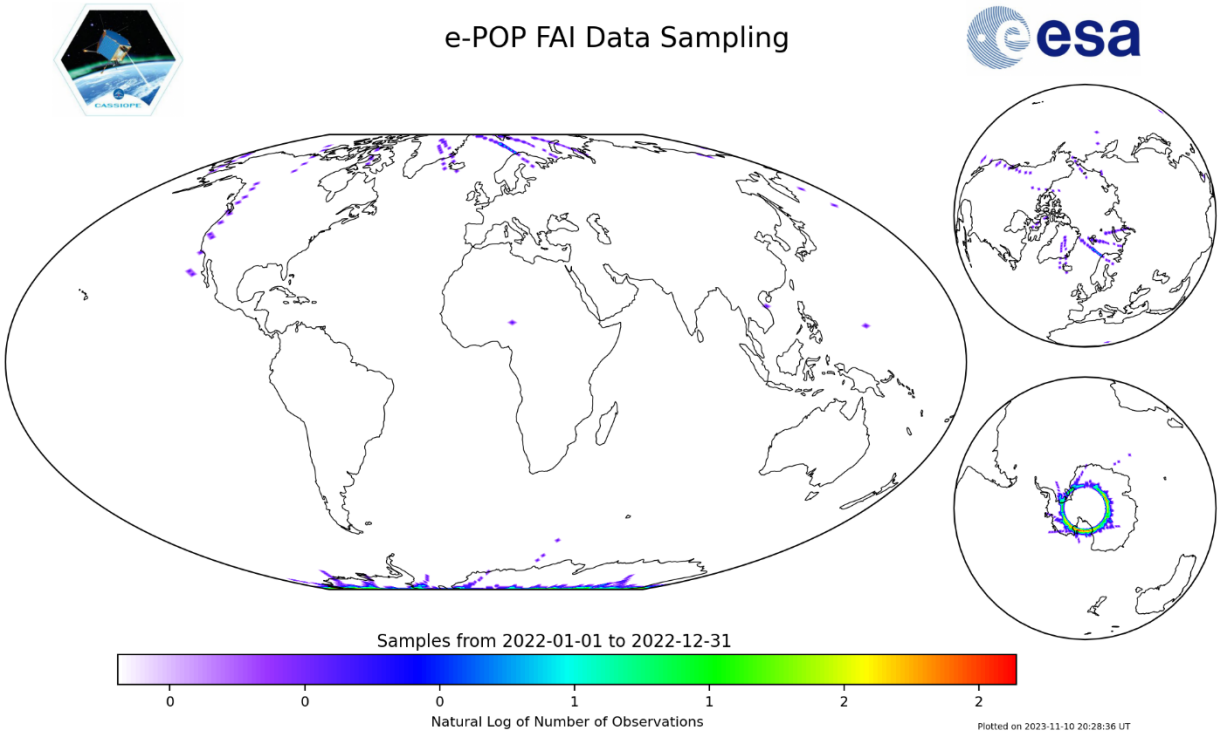

Figure 94: FAI Data Sampling for 2022

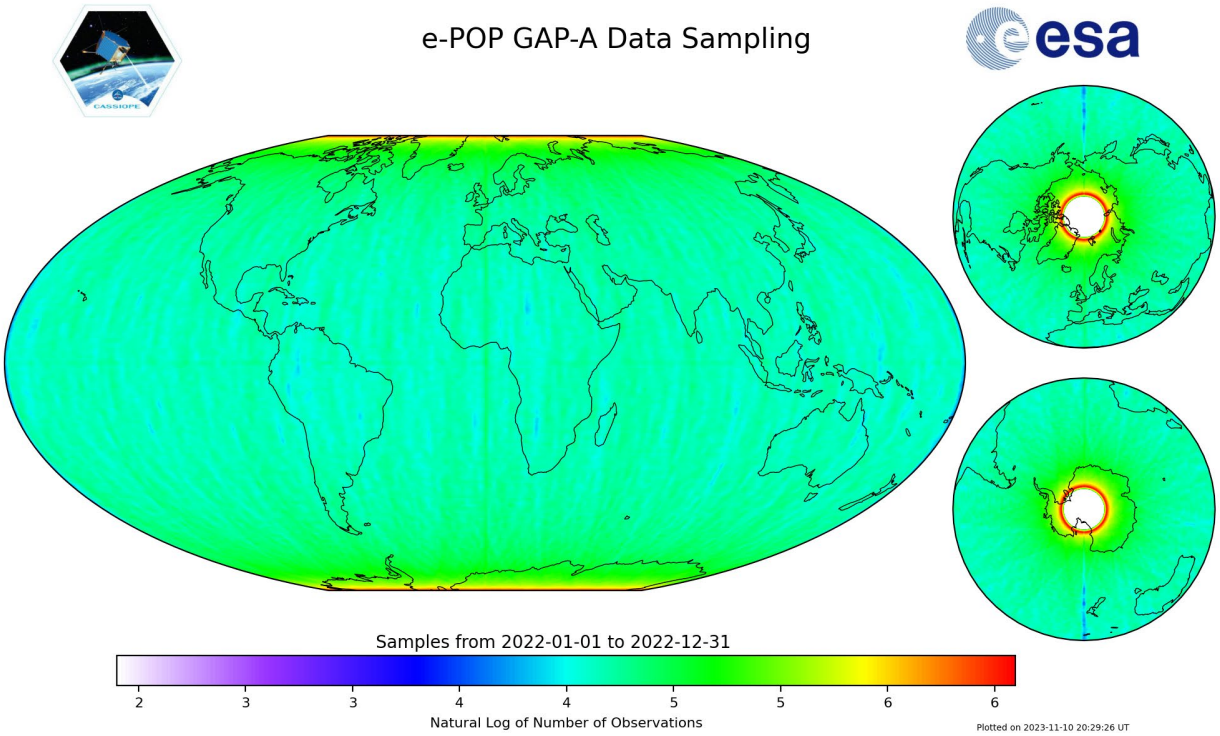

Figure 95: GAP-A Data Sampling for 2022

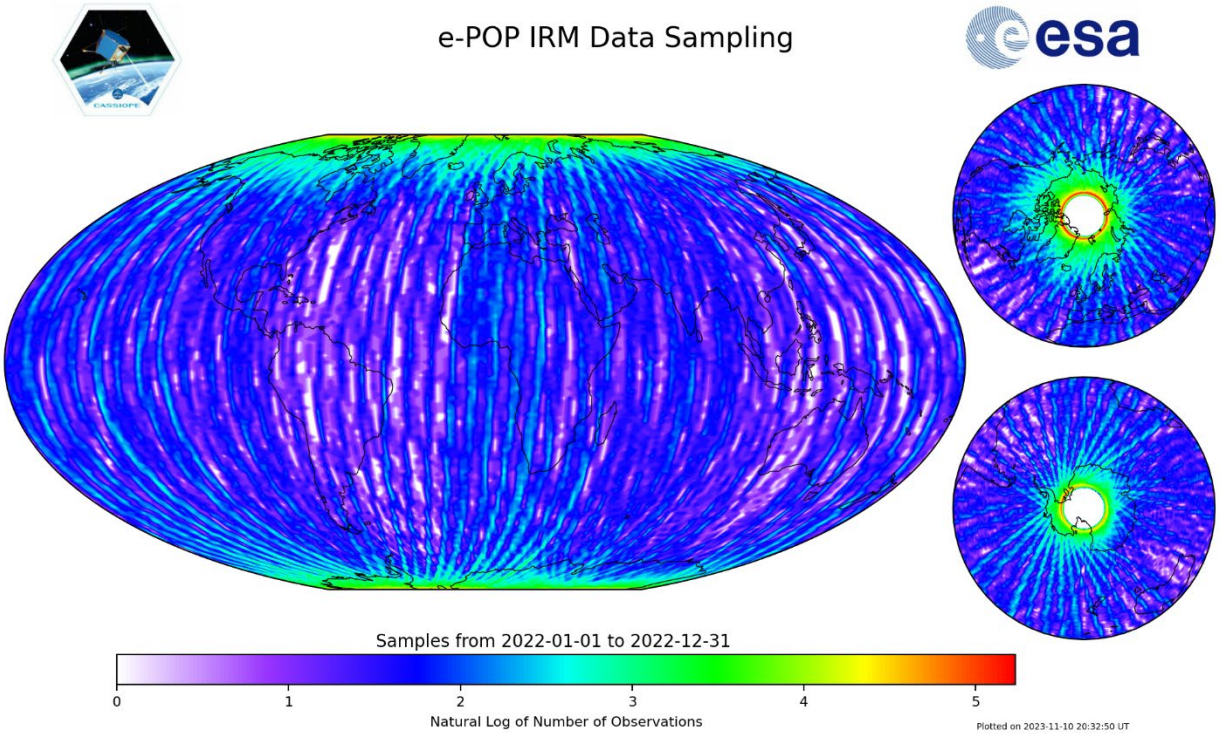

Figure 96: IRM Data Sampling for 2022

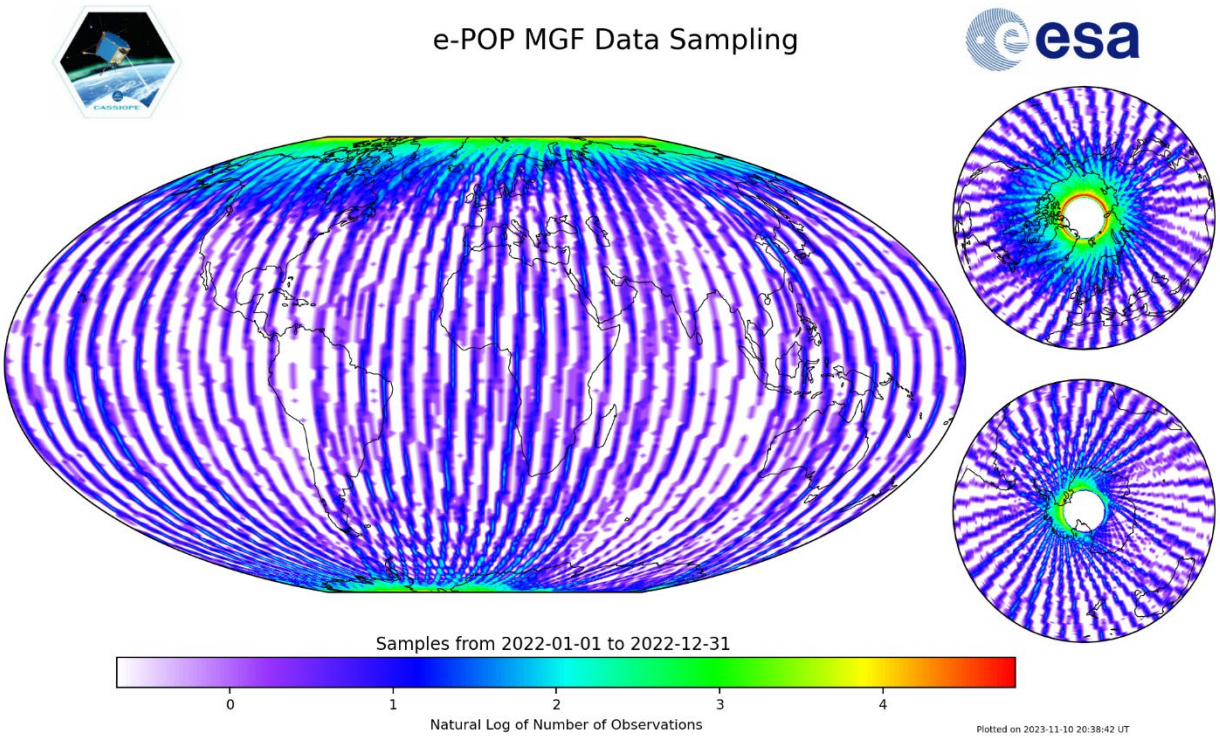

Figure 97: MGF Data Sampling for 2022

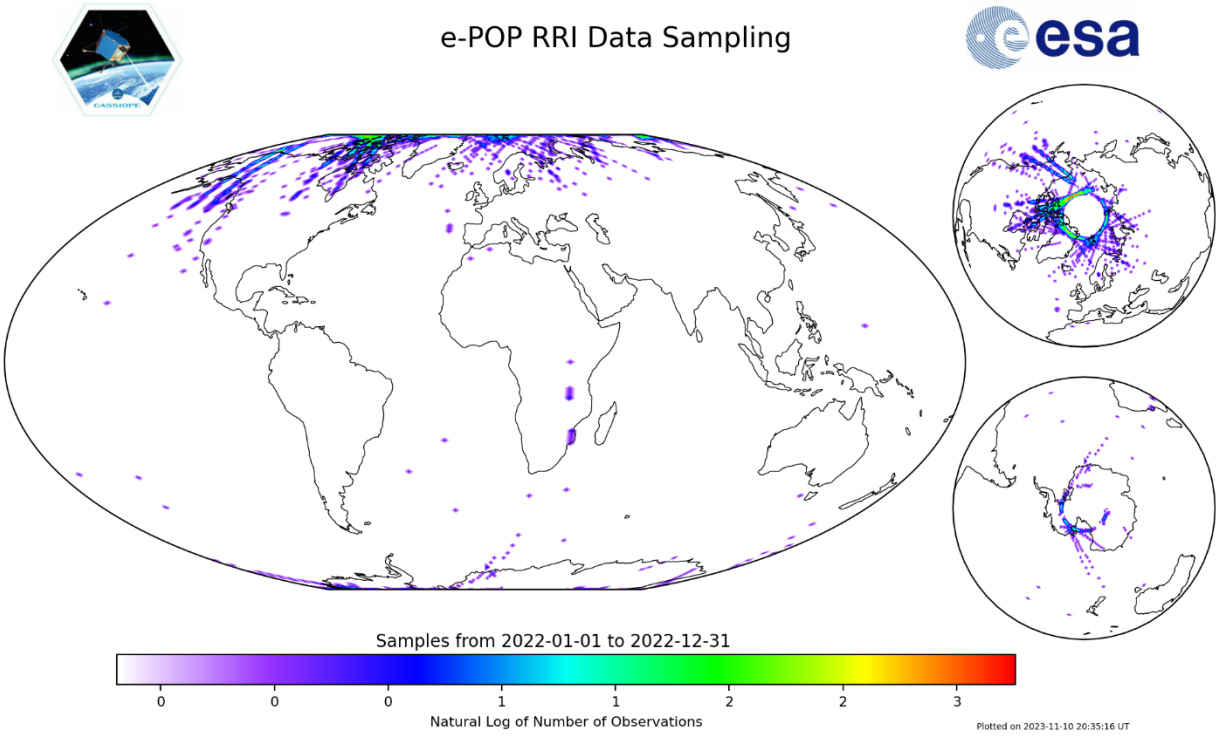

Figure 98: RRI Data Sampling for 2022

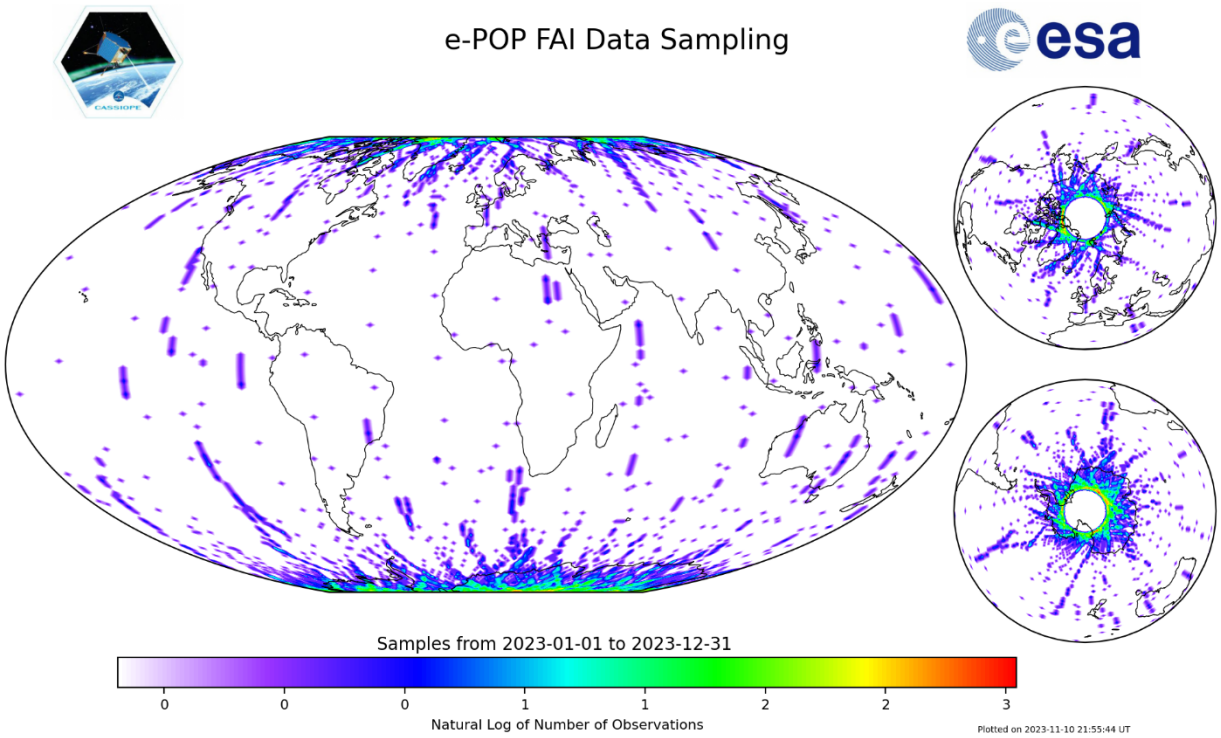

Figure 99: FAI Data Sampling for 2023

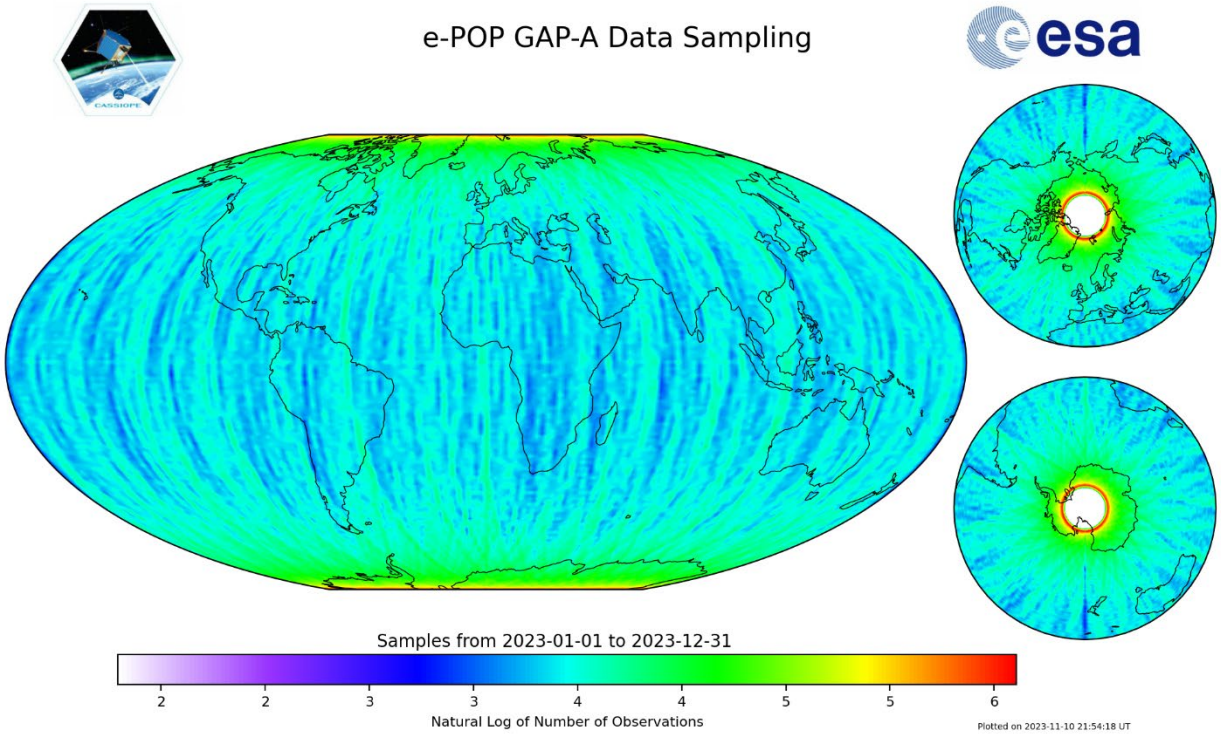

Figure 100: GAP-A Data Sampling for 2023

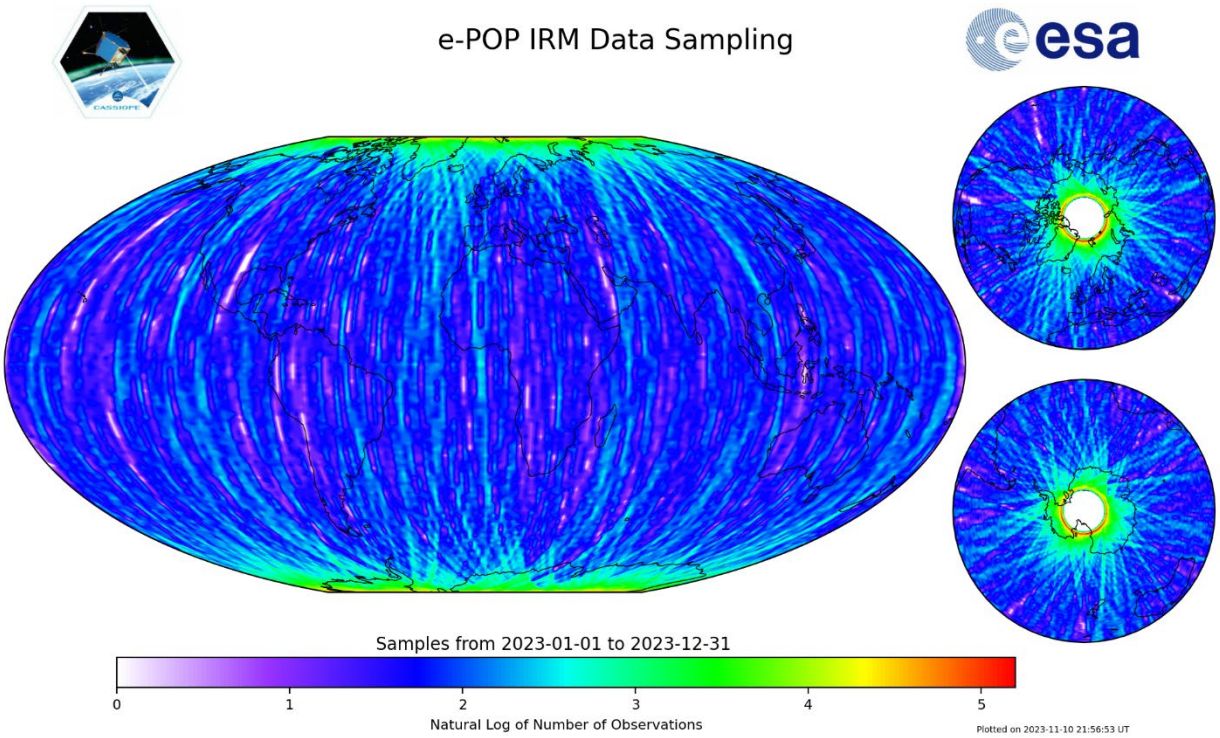

Figure 101: IRM Data Sampling for 2023

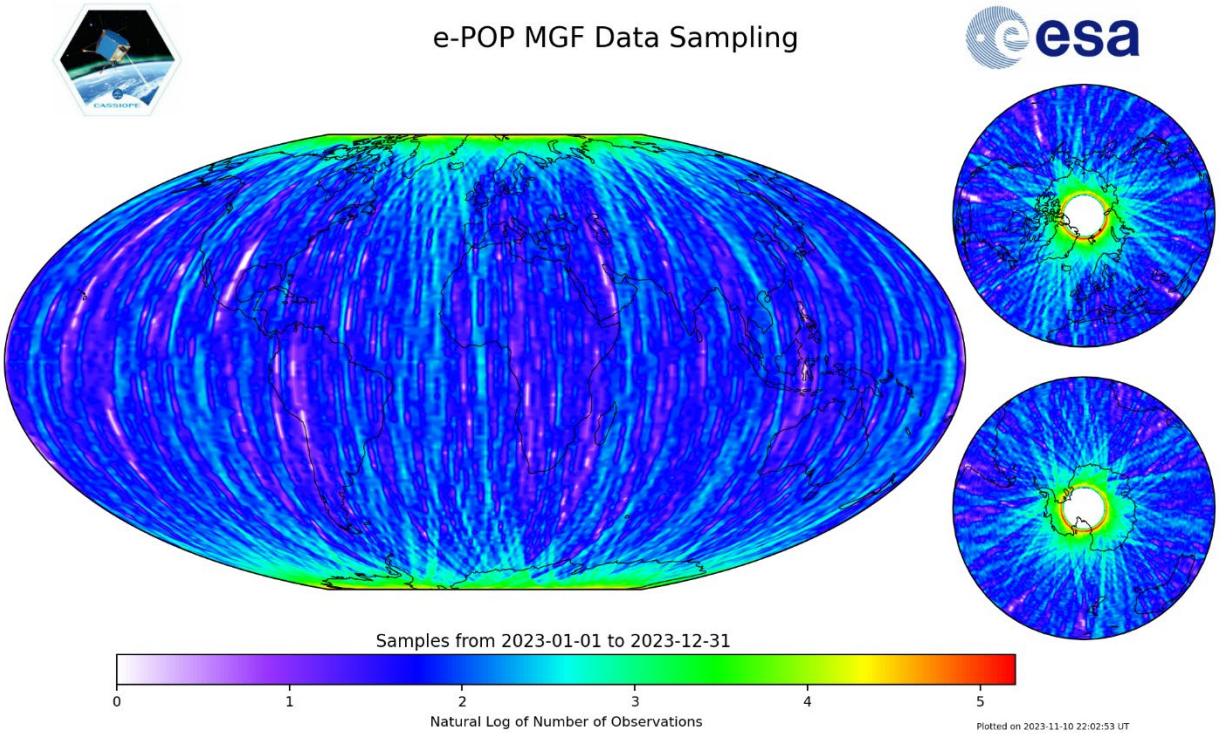

Figure 102: MGF Data Sampling for 2023

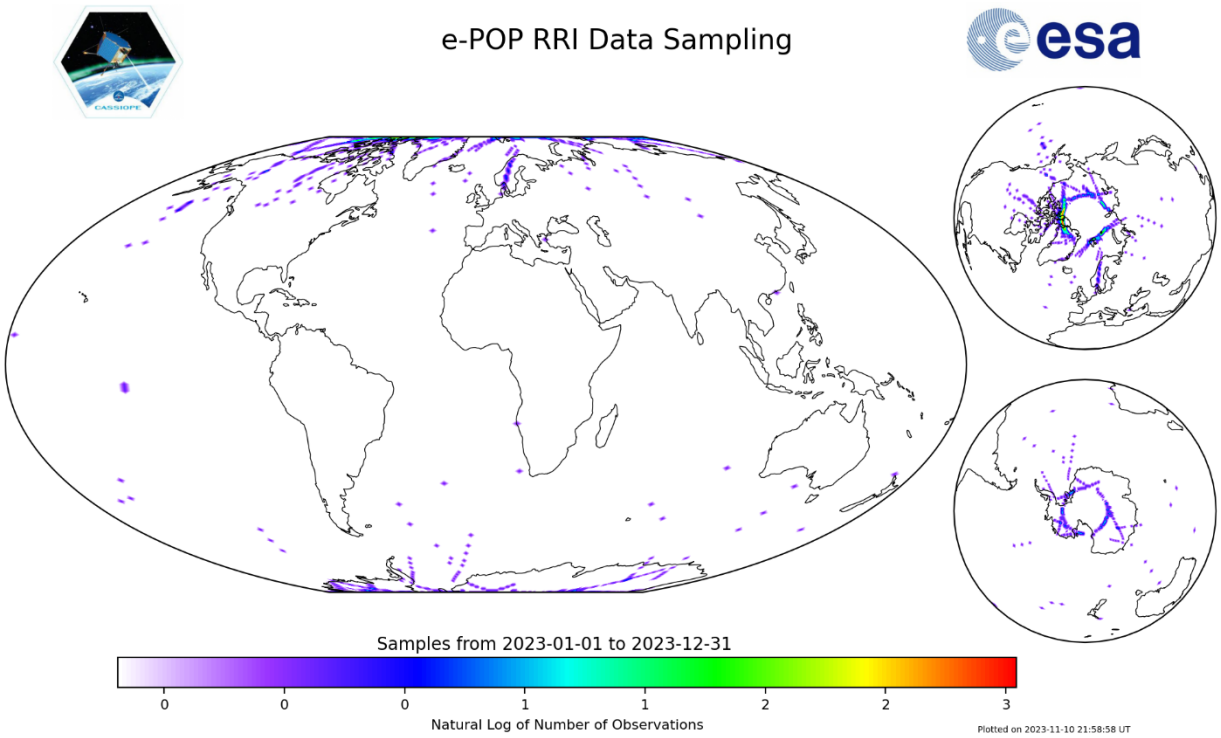

Figure 103: RRI Data Sampling for 2023

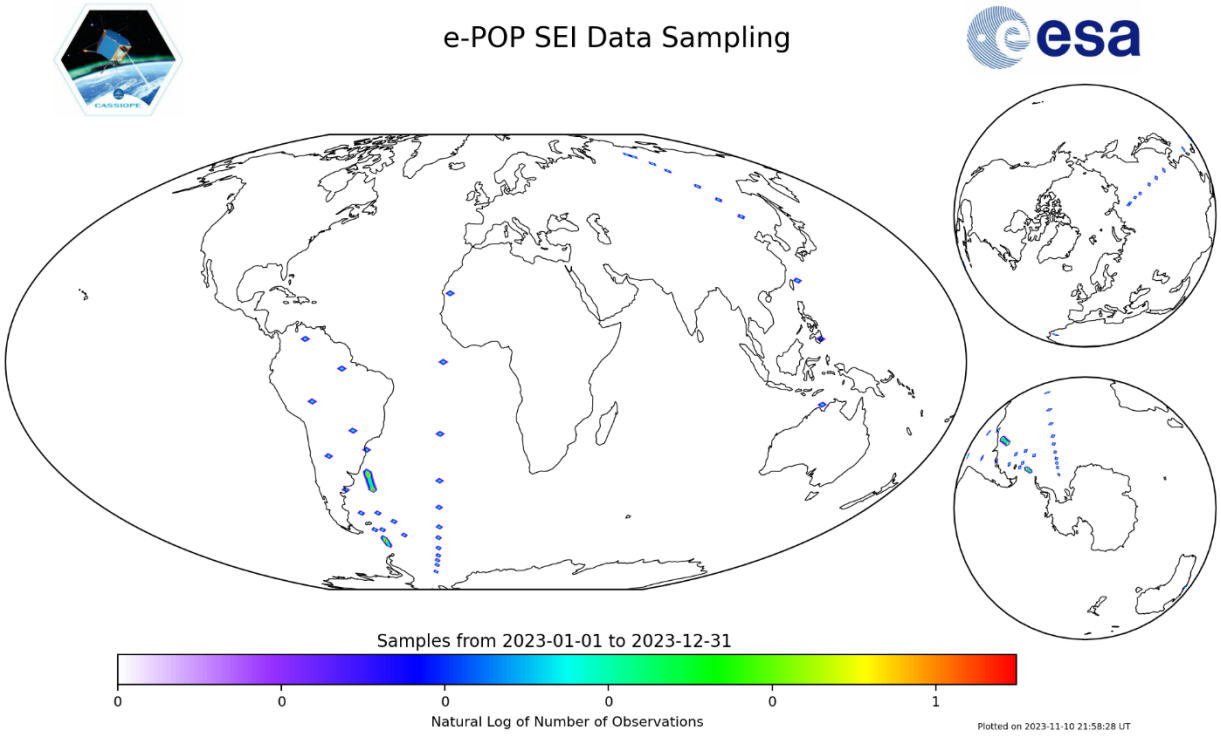

Figure 104: SEI Data Sampling for 2023

5 ANOMALIES

5.1 BUS ANOMALIES

5.1.1 CASSIOPE/Swarm-E Central Processing Unit (CPU) Reboots

A satellite in orbit that reaches above 1000 km altitude is subject to increased rates of high-energy radiation from Earth's inner radiation belts. This radiation is particularly strong in the South Atlantic Anomaly (SAA) where the weaker intrinsic magnetic field allows the particles to penetrate deeper into the Earth's atmosphere. Single event upsets related to high energy particle radiation occurred on CASSIOPE/Swarm-E from time to time, causing a CPU reset and disrupting regular operations. In the event of a CPU reset, all volatile memory is reset, housekeeping and science data is lost, and the spacecraft command timeline is replaced with the copy hard coded into flight software at launch. Thirty-one CPU resets were recorded over the course of the mission, listed in Table 6. Figure 105 shows the reset locations color-coded by the altitude of the spacecraft at the time of the reset, clearly indicating the influence of the SAA at high altitude.

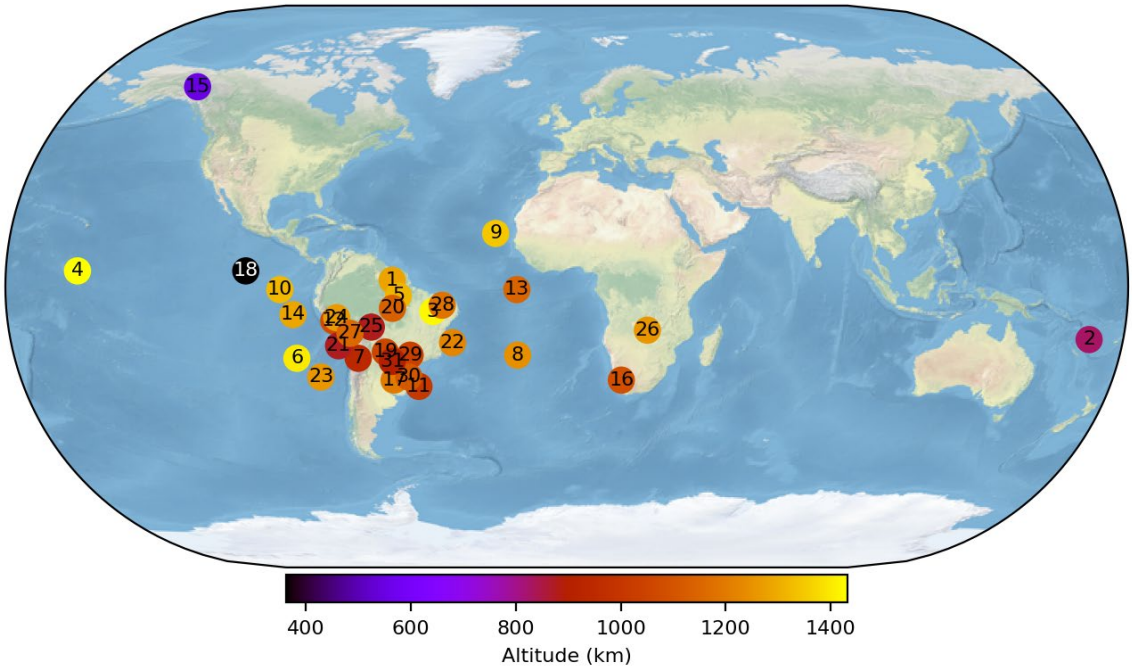

Figure 105: Map of all CASSIOPE/Swarm-E CPU resets, colored by S/C altitude at the time of reset. See Table 6 for the list of times associated with these resets.

Reset Number	Date/Time (UTC)	Latitude (°)	Longitude (°)	Altitude (km)
1	2013-10-08 22:58:55	2.0	-56.1	1257.5
2	2014-05-11 03:30:18	-16.5	168.5	844.3
3	2014-06-04 14:27:00	-8.0	-42.8	1426.2
4	2014-08-12 01:01:29	4.8	-157.1	1431.9

5	2014-12-03 03:12:49	-3.4	-53.8	1331.7
6	2015-02-23 06:17:55	-23.4	-88.4	1402.2
7	2015-11-24 04:48:40	-23.2	-67.9	944.2
8	2015-12-07 23:28:56	-22.2	-15.8	1246.0
9	2015-12-31 20:18:49	16.8	-22.7	1347.8
10	2016-01-04 00:41:24	-1.1	-91.8	1320.1
11	2016-03-28 10:53:58	-31.9	-49.3	1010.9
12	2016-05-18 05:31:50	-11.1	-74.9	1075.0
13	2016-07-20 04:59:56	-0.6	-15.7	1147.7
14	2017-07-21 08:28:24	-8.7	-88.1	1288.7
15	2017-08-24 18:04:01	64.2	-139.2	552.2
16	2017-12-16 17:49:09	-30.0	18.4	1088.0
17	2018-09-21 09:14:07	-30.1	-56.9	1198.6
18	2018-09-25 23:22:14	4.8	-102.7	358.3
19	2018-12-25 20:19:50	-20.8	-58.5	1056.8
20	2019-02-03 14:37:54	-6.5	-56.0	1128.5
21	2019-02-10 14:59:53	-19.1	-73.6	875.0
22	2019-11-23 09:29:57	-18.0	-36.8	1227.8
23	2020-01-10 18:24:59	-29.0	-80.8	1259.1
24	2020-01-27 15:24:54	-9.5	-73.5	1264.5
25	2020-08-28 21:30:03	-12.5	-63.4	879.5
26	2020-12-07 01:57:27	-14.4	25.8	1260.3
27	2021-02-06 12:19:42	-14.7	-69.9	1157.7
28	2021-02-07 10:05:55	-6.4	-39.7	1184.1
29	2021-07-22 00:14:01	-21.9	-51.4	1042.1
30	2021-09-07 06:26:20	-29.2	-51.9	1110.6
31	2023-06-12 14:51:10	-24.4	-57.2	895.5

Table 6: CASSIOPE/Swarm-E CPU reset list.

5.1.2 Bus Solar Array Anti-Ram-Minus Thermistor Error

The solar array thermistor monitoring the anti-ram-minus panel, known as TS10 in the CASSIOPE/Swarm-E telemetry, intermittently delivered unrealistically high temperature values (> 140 °C) since April 30, 2014. This intermittent behavior occurred throughout the mission. Operational alarms related to high temperature values from TS10 were silenced during operations.

5.1.3 Bus Solar Array Top Thermistor Error

The solar array thermistor monitoring the top solar panel, known as TS2 in the CASSIOPE/Swarm-E telemetry, intermittently delivered unrealistically high temperature values (> 100 °C), starting on September 19, 2016. This intermittent behavior occurred throughout the mission. Operational alarms related to high temperature values from TS2 were silenced during operations.

5.1.4 Bus Solar Array Ram-Plus Thermistor Error

The solar array thermistor monitoring the ram-plus panel, known as TS3 in the CASSIOPE/Swarm-E telemetry, intermittently delivered unrealistically high temperature values (> 216,000 °C), starting on August 7, 2015. This intermittent behavior occurred throughout the mission. Operational alarms related to high temperature values from TS3 were silenced during operations.

5.1.5 Severe Load Shed Event of 2015-02-24

On February 23, 2015, at 06:17 UTC, CASSIOPE/Swarm-E suffered a single event upset that resulted in a CPU reset. During a recovery contact near 17:28 UTC on February 24, the spacecraft was commanded to transition from the sun-pointing thermal mode of the reboot to an operational thermal mode. This was done without disabling the health and safety 'one-shot' software check, as was required, resulting in a condition where the thermal mode could not be altered by the health and safety system in the event of an out-of-specification condition. The operational thermal mode warmed the spacecraft from -30 ^{o}C over the course of a few hours, but when the power reached a critically low value the health and safety system was unable to change the thermal mode due to the one-shot override. As a result, the heaters were left on and the power system was drained to nearly zero and the flight computer was turned off along with all other bus units and payloads, leaving only the low-level Unit Manager running. Over the course of the next nine days, a complex recovery operation was conducted to get the spacecraft flight computer turned back on, and all units and payloads returned to regular operations. No lasting effects were caused by this outage other than a lack of science and bus telemetry data for the affected period.

5.1.6 Reaction Wheel Failures

5.1.6.1 Wheel 4 Failure

At approximately 00:40:13 UTC on Aug 12, 2016, all CASSIOPE/Swarm-E reaction wheels suddenly ramped from the nominal +/-100 rad/s down to zero (see Figure 106). After this event, wheels 1, 2, and 3 continued to operate while wheel 4 remained stopped near zero rads/s. The flight software wheel speed references remained in place with a desired speed of 100 rad/s but were ignored by flight software. The wheel 4 temperature before, during, and after the event was nominal, between 3^{o} and 7^{o} C. Attempts to spin-up the wheel in the days following failed to get it running again, and the spacecraft continued with three operating wheels.

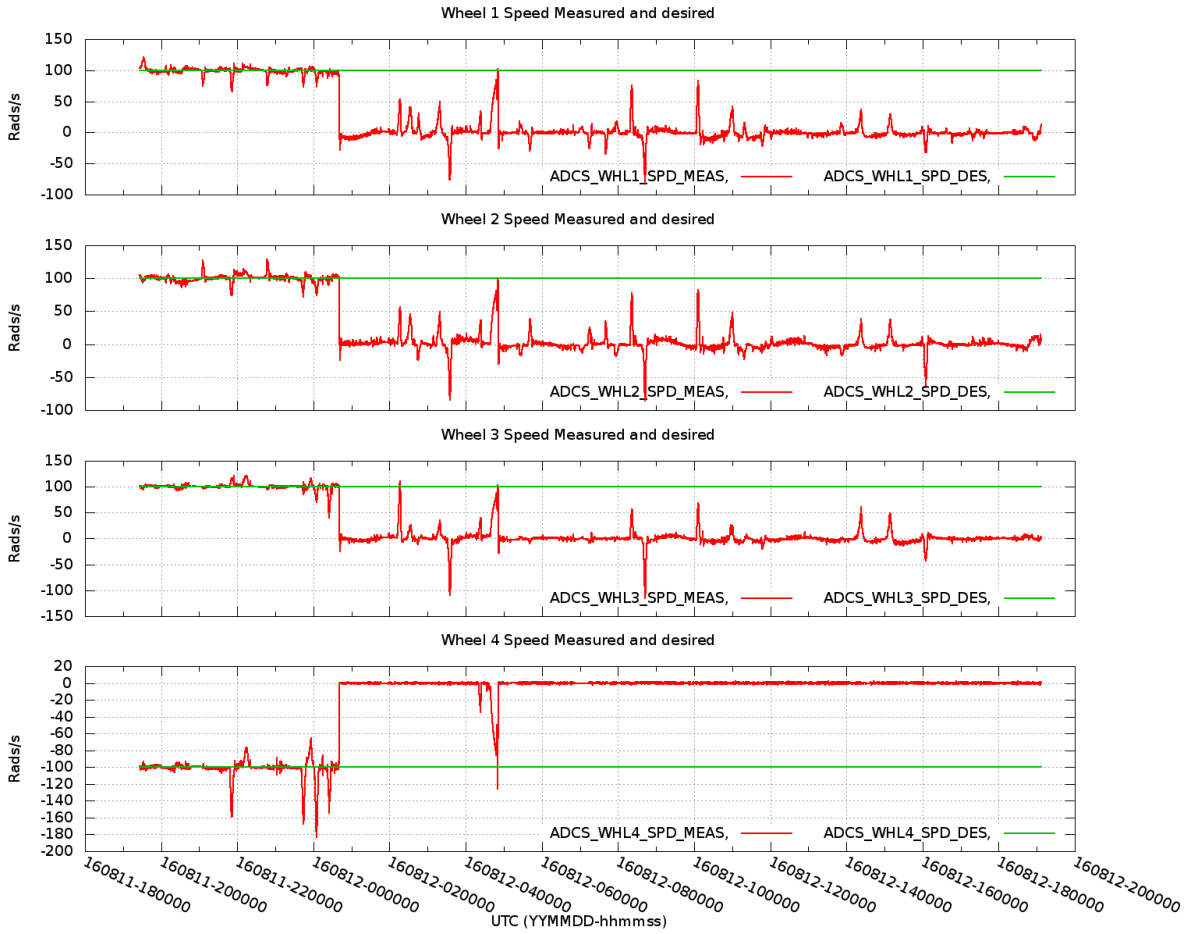

Figure 106: CASSIOPE/Swarm-E wheel speeds for wheels 1-4 (panels top-bottom). Green lines are the desired speeds, red lines are the measured speeds.

The default operational speed of the wheels changed from 100 rad/s before the failure to 0 rads/s after the failure. With three operational wheels, the bus flight software forces the default wheel speed to 0 rads/s, presumably due to difficulty in controlling momentum build up in the wheels when one wheel is not operational. This change affected the magnetic signature of the wheels and can be seen in magnetic sonograms of MGF data after the failure.

5.1.6.2 Wheel 1 Failure

Near 12:27 UTC on February 27, 2021, reaction wheel #1 on CASSIOPE/Swarm-E was attempting to spin down and switch its rotation direction when it became stuck. As can be seen in Figure 107Figure 107: Top panel: Wheel 1 commanded (green), wheel 1 measured (pink), wheel 2 commanded (blue), and wheel 2 measured (red) speeds. Bottom panel: Wheel 1 current draw (green), and wheel 2 current draw (pink). below, both wheel 1 and wheel 2 were operating in a similar fashion, with wheel 1 sticking when it crossed the zero-speed threshold.

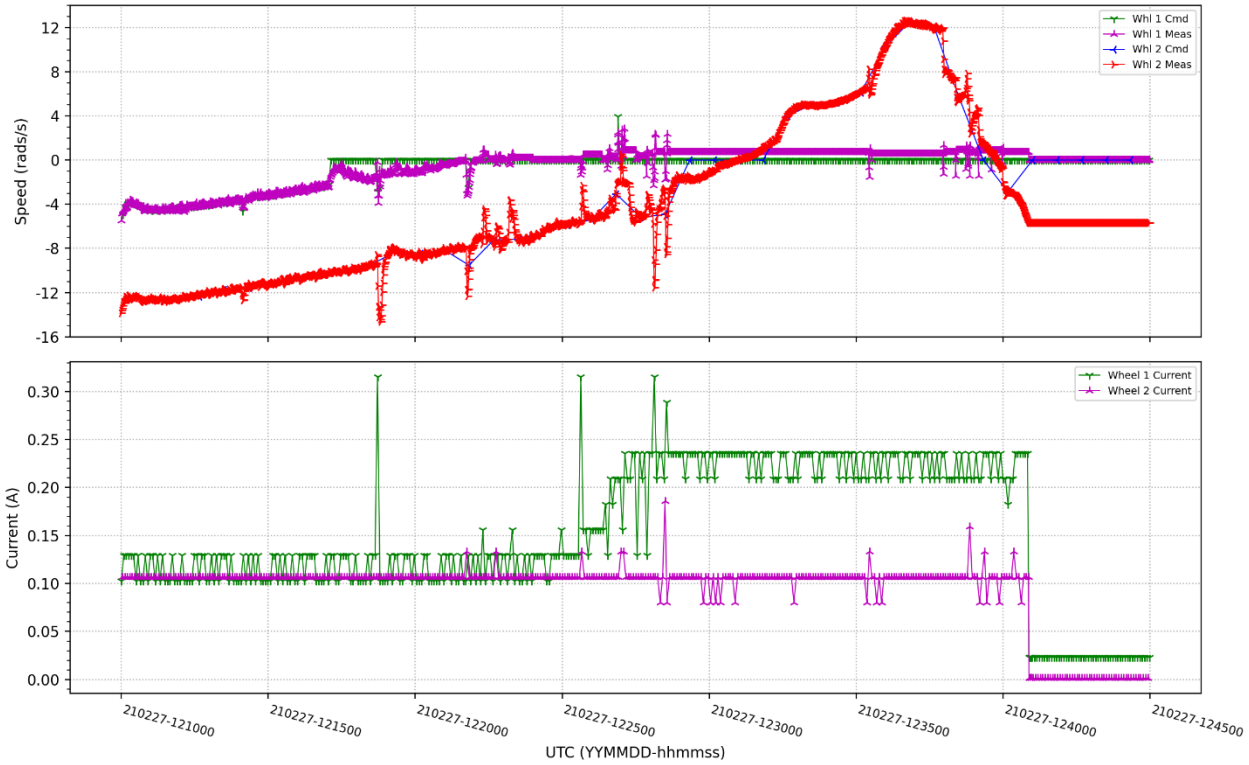

Figure 107: Top panel: Wheel 1 commanded (green), wheel 1 measured (pink), wheel 2 commanded (blue), and wheel 2 measured (red) speeds. Bottom panel: Wheel 1 current draw (green), and wheel 2 current draw (pink).

The attitude determination and control system (ADCS) recognized that wheel 1 was sticking and increased the current to the wheel just after 12:25:00. After 15 minutes of unsuccessfully spinning up wheel 1, the ADCS placed the spacecraft in safe-hold mode and powered off all wheels.

On subsequent spacecraft ground contact sessions, recovery attempts were initiated whereby all four wheels were powered on and sent commands to spin up. Wheel 1 did not spin up. Figure 2 shows two such attempts, where it can be seen that power is applied to wheel 1, it is commanded to spin at 20 rads/s, but it does not change its speed from ~0 rads/s (note that the measured speed of a wheel is misreported before it is asked to spin-up – the values of < -100 rads/s in Figure 2 are fictitious). The current is increased by the ADCS to push the wheel to spin, but it fails.

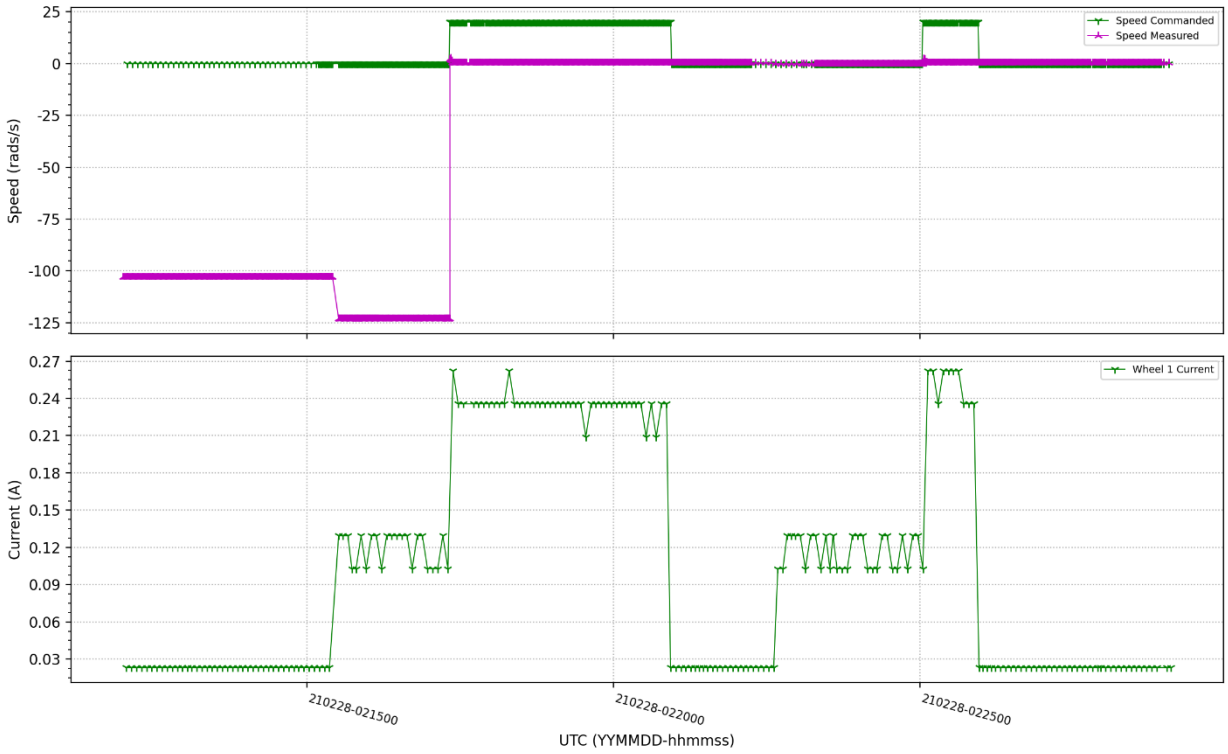

Figure 108: Unsuccessful wheel 1 spin-up attempts on February 28 at 02:15 UT

The behavior of wheel 1 after the incident matches that of wheel 4, which failed in August 2016. Each wheel appears to have had a catastrophic failure of the bearings, causing them to seize.

5.1.6.3 Wheel 3 Failure

The third wheel to fail on CASSIOPE/Swarm-E was Wheel 3, which stopped on December 17, 2021 near 06:05 UTC. This failure resulted in a complete shutdown of the wheel suite, since the operation of a single wheel has no practical purpose, leaving the spacecraft in its safe hold mode. Safe hold mode uses the torque rods to point the main solar panel at the sun, spinning the spacecraft about its z-axis at one degree per second. After this event, routine science operations of CASSIOPE/Swarm-E came to an end.

5.1.7 Extended Downtime Event – July 2019

On July 26, 2019, at 23:32:45 UTC, CASSIOPE/Swarm-E was scheduled to transition to its 'Nadir' attitude from its 'RRI_Nadir' attitude. During the transition, the star trackers became blinded causing a loss of attitude data, resulting in a slow, uncontrolled spin. After a number of minutes, the attitude control system failed to gain control, and executed an autotransition to sun acquisition mode. The autotransition disables command timelines, turns off the reaction wheels, and uses the torque rods to point the main solar panel at the sun.

The next day, at 17:27:22 UTC, an attempt to recover the spacecraft from the autotransition was made. At the time the reaction wheels were energized for the recovery, the spacecraft was still spinning, leading to a high-momentum alarm and autotransition just under an hour later. The spacecraft was left for a number of hours to allow it to de-spin automatically using the torque rods.

On July 29 at 15:27:33 UTC the recovery was continued, and the wheels were successfully turned on and activated.

On July 30 at 01:45:31 UTC, during the final steps in the recovery phase, a commanding error was made that caused an overwrite of a critical area of memory that rendered the data collection buffers unusable, meaning that both back orbit bus telemetry and science data were not being written to memory. After consulting the bus manufacturer for a solution, a fix was implemented on August 2 at 02:05 UTC involving a soft CPU reset, allowing normal operations to resume. This event resulted in loss of science data for a period of close to seven days.

5.1.8 Loss of Star Sensor Attitude Solutions

CASSIOPE/Swarm-E uses the Danish Technical University's Micro Advanced Stellar Compass (μ-ASC) star sensor. These units use CCD devices to image star fields for calculation of an accurate attitude solution. When the noise on a given star sensor CCD exceeds a certain threshold, the star sensor is unable to distinguish stars from noise and an attitude solution cannot be found.

For CASSIOPE/Swarm-E, there are three factors that increased the noise profile of the μ-ASC CCDs:

1) The star sensor CCD noise profile is temperature dependent – the higher the star sensor temperature, the higher the noise profile. Short-term temperature swings are dependent on both the orbit plane configuration and the spacecraft attitude.
2) The baseplate temperature of the star sensors increases with time throughout the mission, coupling with factor #1 above to increase overall CCD noise.
3) The noise floor is affected by the total radiation dose – the longer the unit is in space, the higher the radiation dose, the higher the noise floor.

Figure 109 shows the hourly-averaged validity flag for star sensor A (SSA) as a function of time and CCD temperature. At the start of the mission, good star sensor attitude solutions are found for temperatures over 10 ^{o}C, but as the mission progresses the threshold temperature decreases to closer to 5 ^{o}C. Figure 110 shows the same data for star sensor B (SSB).

The star sensor temperature is primarily affected by the satellite orientation with respect to the sun – depending on the orbital plane configuration and the attitude of the spacecraft, the star sensor is either in sunlight or in eclipse for long periods of time. As the orbit plane precesses, the star trackers alternate between being primarily sunlit or eclipsed, thus they each go through periods of high and low temperatures. On average, at least one star tracker was below the minimum temperature threshold to get reliable attitude solutions ~99% of the time. The remaining 1% of the time therefore represents occasions when neither star tracker is providing acceptable attitude solutions, leaving only the Coarse Sun Sensor information for attitude. These solutions have a very large uncertainty of 8^{o} in yaw, pitch, and roll. This was an ongoing issue throughout the mission.

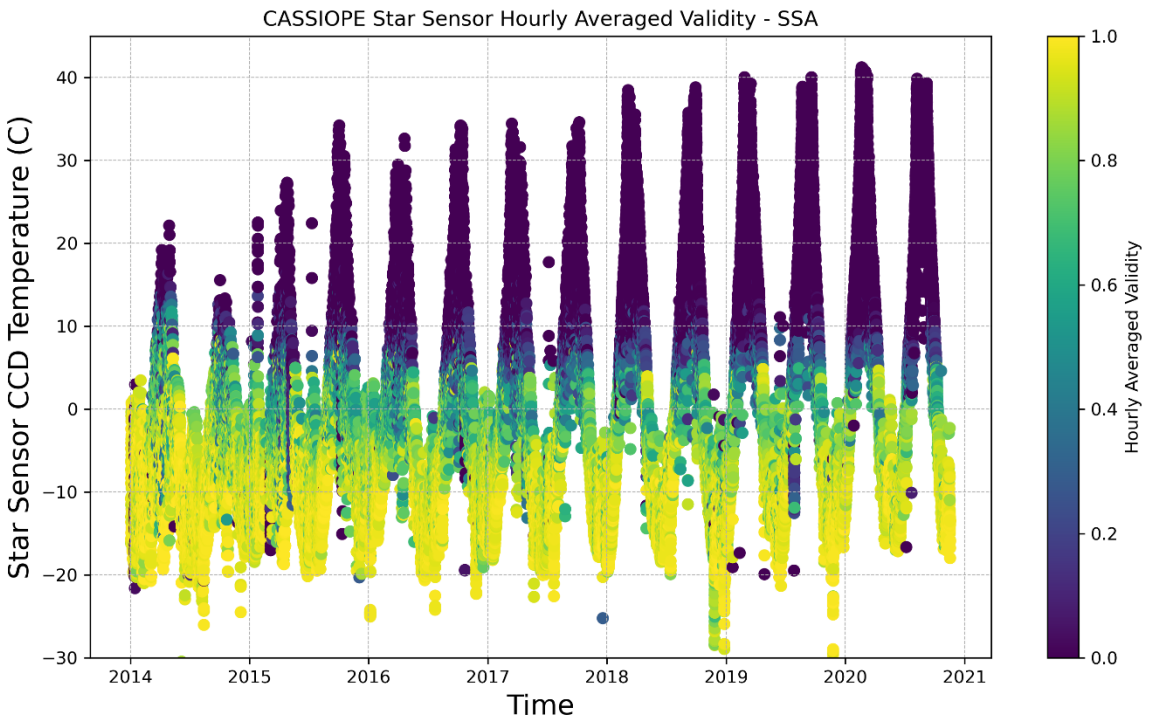

Figure 109: Star Sensor A hourly-averaged validity as a function of time and temperature

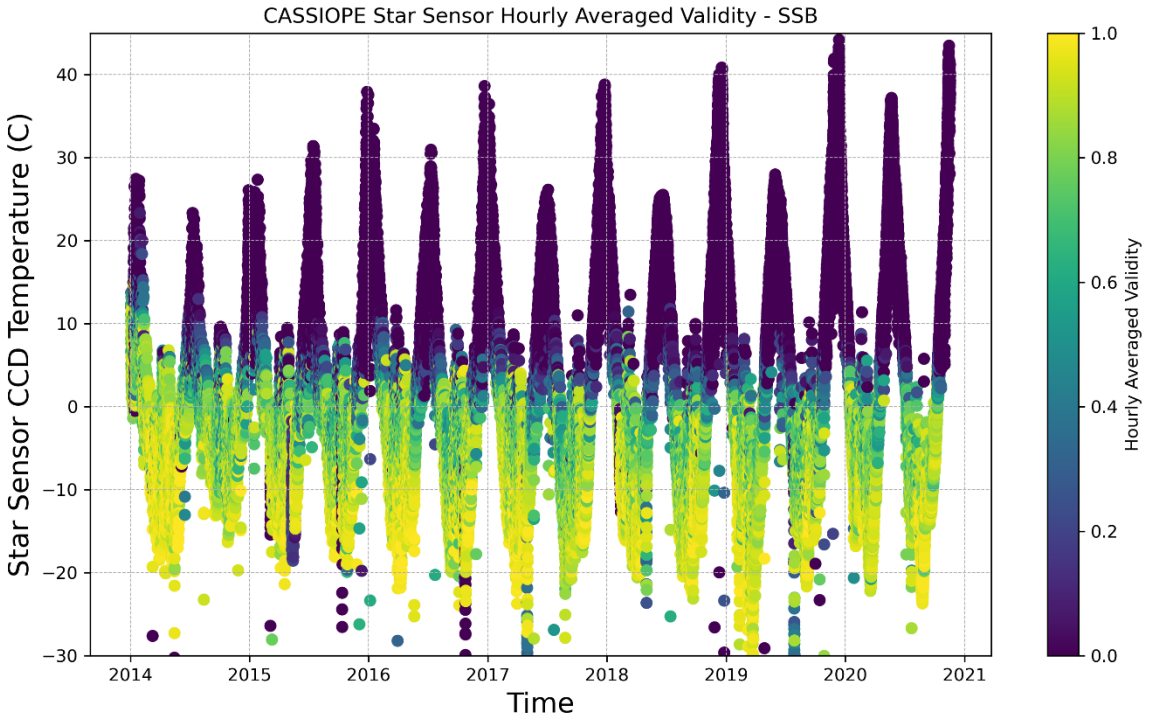

Figure 110: Star Sensor B hourly-averaged validity as a function of time and temperature

5.2 E-POP ANOMALIES

5.2.1 CERTO Antenna Deployment

The CERTO beacon antenna, being stowed at launch, was deployed on October 1, 2013. Figure 111 shows the antenna boom in its stowed state, Figure 112 shows the antenna fully deployed. The boom

Figure 111: CERTO antenna in its stowed position

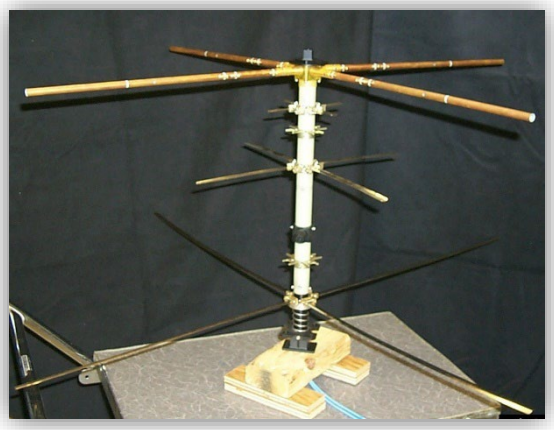

Figure 112: CERTO antenna in its deployed state

deployment is monitored by a potentiometer that has a value of 1.62 volts when the boom is stowed, and 0.97 volts when the boom is fully deployed. Values of the potentiometer during the boom deployment are shown in Figure 113. The final deployed value for the potentiometer after the CASSIOPE/Swarm-E commissioning phase was 0.997 volts, indicating that the CERTO boom deployed to an angle of 87.57 degrees, short of the expected 90 degree full-deployment angle. There is nothing to indicate that the antenna components themselves did not deploy as expected, however the pointing direction of the CERTO antenna must be considered when interpreting ground receiver results.

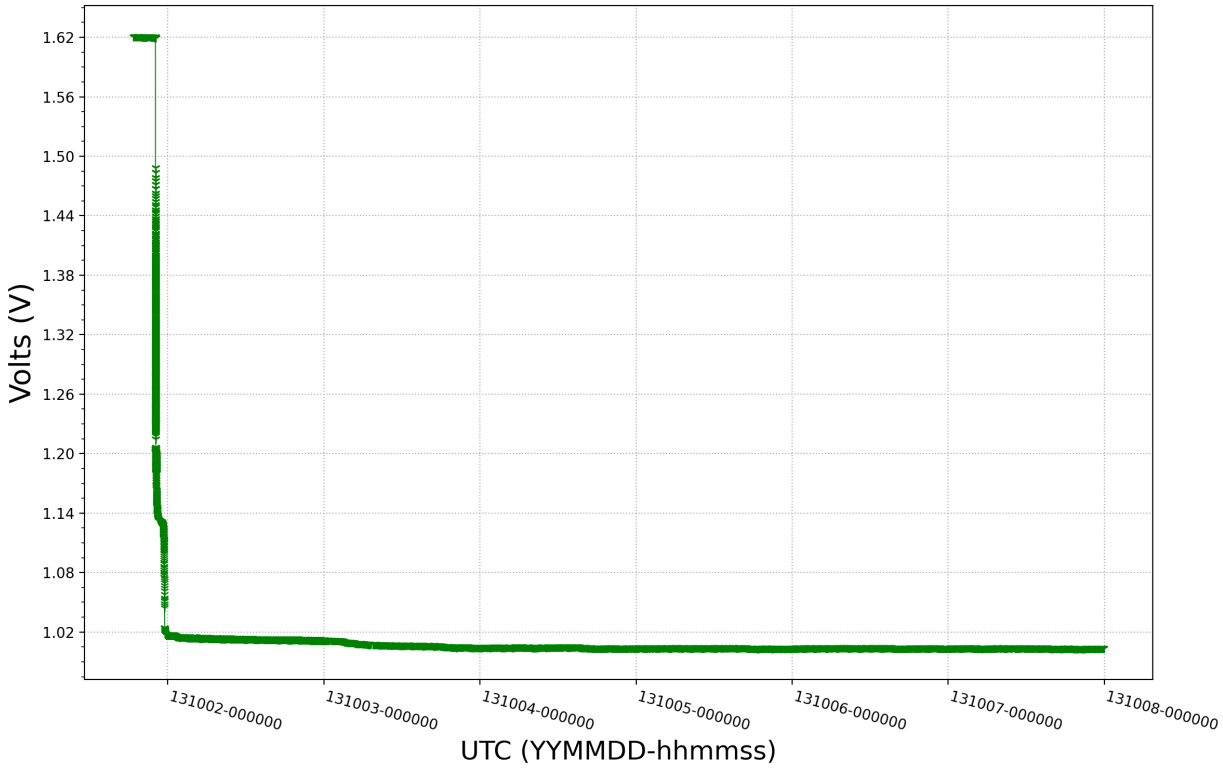

Figure 113: CERTO beacon antenna potentiometer values during boom deployment

5.2.2 Loss of Fine Pointing During MGF Data Collections

Science data collected by the MGF instrument on CASSIOPE/Swarm-E is viable only when the magnetic torque rods used for attitude control on the spacecraft are disabled. Disabling the torque rods is implemented in operations as a special attitude control mode that is activated prior to turning on MGF. On occasion, the attitude control system would fail to adequately obtain sufficient attitude knowledge from the star trackers while in this special mode, and autonomously fail over into the default attitude control mode so that control would not be in danger of being lost. These events are referred to as autotransitions, specifically an A6 autotransition in this case. When an A6 autotransition occurs, the MGF data is swamped by the magnetic signal from the torque rods for the remainder of the data collection session. Figure 114 shows an example from September 7, 2014, when an A6 autotransition affected the MGF science data at 11:16 UTC.

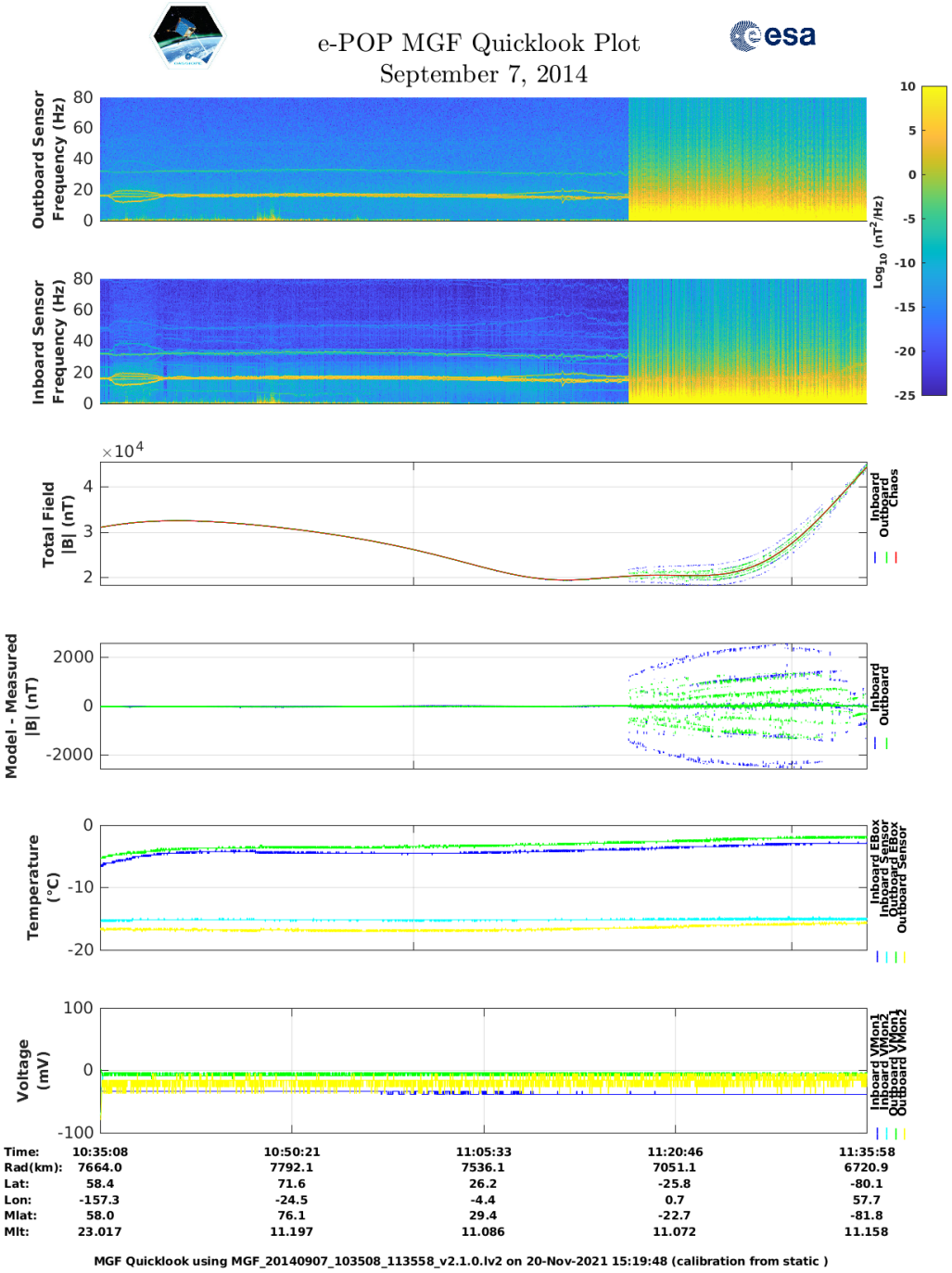

Figure 114: MGF Quicklook Plot of a session with an A6 autotransition at 11:16 UTC.

Table 7 lists all the A6 autotransitions that occurred during the routine operations phase of the CASSIOPE/Swarm-E mission.

A6 Transition Time (UTC)	A6 Transition Time (UTC)	A6 Transition Time (UTC)
2014-02-11 08:03:54	2018-01-02 00:09:29	2019-06-05 15:01:15
2014-02-12 11:03:54	2018-01-02 01:52:18	2019-07-09 19:22:22
2014-03-18 22:48:20	2018-01-24 08:02:03	2019-07-12 16:09:47

2014-05-15 08:06:38	2018-02-10 11:37:47	2019-07-15 16:27:14
2014-06-16 17:01:07	2018-02-10 20:03:26	2019-07-17 16:27:01
2014-06-17 04:48:42	2018-02-10 23:25:42	2019-07-19 17:31:30
2014-06-17 06:31:20	2018-02-11 04:29:06	2019-07-24 12:40:25
2014-09-01 14:00:08	2018-02-11 06:10:14	2019-07-26 23:31:58
2014-09-07 11:17:07	2018-02-11 07:51:22	2019-07-27 19:18:56
2014-09-09 11:08:33	2018-02-11 14:41:05	2019-07-28 08:29:29
2014-09-23 15:16:10	2018-02-11 19:39:16	2019-09-21 10:53:19
2014-09-26 15:01:48	2018-02-11 23:01:33	2019-09-25 12:35:21
2014-09-27 14:52:40	2018-02-12 00:42:40	2019-10-01 21:42:34
2014-11-07 09:07:32	2018-02-12 04:07:01	2019-10-25 09:48:38
2014-11-10 19:52:10	2018-02-12 05:46:04	2020-01-17 07:44:29
2014-11-14 03:39:22	2018-02-12 07:27:12	2020-02-04 02:43:22
2014-11-18 10:45:14	2018-02-12 10:49:27	2020-03-28 15:55:21
2014-11-19 19:05:18	2018-02-12 14:14:44	2020-03-29 15:27:19
2014-11-20 18:59:21	2018-02-12 19:15:06	2020-04-02 23:07:14
2014-11-23 18:41:19	2018-03-31 14:13:20	2020-04-08 01:50:07
2014-12-24 21:59:17	2018-03-31 22:39:01	2020-04-21 18:20:53
2014-12-24 23:44:02	2018-04-01 05:25:47	2020-06-05 03:01:16
2015-03-11 21:48:39	2018-05-18 17:42:43	2020-06-25 16:29:55
2015-03-12 12:26:49	2018-07-19 09:17:53	2020-06-28 04:55:14
2015-05-12 22:08:30	2018-07-19 10:59:43	2020-06-29 19:18:13
2015-10-09 18:00:21	2018-08-13 20:44:02	2020-07-05 14:44:49
2016-03-17 08:27:43	2018-11-20 15:27:16	2020-07-07 05:23:28
2016-10-15 21:03:54	2018-11-25 16:17:31	2020-07-10 01:17:03
2016-10-16 00:20:47	2018-11-26 17:11:26	2020-10-09 03:51:39
2016-10-16 08:47:20	2018-12-22 21:03:13	2020-10-21 09:33:21
2016-10-23 20:14:56	2019-01-20 20:13:48	2020-12-24 10:35:16
2016-10-24 01:19:12	2019-01-20 21:54:47	2021-01-17 05:13:09
2016-10-24 06:23:30	2019-01-20 23:35:45	2021-01-19 04:09:53
2017-07-30 09:27:42	2019-01-21 01:18:36	2021-01-19 05:52:44
2017-08-29 15:56:58	2019-01-21 02:57:42	2021-02-01 02:35:19
2017-09-09 03:23:51	2019-03-20 18:19:12	2021-02-03 21:41:20
2017-09-09 05:01:48	2019-03-21 04:26:44	2021-02-08 17:23:51
2017-11-14 19:46:48	2019-05-11 01:28:18	2021-09-20 17:11:04
2018-01-01 14:11:59	2019-06-04 15:27:19	2021-09-24 15:42:39

Table 7: A6 Autotransition Times in UTC

5.2.3 FAI Visual Camera Blinding

Prior to launch it was anticipated that the FAI Visible Camera would have a low signal-to-noise ratio, due to the very small bandwidth (2 nm) of the 630 nm filter in its optical chain. During the commissioning phase of the mission, the images from the camera had a sufficiently high signal-to-noise ratio for

scientific use. However, unlike the Near-infrared Camera and despite the two cameras sharing the same CCD manufacturer and model, the dark noise signal on the Visible Camera rose much more quickly than the Near-infrared Camera, to the point that on November 30, 2016 the Visible Camera was taken out of regular service due to very poor signal-to-noise ratios. Figure 115 compares images of the limb with aurora from the Visible Camera early in the mission (left image) and just prior to its shutdown in 2016 (right image). The image from later in the mission is clearly suffering from a drastic reduction in the signal-to-noise ratio.

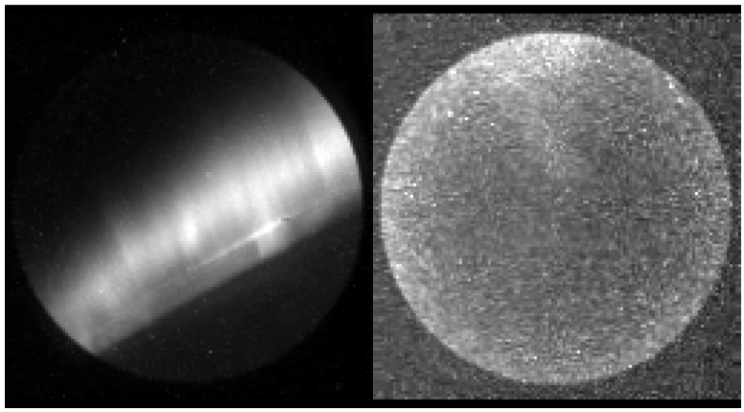

Figure 115: FAI Visible Camera images from Nov 09, 2013 (left) and Oct 08, 2016 (right)

5.2.4 Loss of the GAP GPS-1 Receiver

An abnormal current spike occurred in the GAP electronics box on September 16, 2018, at 07:50:53 UTC (see Figure 116), corresponding exactly with the loss of data packet reception from the GAP GPS-1 receiver. In the days following the event, attempts to communicate with the GPS-1 receiver were unsuccessful, even though the GAP current draw indicated that the receiver was powering up. A full reset of the GPS-1 receiver software was also attempted, but there was no response received from the unit. Operations with GPS-1 were abandoned, and the GAP GPS-3 receiver was activated from its cold spare status into routine operations to replace the failed GPS-1 receiver on October 18, 2018.

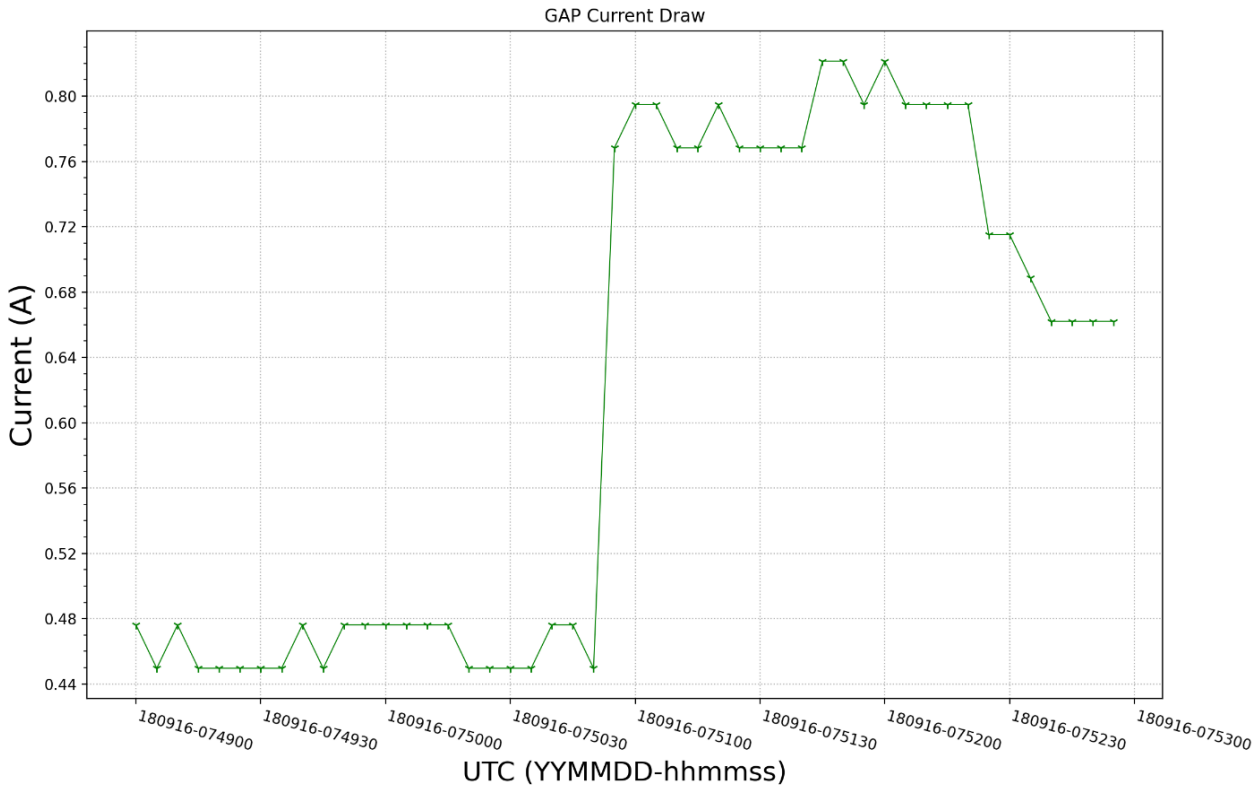

Figure 116: GAP current draw at the time of the loss of the GAP GPS-1 receiver

5.2.5 Loss of GAP GPS-4 Receiver Data

The GAP GPS-4 receiver failed to send data packets at start up on November 1, 2018 at 08:05:41 UTC. The prior operational pass was nominal. No current draw abnormalities were detected during the power-up sequence, or during the prior operation. A factory reset command was issued to the unit on December 13, 2018, at which point the unit powered on and began to transmit data in its default operating mode. Routine operations were resumed after the default operating parameters for GPS receiver 4 were set in the GAP onboard memory.

A second, permanent loss of the GAP GPS-4 data occurred in 2022. When the third reaction wheel on CASSIOPE failed in December of 2021, the spacecraft was put into a stable 1 deg/sec spin about its z-axis. In this mode, the GPS-4 receiver is not able to stare at the limb and watch as GPS satellites set over the horizon. For this reason, the receiver was not powered on for nearly two months. When an attempt was made to operate the receiver in February 2022, it failed to send data to the spacecraft. Numerous attempts were made to communicate with the receiver and get it operational once again, but no commands were successful and the receiver was declared dead on February 22, 2022.

5.2.6 GAP EEPROM Failure

Each e-POP instrument is equipped with at least two copies of flight software on electronically erasable programmable read-only memory (EEPROM), for redundancy in case of failure of the primary image. For GAP, there is an upper and a lower EEPROM, each containing one copy of flight software. Nominally, the

GAP instrument was booted from the lower EEPROM. On February 23, 2021, upon power-up, the GAP instrument failed to boot and was unresponsive. The instrument was power-cycled several times but continued to be unresponsive, despite drawing power. When an attempt was made to boot from the upper EEPROM, the instrument booted as normal and provided nominal data packets and command responses. The conclusion is that the lower EEPROM suffered a single event upset and no longer contains a valid flight software image. Routine operations from February 24th, 2021, and onward made use of the upper EEPROM image on GAP.

5.2.7 MGF Instrument Operational Deficiencies

Shortly after launch in 2013, analysis of the MGF data showed two deficiencies in the MGF operation. The first, deemed a moderate deficiency, was an unintended timing variation between when the magnetic feedback to the sensor was updated and when the next sample was taken. This caused unpredictable ring transients to occur as the MGF tracked the local magnetic field. Although the DC field was measured as expected, these transients significantly polluted the active component performance of the instrument and, due the timing variation, were very difficult to remove in post-processing. To solve this issue, a patch to the MGF flight software was proposed. Figure 117 below shows overplotted sequences of Analog to Digital converter values around a step in digital feedback using the original firmware (left panel) and the new firmware (right panel).

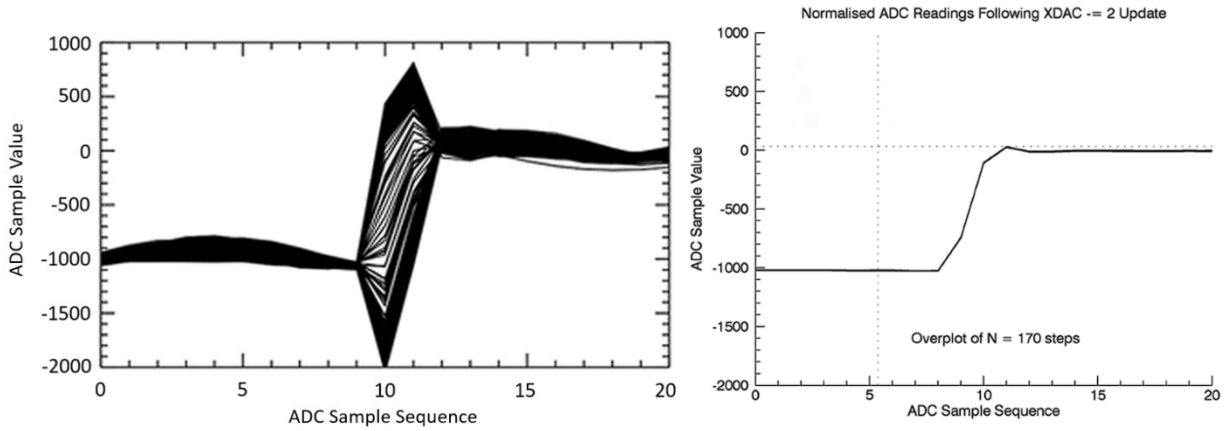

Figure 117: Transient behavior in the MGF data using (left) the original firmware and (right) the updated firmware.

The second deficiency, deemed minor, related to the synchronisation between the two magnetometers, such that there was an unpredictable offset between the two at power-up. This could have been removed in post-processing, but a flight software fix was chosen as the better solution since it was being employed for the ring transient issue noted above.

Testing was performed on the MGF engineering model at the University of Alberta in early 2014, allowing for a new flight software image to be developed that fixed the above noted timing issues. The new flight software, version 1.3.0, was verified and subsequently burned to the inboard magnetometer card on April 10, 2014. The outboard card was updated on April 22, 2014, after data from the inboard card was confirmed to be nominal and free from timing deficiencies.

5.2.8 NMS Science Data Values

The Neutral Mass Spectrometer (NMS) on e-POP was a first-generation instrument developed by the Japan Aerospace Exploration Agency (JAXA), intended to measure neutral mass composition and 2-D velocity distributions at e-POP altitudes. The instrument went through full assembly, integration, and testing procedures prior to launch, performing well in all vacuum tests.

When operated on-orbit, however, the data values returned from the instrument did not match the profiles seen on the ground. The particle count rates are much higher than expected, indicating that neutral particles are being measured without having the ionisation circuitry enabled. There is no conclusive evidence pointing to why this is the case, but it has been suggested by the NMS principal investigator that ionisation of excited neutral particles is the most probable explanation. The anomaly has not been reproduced on the ground, leaving the data in an uncalibrated state and unsuitable for scientific investigation.

5.2.9 Loss of the SEI High Voltage Power Supply

The SEI instrument relies on a high voltage power supply (HVPS) to detect ions and electrons that pass through its hemispherical electrostatic analyzer and land on the microchannel plate. Since early in the mission, the setting and monitoring of the HVPS voltages was erratic, but workable settings were found through trial and error. Since the absolute values of the HVPS voltages are not required for ion velocity and temperature calculations this did not pose a problem for interpretation of the data. Beginning in May of 2015, however, there were increasing signs that the high voltages were slowly dropping away, and eventually SEI recorded little to no signal in most passes. Operations with the HVPS enabled on SEI ended in October of 2016. Data acquired with the HVPS off can be used to measure cosmic ray abundance, since the SEI CCD is sensitive to these high energy particles without the HVPS operating. This mode was utilized in the years after the HVPS failure.

6 DATA PRODUCTS

The processed data products for the Swarm-E/CASSIOPE mission are shown in Table 8. A full description including contents and data formats can be found at https://epop.phys.ucalgary.ca/data-handbook/.

System	Data Product	Description
Spacecraft	Orbit Determination SP3	GPS-derived spacecraft position and velocity data in the International Terrestrial Reference Frame (ITRF) geographic Cartesian coordinate system, formatted in the National Geodetic Survey SP3 format. This is a mission-level product with an error estimate of ~5 meters on the position values.
	Attitude Quaternions	Daily CASSIOPE/Swarm-E attitude quaternions in CDF format.
	Ephemeris Text File	Spacecraft position and attitude information derived from the Orbit Determination SP3 and Attitude Quaternion products.
	Bus Telemetry CDF	Listing of various spacecraft housekeeping telemetry values (voltages, temperatures, etc.) in CDF format.
	Orbit Count File	Text file listing each orbit number, start time, and longitude at orbit start.

e-POP Payload	Quick Look Plot	A plot of the daily e-POP payload data availability
	Data Availability	A text file listing of the daily e-POP payload data availability
	Swarm Conjunction List	Listing of each time when CASSIOPE/Swarm-E was within 400km of any of Swarm-A/B/C, and there is e-POP data available.
CERTO	Quick Look Plot	Plot showing location, operating mode, and current draw of CERTO for each turn-on session.
	Total Electron Content (TEC)	Data files containing the total electron content for each pass as determined from receiver data taken during CERTO transmissions.
	TEC Quick Look Plot	Plots of the CERTO TEC data.
MGF	Summary Plot	Plot of the magnetic field components as measured by the inboard and outboard sensors of MGF.
	Quick Look Plot	Plot containing MGF voltage monitors, temperatures, magnetic field residuals, total magnetic field, and power spectrograms of the magnetic field.
	Lv1b High-Rate CDF	On-orbit calibrated 160 sample per second magnetic field data from MGF, in CDF format, one per day. Data files have similar structure to those of the main Swarm mission.
	Lv1b Low-Rate CDF	Daily 1 Hz magnetic field data from MGF. Data is on-orbit calibrated and in a similar format to those of the main Swarm mission.
	Residuals Plot	Plot of the deltas between the MGF sensors and the CHAOS model for each turn-on session of MGF.
FAI	Summary Plot	Keogram-style plot of the FAI imagery for each turn-on session, including a map with the FAI field of view projection.
	Quick Look Plot	Video of the full FAI image sequence for each turn-on session. Plots include a map with the satellite trajectory and the FAI field of view.
	Lv1 HDF5 Images	Corrected FAI image data in binary (HDF5) format, preserving the 16-bit depth of the images
	Lv1 PNG Images	Corrected FAI image data in 8-bit PNG format. Images are color-scaled so that the top 0.1% of the pixels appear white.
GAP	Quick Look Plot	Daily plot containing time and location of the GPS data, number of packets from each GAP GPS receiver, and type of GPS messages received
	Lv1 Binary Data	Raw GPS messages from each GAP receiver in the native NovAtel binary format.
	Lv2 RINEX Data	GAP GPS receiver data in the Receiver Independent Exchange (RINEX) format. Data files are produced by the NovAtel *Convert* software that converts raw binary NovAtel GPS message data into the RINEX format.
	Line-of-Sight TEC	Line-of-sight (LOS) TEC between a given e-POP GPS receiver and any locked GPS satellite. The LOS-TEC product is calibrated and phase-levelled TEC, processed to account for

		cycle slips, high noise and multipath, half-cycle ambiguities, and outliers. Data is formatted to the NetCDF standard.
	Line-of-Sight TEC Plot	Interactive plot in html format of the LOS TEC data.
	Vertical TEC	Vertical TEC derived from the LOS-TEC data product, at 1 Hz. One file is produced per day and formatted to the NetCDF standard.
	Vertical TEC Plot	Interactive plot in html format of the vertical TEC data.
IRM	Summary Plot	The IRM summary plot contains five panels that show an energy-time spectrogram, a time-of-flight-time spectrogram, the sensor surface current, total counts per second on the IRM anode, and a map showing the location of the observations.
	Quick Look Plot	Video showing a plot of the IRM counts on the anode alongside a time-of-flight histogram for two inner dome voltage settings. Engineering housekeeping values are also displayed. There is one mp4 video for each turn-on session of IRM.
	Sensor Surface Current (SSC) HDF5 Data	The IRM SSC HDF5 file is generated for each IRM turn-on session and consists of the IRM sensor surface current time-series data coupled with spacecraft ephemeris information.
RRI	Quick Look Plot	The RRI quicklook plot includes voltage spectrograms for each RRI input channel, a plot of the spacecraft attitude, as well as a map showing the location of the measurements.
	Lv1 HDF5 Data	This level-1 product contains processed RRI antenna voltage values, in mV, alongside RRI housekeeping and settings data, and spacecraft ephemeris data. The files are in HDF5 format and are produced for each RRI turn-on session.

Table 8: CASSIOPE processed data products

7 PERSONNEL

7.1 MANAGEMENT PERSONNEL

CASSIOPE/Swarm-E has benefitted from consistent program management at both the University of Calgary and at ESA over the duration of the mission. Below is a list of managers, their titles, and years of service.

Name	Organization	Title	Years of Service with CASSIOPE/Swarm-E
Dr. Andrew W. Yau	University of Calgary	Mission Scientist	1997-Present
Gregory Enno	University of Calgary	Project Manager	1997-2019
Andrew Howarth	University of Calgary	Project Manager	2001-Present
Dr. Rune Floberghagen	European Space Agency	Mission Manager	2017-2019
Dr. Anja Strømme	European Space Agency	Mission Manager	2019-Present
Antonio de la Fuente	European Space Agency	Operations Manager	2017-Present

Table 9: CASSIOPE/Swarm-E management staff

7.2 Operations Personnel

Personnel at the University of Calgary that have been responsible for the day-to-day operations of the satellite including daily contact sessions, command table generation, attitude and power planning, data management, anomaly resolution, and more, are listed in the table below along with his/her respective years of service.

Name	Years of Service
Troy Kachor	2012-Present
Yi-Ching Chung	2012-2015
Jamie Roberts	2013-2018
Warren Holley	2018-Present
Stephanie Erion	2018-2020
Paige Rutledge	2019-Present

Table 10: CASSIOPE/Swarm-E satellite operators

7.3 Science Team

Prior to launch of the CASSIOPE satellite, a Science Team was assembled of members that would lead the analysis and data modeling assimilation efforts while the mission was active. In 2012, the Science Team consisted of the following members:

Takumi Abe[1], Peter Amerl, Paul Bernhardt[2], David Boteler[3], Leroy Cogger[4], Martin Connors[5],Donald Danskin[3], Eric Donovan[4], Abdelhaq Hamza[6], Hajime Hayakawa[1], Robert Horita[7], Glen Hussey[8], Gordon James, P.T. Jayachandran[6], Ludmila Kagan[9], Don Kim[6], David Knudsen[4], Sasha Kostov[8], Jim Laframboise[10], Richard Langley[6], Marc Lessard[11], John MacDougall[9], Karim Meziane[6], David Miles[14], John McMahon[10], Sandy Murphree[4], Jean-Marc Noël[12], W.K. Petersen[13], Paul Prikryl, Robert Rankin[14], Bernie Shizgal[15], Carl Siefring[2], George Sofko[8], Jean-Pierre St. Maurice[8], Trond Trondsen, Koichiro Tsuruda[1], Don Wallis, Clare Watt[14],Andrew Yau[4]

[1]JAXA/ISAS, Japan, [2]Naval Research Laboratory, USA, [3]Natural Resources Canada, [4]University of Calgary, [5]Athabasca University, [6]University of New Brunswick, [7]University of Victoria, [8]University of Saskatchewan, [9]University of Western Ontario, [10]York University, [11]University of New Hampshire, USA [12]Royal Military Collage of Canada, [13]University of Colorado, [14]University of Alberta, [15]University of British Columbia

Over the course of the mission, many members have retired or moved to other institutions. The current Science Team is a less formally organized group, now consisting of those who actively take part in planning and running experiments, analyzing data, and assimilating data into empirical models. There is currently no official list of Science Team members.

8 Reference Documentation

Table 11 lists applicable technical references for the Swarm-E spacecraft and data set. RD-1, the CASSIOPE/Swarm-E Processed Data Handbook, contains a comprehensive set of documents for understanding and interpreting the Swarm-E data, including many technical details of the spacecraft and e-POP instruments.

RD-1	CASSIOPE Spacecraft (Swarm-E) Processed Data Handbook https://epop.phys.ucalgary.ca/data-handbook
RD-2	CASSIOPE raw data formats https://epop.phys.ucalgary.ca/wp-content/ePOP-5024_e-POP_instrument_raw_and_processed_data_formats_REV_E.pdf
RD-3	e-POP data tutorials https://epop.phys.ucalgary.ca/e-pop-data-tutorials
RD-4	e-POP Data Explorer Web App (eDEx) https://edex.phys.ucalgary.ca
RD-5	e-POP Payload Quicklook Web App https://payloadquicklook.phys.ucalgary.ca/
RD-6	CASSIOPE star sensor attitude data combination https://epop.phys.ucalgary.ca/wp-content/uploads/2022/06/ESA-EOPSM-SWRM-TN-3487_New_Star_Sensor_Attitude_Solution.pdf
RD-7	CASSIOPE dimensioned engineering drawings https://epop.phys.ucalgary.ca/wp-content/CASSIOPE_Dimension_View.pdf
RD-8	Swarm-E spacecraft parameters used for MGF calibration https://epop.phys.ucalgary.ca/wp-content/Swarm-E_Spacecraft_Parameters_for_MGF_Calibration_Rev_B.pdf
RD-9	SpaceX Falcon 9 Press Kit for CASSIOPE launch https://epop.phys.ucalgary.ca/wp-content/SpaceX_F9_Demo_Mission_PressKit.pdf

Table 11: Swarm-E Technical References

9 PUBLICATIONS

Below is a list of peer-reviewed publications where CASSIOPE/Swarm-E data and analysis were the focus of the paper. Figure 118 is a chart of the number of CASSIOPE/Swarm-E of publications per year, since 2004. Listings highlighted in blue indicate an e-POP instrument paper.

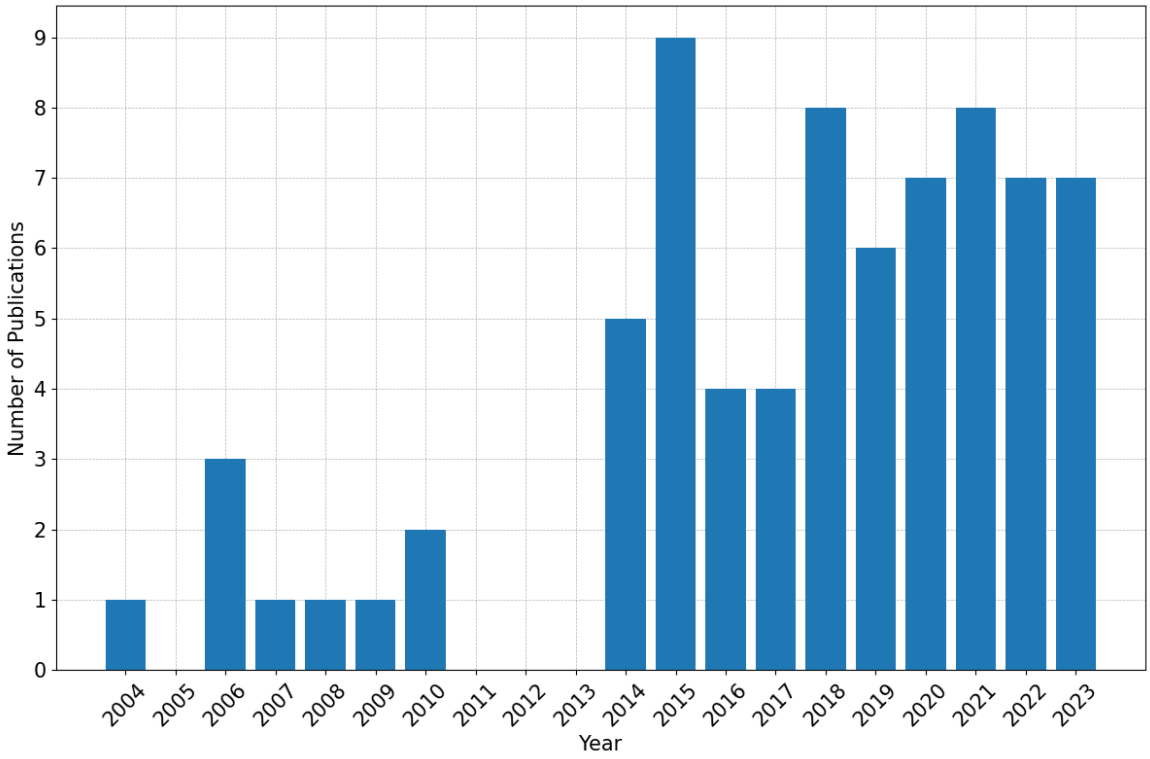

Figure 118: Number of CASSIOPE/Swarm-E publications by year

Bernhardt P. A., L. Scott, A. Howarth, and G.J. Morales, Observations of plasma waves generated by charged space objects, Phys. Plasmas 30, 092106 (2023), DOI: 10.1063/5.0155454

Bernhardt P.A., M.K. Griffin, W.C. Bougas, A.D. Howarth, H.G. James, C.L. Siefring, and S.J. Briczinski, Satellite Observations of Strong Plasma Wave Emissions With Frequency Shifts Induced by an Engine Burn From the Cygnus Spacecraft, Radio Science (2021), DOI: 10.1029/2020RS007143

Bernhardt P.A., W.C. Bougas, M.K. Griffin, C. Watson, R.B. Langley, A.D. Howarth, H.G. James, C.L. Siefring, G.W. Perry, J.D Huba, R.C. Moore, M.B. Cohen, and M. Gołkowski, Strong Amplification of ELF/VLF Signals in Space Using Neutral Gas Injections From a Satellite Rocket Engine, Radio Science (2021), DOI: 10.1029/2020RS007207

Broadfoot R., D.M. Miles, W. Holley, and A.D. Howarth, In situ calibration of the Swarm-Echo Magnetometers, Geoscientific instrumentation (2022), DOI: 10.5194/gi-11-323-2022

Burrell A.B., G.W. Perry, T.K. Yeoman, S.E. Milan, and R. Stoneback, Solar Influences on the Return Direction of High-Frequency Radar Backscatter, Radio Science (2018), DOI: 10.1002/2017rs006512

Burrell A.G., e-POP RRI provides new opportunities for space-based, high-frequency radio science experiments, Radio Science (2017), DOI: 10.1002/2017RS006257

Burrell A.G., S.E. Milan, G.W. Perry, T.K. Yeoman, and M. Lester, Automatically determining the origin direction and propagation mode of high-frequency radar backscatter, Radio Science (2015), DOI: 10.1002/2015RS005808

Calabia A. and S. Jin, Thermospheric Mass Density Disturbances Due to Magnetospheric Forcing From 2014–2020 CASSIOPE Precise Orbits, Journal of geophysical research. Space physics (2021), DOI: 10.1029/2021JA029540

Calabia A. and S. Jin, Upper atmosphere mass density variations from CASSIOPE precise orbits, Space Weather (2021), 19, DOI: 0.1029/2020SW00264

Cameron T. and D. Knudsen, Inverse electron energy dispersion from moving auroral forms, J. Geophys. Res. Space Physics (2016), DOI: 10.1002/2016JA023045

Clark R., Y. Fu, S. Dave, and R. Lee, Simulation of RSO Images for Space Situation Awareness (SSA) Using Parallel Processing, Sensors (2021), DOI: 10.3390/s21237868

Clark, R., Y. Fu, S. Dave, R. S. K. Lee, Resident space object (RSO) attitude and optical property estimation from space-based light curves, Advances in Space Research 70 (2022), DOI: 10.1016/j.asr.2022.08.068

Cogger L., A. Howarth, A. Yau, A. White, G. Enno, T. Trondsen, D. Asquin, B. Gordon, P. Marchand, D. Ng, G. Burley, M. Lessard, and B. Sadler, Fast Auroral Imager (FAI) for the e-POP Mission, Space Sci. Rev. (2014) DOI: 10.1007/s11214-014-0107-x

Danskin D.W., G.C. Hussey, R.G. Gillies, H.G. James, D.T. Fairbairn, and A.W. Yau, Polarization Characteristics Inferred From the Radio Receiver Instrument on the Enhanced Polar Outflow Probe, J. Geophys. Res. Space Physics (2018), DOI: 10.1002/2017JA024731

Desouky, M.A.A. and O. Abdelkhalik, A Recursive Approach for Magnetic Field Estimation in Spacecraft Magnetic Attitude Control, Aerospace (2022), DOI: 10.3390/aerospace9120833

Desouky, M.A.A. and O. Abdelkhalik, Improved Spacecraft Magnetic Attitude Maneuvering, Journal of spacecraft and rockets (2019), DOI: 10.2514/1.A34452

Durgonics T., A. Komjathy, O. Verkhoglyadova, E.B. Shume, H.-H. Benzon., A.J. Mannucci, M.D. Butala, P. Høeg, and R.B. Langley, Multiinstrument observations of a geomagnetic storm and its effects on the Arctic ionosphere: A case study of the 19 February 2014 storm, Radio Science (2017), DOI: 10.1002/2016RS006106

Eyiguler, E. C. K., W. Holley, A. D. Howarth, D. W. Danskin, K. Pandey, C. J. Martin, R. G. Gillies, A. W. Yau, G. C. Hussey, cavsiopy: a Python package to calculate and visualize spacecraft instrument orientation, Fronteirs in Astronomy and Space Sciences (2023), DOI: 10.3389/fspas.2023.1278794

Eyiguler, E. C. K., K. Pandey, A. D. Howarth, W. Holley, D.W. Danskin, G. C. Hussey, R. G. Gillies, A. W. Yau, Effect of spacecraft attitude on radio wave polarization measurements for the radio Receiver instrument on Swarm-E, Advances in Space Research 72 (2023) 4836–4855, DOI: 10.1016/j.asr.2023.09.001

Finley M.G., R.M. Broadfoot, S. Shekhar, and D.M. Miles, Identification and Removal of Reaction Wheel Interference From In-Situ Magnetic Field Data Using Multichannel Singular Spectrum Analysis, J. Geophys. Res. Space physics (2023), DOI: 10.1029/2022JA031020

Finley, M. G., T. A. Bowen, M. Pulupa, A. Koval, and D. M. Miles, Statistical Decomposition and Machine Learning to Clean In Situ Spaceflight Magnetic Field Measurements, Geophys. Res. Lett. (2023), DOI: 10.1029/2023GL103626

Gillies R.G., G.C. Hussey, G.J. Sofko, and H.G. James, Relative O- and X-mode transmitted power from SuperDARN as it relates to the RRI instrument on ePOP, Annales Geophysicae (2010), DOI: 10.5194/angeo-28-861-2010

Gillies R.G., G.C. Hussey, H.G. James, and G.J. Sofko, D. André, Modelling and observation of transionospheric propagation results from ISIS II in preparation for ePOP, Annales Geophysicae (2007), DOI: 10.5194/angeo-25-87-2007

Gupta A.S. and D.M. Miles, Autonomous Reaction Wheel Magnetic Signature Detection Against Background Noise in Spacecrafts, IEEE sensors letters (2023), DOI: 10.1109/LSENS.2023.3308124

Hauschild A., O. Montenbruck, and R.B. Langley, Flight results of GPS-based attitude determination for the Canadian CASSIOPE satellite, Wiley Navigation (2020), DOI: 10.1002/navi.348

Hussain S. and R. Marchand, Sheath-induced distortions in particle distributions near enhanced polar outflow probe particle sensors, Physics of Plasmas (2014), DOI: 10.1063/1.4887257

Huyghebaert D., J.P. St.-Maurice, K. McWilliams, G. Hussey, A.D. Howarth, P. Rutledge, and S. Erion, The Properties of ICEBEAR E-Region Coherent Radar Echoes in the Presence of Near Infrared Auroral Emissions, as Measured by the Swarm-E Fast Auroral Imager, Journal of geophysical research. Space physics (2021), DOI: 10.1029/2021JA029857

James H.G., E.P. King, A. White, and R.H. Hum, W.H.H.L. Lunscher, and C.L. Siefring, The e-POP Radio Receiver Instrument on CASSIOPE, Space Sci. Rev. (2015), DOI: 10.1007/s11214-014-0130-y

James H.G., Effects on transionospheric HF propagation observed by ISIS at middle and auroral latitudes, Advances in Space Research (2006), DOI: 10.1016/j.asr.2005.03.114

James H.G., Propagation Directions of High-Frequency Waves in the Ionosphere, Radio Science (2018), DOI: 10.1002/2017RS006474

James H.G., V.L. Frolov, E.S. Andreeva, A.M. Padokhin, and C.L. Siefring, Sura heating facility transmissions to the CASSIOPE/e-POP satellite, Radio Science (2017), DOI: 10.1002/2016RS006190

Kagan L.M., Aurora-Associated phenomena and the ePOP mission, Advances in Geosciences: Volume 2: Solar Terrestrial (2006), DOI: 10.1142/9789812707185_0018

Kim D. and R.B. Langley, The GPS attitude, positioning, and profiling experiment for the enhanced polar outflow probe platform on the Canadian CASSIOPE satellite, Geomatica (2010), 64(2), 233-243, DOI:10.5623/geomat-2010-0023

Knudsen D.J., J.K. Burchill, T.G. Cameron, G.A. Enno, A. Howarth, and A.W. Yau, The CASSIOPE/e-POP Suprathermal Electron Imager (SEI), Space Sci. Rev. (2015), DOI: 10.1007/s11214-015-0151-1

Lamarche L.J., R.H. Varney, and C.L. Siefring, Analysis of plasma irregularities on a range of scintillation-scales using the Resolute Bay Incoherent Scatter Radars, J. Geophys. Res. Space Physics (2020), DOI: 10.1029/2019JA027112

Leyser T.B., H.G. James, B. Gustavsson, and M.T. Rietveld, Evidence of L-mode electromagnetic wave pumping of ionospheric plasma near geomagnetic zenith, Annales Geophysicae (2018), DOI: 10.5194/angeo-36-243-2018

Liang J., Y. Shen, D. Knudsen, E. Spanswick, J. Burchill, E. Donovan, e-POP and Red Line Optical Observations of Alfvénic Auroras, J. Geophys. Res. Space Physics (2019), DOI: 10.1029/2019JA026679

Lui A.T.Y., L.L. Cogger, A. Howarth, and A.W. Yau, First Satellite Imaging of Auroral Pulsations by the Fast Auroral Imager on e-POP, Geophys. Res. Lett., (2015) 42, DOI: 10.1002/2015GL065331

Marchand R. and S. Hussain, Aberrations in Particle Distribution Functions Near e-POP Particle Sensors, IEEE Transactions on Plasma Science (2015), DOI: 10.1109/TPS.2015.2428715

Maxworth A., G. Hussey, and M. Gołkowski, Coexistence of Lightning Generated Whistlers, Hiss and Lower Hybrid Noise Observed by e-POP (SWARM-E)–RRI, Atmosphere (2020), DOI: 10.3390/atmos11020177

Miles D.M., A.D. Howarth, and G. Enno, In situ calibration of offsetting magnetometer feedback transients on the Cassiope spacecraft, Geoscientific instrumentation (2019), DOI: 10.5194/gi-8-187-2019

Miles D.M., I.R. Mann, I.P. Pakhotin, J.K. Burchill, A.D. Howarth, D.J. Knudsen, R.L. Lysak, D.D. Wallis, L.L. Cogger, and A.W. Yau, Alfvénic Dynamics and Fine Structuring of Discrete Auroral Arcs: Swarm and e-POP Observations, Geophys. Res. Lett. (2018), DOI: 10.1002/2017GL076051

Mohandesi, A., D.J. Knudsen, S. Skone, R.B. Langley, and A.W. Yau, Regional Mapping of Small-Scale Equatorial Ionospheric Irregularities Using Swarm Echo Satellite Measurements, Space Weather (2023); DOI: 10.1029/2023SW003417

Montenbruck O., A. Hauschild, R.B. Langley, and C. Siemes, CASSIOPE orbit and attitude determination using commercial off-the-shelf GPS receivers, GPS Solutions (2019), DOI: 10.1007/s10291-019-0907-2

Pandey K., E.C.K. Eyiguler, R.G. Gillies, G.C. Hussey, D.W. Danskin, and A.W. Yau, Polarization Characteristics of a Single Mode Radio Wave Traversing Through the Ionosphere: A Unique Observation From the RRI on ePOP/SWARM-E, J. Geophys. Res. Space Physics (2022), DOI: 10.1029/2022JA030684

Perry G.W., C. Watson, A.D. Howarth, D.R. Themens, V. Foss, R.B. Langley, and A.W. Yau, Topside ionospheric disturbances detected using radio occultation measurements during the August 2017 solar eclipse, Geophys. Res. Lett. (2019), DOI: 10.1029/2019GL083195

Perry G.W., H.G. James, R.G. Gillies, A. Howarth, G.C. Hussey, K.A. McWilliams, A. White, and A.W. Yau, First results of HF radio science with e-POP RRI and SuperDARN, Radio Science (2016), DOI: 10.1002/2016RS006142

Perry G.W., K. Ruzic, K. Stern, A.D. Howarth, A.W. Yau, Modeling and validating a SuperDARN radar's Poynting flux profile, Radio Science (2022), DOI: 10.1029/2021RS007323

Perry G.W., N.A. Frissell, E.S. Miller, M. Moses, A. Shovkoplyas, A.D. Howarth, and A.W. Yau, Citizen Radio Science: An Analysis of Amateur Radio Transmissions With e-POP RRI, Radio Science (2018), DOI: 10.1029/2017RS006496

Shen Y. and D.J. Knudsen, Suprathermal Electron Acceleration Perpendicular to the Magnetic Field in the Topside Ionosphere, J. Geophys. Res. Space Physics (2020), DOI: 10.1029/2019JA027449

Shen Y., A. Artemyev, X.J. Zhang, I.Y. Vasko, A. Runov, V. Angelopoulos, and D. Knudsen, Potential Evidence of Low-Energy Electron Scattering and Ionospheric Precipitation by Time Domain Structures, Geophysical Research Letters, 47(16), p.e2020GL089138 (2020), DOI: 10.1029/2020GL089138

Shen Y., D.J. Knudsen, J.K. Burchill, A. Howarth, A.W. Yau, R.J. Redmon, D.M. Miles, R.H. Varney, and M.J. Nicolls, Strong ambipolar-driven ion upflow within the cleft ion fountain during low geomagnetic activity, J. Geophys. Res. Space Physics (2016), DOI: 10.1002/2016JA022532

Shen Y., D.J. Knudsen, J.K. Burchill, A.D. Howarth, A.W. Yau, D.M. Miles, H.G. James, G.W. Perry, and L. Cogger, Low-altitude ion heating, downflowing ions, and BBELF waves in the return current region, J. Geophys. Res. Space Physics (2018), DOI: 10.1002/2017JA024955

Shen, T., L. Chen, X. Zhang, A. Artemyev, V. Angelopoulos, C.M. Cully, H.G. James, A. Yau, A.D. Howarth, J. Bortnik, J. Wu, S. Tian, M.D. Hartinger, M. Connors, and R.B. Horne, Conjugate Observation of Magnetospheric Chorus Propagating to the Ionosphere by Ducting, Geophysical Research Letters (2021), DOI: 10.1029/2021GL095933

Shen, Y. and D.J. Knudsen, On O+ ion heating by BBELF waves at low altitude: Test particle simulations, J. Geophys. Res. Space Physics, 125(8), p.e2019JA027291 (2020), DOI: 10.1029/2019JA027291

Shen, Yangyang, Microphysics of ion and electron energization in the topside ionosphere, PhD Dissertation, University of Calgary, October 2019

Shume E.B., A. Komjathy, R.B. Langley, O. Verkhoglyadova, M.D. Butala, and A.J. Manucci, Intermediate scale plasma irregularities in the polar ionosphere inferred from GPS radio occultation, Geophys. Res. Lett. (2015), DOI: 10.1002/2014GL062558

Shume E.B., P. Vergados, A. Komjathy, R.B. Langley, and T. Durgonics, Electron number density profiles derived from radio occultation on the CASSIOPE spacecraft, Radio Science (2017), DOI: 10.1002/2017RS006321

Siefring C.L., P.A. Bernhardt, H.G. James, and R.T. Parris, The CERTO Beacon on CASSIOPE/e-POP and Experiments using High-Power HF Ionospheric Heaters, Space Sci. Rev. (2014), DOI: 10.1007/s11214-014-0110-2

Wallis D.D., D.M. Miles, B.B. Narod, J.R. Bennest, K.R. Murphy, I.R. Mann, and A.W. Yau, The CASSIOPE/e-POP Magnetic Field Instrument (MGF), Space Sci. Rev. (2014), DOI: 10.1007/s11214-014-0105-z

Wang L., J.W. MacDougall, and H.G. James, Ionospheric structure effects on HF radio wave propagation for the enhanced polar outflow probe (e-POP) satellite mission, Radio Science (2004), DOI: 10.1029/2003RS002975

Wang, L., J.W. MacDougall, and R. Abugharbieh, Proposal for ionospheric tomography technique using a new HF radio source, Advances in Space Research (2008), DOI: 10.1016/j.asr.2007.09.014

Watson C., R.B. Langley, D.R. Themens, A.W. Yau, A.D. Howarth, and P.T. Jayachandran, Enhanced Polar Outflow Probe ionospheric radio occultation measurements at high latitudes: Receiver bias estimation and comparison with ground-based observations, Radio Science (2018), DOI: 10.1002/2017RS006453

Wood A. G., et al. Variability of Ionospheric Plasma: Results from the ESA Swarm Mission, Space Sci. Rev. (2022), DOI: 10.1007/s11214-022-00916-0

Wu J., D.J. Knudsen, Y. Shen, and D.M. Gillies, e-POP Observations of Suprathermal Electron Bursts in the Ionospheric Alfvén Resonator, Journal of Geophysical Research: Space Physics, 126(2), p.e2020JA028005 (2021), DOI: 10.1029/2020JA028005

Wu, Jiashu, Static and Alfvénic Electrodynamics in the Auroral Region, PhD Dissertation, University of Calgary, July 2020

Yau A.W. and A. Howarth, Imaging thermal plasma mass and velocity analyzer, J. Geophys. Res. Space Physics (2016), DOI: 10.1002/2016JA022699

Yau A.W. and H.G. James, CASSIOPE Enhanced Polar Outflow Probe (e-POP) Mission Overview, Space Sci. Rev. (2015), DOI: 10.1007/s11214-015-0135-1

Yau A.W., A. Howarth, A. White, G. Enno, and P. Amerl, Imaging and Rapid-Scanning Ion Mass Spectrometer (IRM) for the CASSIOPE e-POP Mission, Space Sci. Rev. (2015), DOI: 10.1007/s11214-015-0149-8

Yau A.W., H.G. James, and L.L. Cogger, The Canadian Enhanced Polar Outflow Probe (e-POP) Mission, Physics in Canada (2014), 70(4), 229-234, DOI: 10.1016/j.asr.2005.01.058

Yau A.W., H.G. James, and W. Liu, The Canadian Enhanced Polar Outflow Probe (e-POP) mission in ILWS, Advances in Space Research (2006) DOI: 10.1016/j.asr.2005.01.058

Yau A.W., H.G. James, P.A. Bernhardt, L.L. Cogger, G.A. Enno, H. Hayakawa, A. Howarth, E.P. King, D.J. Knudsen, R.B. Langley, R. Rankin, R.H. Hum, D.D. Wallis, and A. White, The Canadian enhanced polar outflow probe (e-POP) mission: Current status and planned observations and data distribution, Data Science Journal (2009), DOI: 10.2481/dsj.8.S38

Yau A.W., V. Foss, A.D. Howarth, G.W. Perry, C.Watson, and J. Huba, Eclipse-Induced Changes to Topside Ion Composition and Field-Aligned Ion Flows in the August 2017 Solar Eclipse: e-POP Observations, Geophys. Res. Lett. (2018), DOI: 10.1029/2018GL079269

Yau A.W., Z. Ali, C. Alonso, C. Casgrain, G.A. Enno, B. Entus, M. Grigorian, J. Hemingway, A. Howarth, R.H. Hum, H.G. James, P. Langlois, M. Senez, and A. White, The Canadian CASSIOPE Small Satellite Mission: The Enhanced Polar Outflow Probe and Cascade Technology Demonstration Payloads, Acta Astronautica (2015), DOI: 10.1016/j.actaastro.2015.01.016

Yau, A. W., A. D. Howarth, D. J. Knudsen, J. S. Murphree, T. S. Trondsen, Leroy L. Cogger: A Pioneer in Optical Observations From Space, Perspectives of Earth and Space Scientists, DOI: 10.1029/2022CN00019

APPENDIX A

List of Acronyms

Acronym	Meaning
ADCS	Attitude Determination and Control System
ARRL	American Radio Relay League
AUTUMNX	Athabasca University Themis UCLA Magnetometer Network eXtension
C&DH	Command & Data Handling Unit
CADI	Canadian Advanced Digital Ionosonde
CARISMA	Canadian Array for Realtime Investigations of Magnetic Activity
CASSIOPE	CAScade Smallsat and IOnospheric Polar Explorer
CCD	Charge Coupled Device
CDF	Common Data Format
CERTO	Coherent Electromagnetic Radio Tomography Instrument
CODAR	Coastal Ocean Dynamics Applications Radar
CPU	Central Processing Unit
DC	Direct Current
DLR	Deutsches Zentrum für Luft- und Raumfahrt (translates as German Center for Air- and Space-flight)
DMSP	Defense Meterological Satellite Program
DSX	Demostration and Science Experiments
EEPROM	Electronically Erasable Programable Read-Only Memory
EISCAT	European Incoherent SCATter
e-POP	Enhanced Polar Outflow Probe
ESA	European Space Agency
FAI	Fast Auroral Imager
FLASH	Frequency Limited Acoustic SHock
FOV	Field of View
GAP	GPS, Attitude, Positioning, and Profiling Instrument
GPS	Global Positioning System
HAARP	High-Frequency Active Auroral Research Program
HDF5	Hierarchical Data Format 5
HF	High Frequency
HVPS	High Voltage Power Supply
ICEBEAR	Ionospheric Continuous-wave *E* region Bistatic Experimental Auroral Radar
ICI	Investigation of Cusp Irregulaties
IRM	Imaging and Rapid Scanning Ion Mass Spectrometer Instrument
ISR	Incoherent Scatter Radar
ITRF	International Terrestrial Reference Frame
JAXA	Japan Aerospace Exploration Agency
kbps	Kilobits per second

kHz	Kilohertz
LEOP	Launch and Early Operations Phase
LOS	Line-of-Sight
Mbps	Megabits per second
MDA	MacDonald, Dettwiler and Associates
MGF	MaGnetic Field Instrument
MHz	Megahertz
NMS	Neutral Mass Spectrometer Instrument
NRCan	Natrual Resources Canada
RENU	Rocket Experiment for Neutral Upwelling
RF	Radio Frequency
RINEX	Receiver INdependent EXchange Format
RISR-C	Resolute Bay Incoherent Scatter Radar Canada
RISR-N	Resolute Bay Incoherent Scatter Radar North
RRI	Radio Receiver Instrument
SAA	South Atlantic Anomaly
SEI	Suprathermal Electron Imager Instrument
SP3	Standard Product 3
SSA	Star Sensor A
SSB	Star Sensor B
SSC	Swedish Space Corporation
SuperDARN	Super Dual Auroral Radar Network
TEC	Total Electron Content
TIGER	Tasman International Geospace Environment Radars
TPM	Third Party Mission
TT&C	Telemtry, Tracking and Command
u-ASC	Micro-Advanced Stellar Compass
UTC	Coordinated Universal Time
VLF	Very Low Frequency

APPENDIX B

List of S-Band Ground Station Acquisition Times

The CASSIOPE/Swarm-E S-band Ground Station Data Acquisition Contact Times are listed in the companion document *SWE-PO-Final Operations Report Appendix B.xlsx.*